Molybdenum/tungsten-carbide and nickel-phosphide as emerging catalysts for deoxygenation reactions

Luana Souza Macedo

Thesis committee

Promotors

Prof. Dr J.H. Bitter

Professor of Biobased Chemistry and Technology

Wageningen University & Research

Prof. Dr V. Teixeira da Silva (in memoriam)

Associate professor, Chemical Engineering Program, Alberto Luiz Coimbra Institute of Engineering Pos-graduation and Research (COPPE)

Federal University of Rio de Janeiro, Brazil

Other members

Prof. Dr J. van der Gucht, Wageningen University & Research

Prof. Dr K. Seshan, University of Twente, Enschede

Prof. Dr P.C.A. Bruijnincx, Utrecht University

Dr R. Gosselink, BASF, Utrecht

This research was conducted under the auspices of the Graduate School VLAG (Advanced studies in Food Technology, Agrobiotechnology, Nutrition and Health Sciences).

Molybdenum/tungsten-carbide and nickel-phosphide as emerging catalysts for deoxygenation reactions

Luana Souza Macedo

Thesis
submitted in fulfilment of the requirements for the degree of doctor
at Wageningen University
by the authority of the Rector Magnificus,
Prof. Dr A.P.J. Mol,
in the presence of the
Thesis Committee appointed by the Academic Board
to be defended in public
on Tuesday 29 January 2019
at 1.30 p.m. in the Aula.

Luana Souza Macedo
Molybdenum/tungsten-carbide and nickel-phosphide as emerging catalysts for deoxygenation reactions,
195 pages.

PhD thesis, Wageningen University, Wageningen, the Netherlands (2019)
With references, with summary in English

ISBN 978-94-6343-547-5
DOI http://doi.org/10.18174/464686

Table of contents

Chapter 1

Introduction

1. General aspects of catalysts

Catalysts are at the heart of industrial chemical transformations and approximately 90% of all chemical industry products require a catalytic step [1]. In 2014, the global demand of catalysts was about US$ 33.5 billion and a steady increase in this demand is expected in the next years [2]. To meet this growing market demand, both governments and catalyst producers are investing in research and development of new catalysts, products, processes and technologies [2].

Catalyst technologies can be grouped into three main areas of relevant economical interest: petroleum refining to fuels or to chemicals and environmental catalysis [3]. Petroleum refining includes several processes, such as catalytic reforming, fluid catalytic cracking, hydrocracking and hydrotreating. Chemicals manufacturing is commonly defined according to reaction type, for example hydrogenation, polymerization and oxidation. Finally, environmental catalysis is often related to cleaning off gases or to the conversion of bio-based sources into marketable products.

To advance the catalysis field it is essential to understand the relationship between catalyst properties and performance [4]. For example, it has been shown that catalyst properties like particle size, acidity and support can significantly influence catalyst performance [5 – 7]. Hence, the steering of such properties is essential to improve the performance of catalysts making their use attainable in the industry. For instance, an interesting new group of catalysts that would be benefited by this understanding of catalyst properties–performance relationship is the transition metal carbides and phosphides, which are the catalysts under study in this thesis. These catalysts are potential substitutes of the limited available noble metals.

For several reactions, it has been shown that carbide and phosphide based catalysts can display similar or even better catalytic performance than noble metal catalysts [8 – 13]. Since the seminal work of Levy and Boudart [14] on water formation from H_2 and O_2 at room temperature over W-carbide, it became clear that transition metal carbides are efficient catalysts for reactions that involve hydrogen activation, such as ammonia synthesis and decomposition, hydrogenation, hydrogenolysis, hydro-isomerization, methanation and hydroprocessing [4]. Metal phosphides are also active catalysts in hydrotreatment reactions (Li *et al.* [15]), thus transition metal carbides and phosphides hold great potential as they are more available and can be at least equally active as compared to noble metals.

In this thesis this group of non-noble metal catalysts – the transition metal carbides and phosphides – will be investigated and we will focus on the study of catalyst properties-performance relations and the influence of synthesis conditions

on the catalyst properties. For that, we apply transition metal carbides and phosphides for the deoxygenation of vegetable oil. The deoxygenation of vegetable oils can yield different products such as aldehydes, alcohols, olefins and paraffins, which are relevant for industry as chemical building blocks or as fuels [16]. The use of biobased renewable feedstock in the production of chemical building blocks and fuels is essential to ensure a more sustainable future.

2. Some challenges for the biobased economy

A biobased economy can be defined as an economy where renewable biomass (organic matter) instead of fossil resources (*i.e.* gas, oil and coal) is at the base of the production chain [17]. The interest in the use of biomass as feedstock increased significantly in the past few years to compensate the expected decrease in easily accessible oil availability and the need to decrease greenhouse gas emissions [18].

2.1 Crude oil for fuel and chemicals production

Currently the worlds' demand for crude oil is about 90 million barrels per day [19]. Figure 1 displays an overview of the oil demand per sector. The transportation sector is responsible for 57% of the total oil demand, divided in road transportation (44%), aviation (6%), marine bunkers (5%) and rail and domestic waterways (2%). The non-transportation sectors, 'other industry', which primarily comprises iron, steel, glass and cement production, construction and mining, accounts for 15% of total oil demand, followed by petrochemicals (11% of total demand), residential/commercial/agriculture (10% of total demand) and electricity generation (7% of total demand) [19].

Currently crude oil is the dominant energy carrier (Figure 2). From a total of $1.3x10^4$ million tonnes oil equivalent in 2015, the consumption of primary energy worldwide was more than 85% fossil fuel (oil, coal and natural gas), followed by 7% hydropower, 4% nuclear energy and 3% renewables [20].

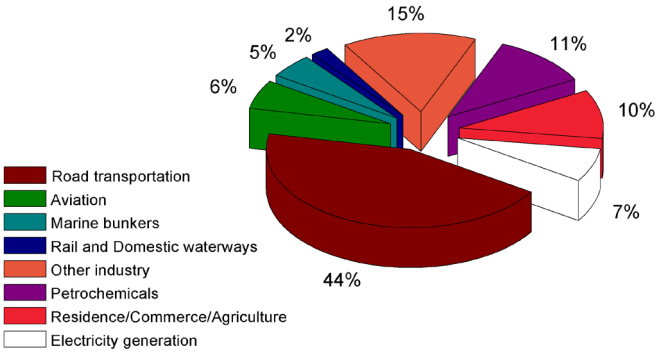

Figure 1. Global oil demand per sector in 2014 [19].

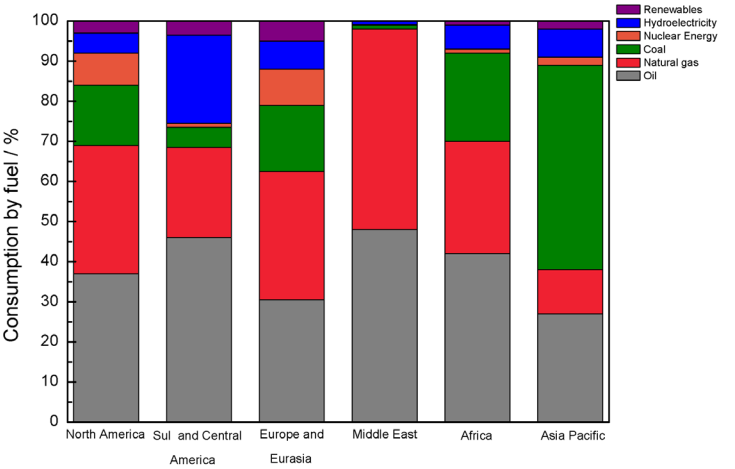

Figure 2. Regional consumption of energy carriers in 2015 [20].

In addition, crude oil is also a feedstock to produce diverse chemicals. According to the review by Eneh [21], the production of chemicals from petroleum has increased since World War II and Table 1 displays examples of the petrochemicals and their products.

Table 1. Petrochemicals and their products [21 – 24].

Petrochemical	**Products**
Methane	Carbon black, ethyne, synthesis gas, halogenmethanes, hydrogen cyanide
Ethyne	Chloroethene compounds, ethanol

Chloroethene compounds	Polymers, e.g. poly(chloroethane)
Synthesis gas	Methanol, ammonia
Methanol	Methanal
Ethene	Poly(ethene), ethylbenzene, epoxyethane, ethanol, 1,2-dichloroethane
Ethylbenzene	Phenylethene
Epoxyethane	Ethane-1,2-diol
Ethanol	Ethanal
1,2-dichloroethane	Chloroethene
Phenylethene	Poly(phenylethane)
Chloroethene	Poly(chloroethene)
Propene	Polypropene, propenontrile, propan-2-ol, 1-(methylethyl)benzene, propane-1,2,3-triol, methylbuta-1,3-diene
Propenontrile	Acrylnitrile-based polymers
Propan-2-ol	Propanone
Propanone	Perspex
1-(methylethyl)benzene	Phenol
Phenol	Bakelite-type resins
Propane-1,2,3-triol	Alkyd resins
Methylbuta-1,3-diene	Artificial rubbers
But-1-ene, But-2-ene	Buta-1,3-diene, poly(butene)
2-Methylpropene	2-methylpropan-2-ol
Buta-1,3-diene	Butadiene-based polymers
Benzene	Phenylethene, cyclobenzene, phenol, phenylamine
Methylbenzene	Benzene, caprolactam
1,4-Dimethylbenzene	Benzene-1,4-dicarboxylic acid

Phenylamine	Aniline dyes
Caprolactam	Nylon
Benzene-1,4-dicarboxylic acid	Terylene

This large amount of fossil resources used for fuel and chemicals production has a number of implications for the future. For example, i. the growing energy demand and limited resources of fossil fuel put pressure on the energy security in the future and ii. the use of fossil resources have a negative environmental impact [25].

i. Growing oil demand and its limited resources

According to Abas *et al.* [26], from 1965 to 2014, the rise rate of oil consumption was 1.4 million barrel per year (Mb/yr) while the rise rate of oil production versus oil consumption was 0.56 Mb/yr [26] indicating that consumption increased approximately two times faster than oil production.

Altogether the world energy consumption increased from 430 million tonnes oil equivalent in 1860 to 10318 million tonnes oil equivalent in 2010 [25]. At the same time, while the world's population increased six times during the twentieth century, energy consumption increased by a factor of 80 [27].

The growing energy demand and oil consumption rates become an issue because crude oil is a limited resource and it is the main component of primary energy worldwide. Oil reservoirs need three conditions to develop; i. a rich source of rock; ii. a migration conduit and; iii. a trap that forms the reservoirs. The reservoirs are considered not to be replenishable (*i.e.* the abiogenic replenishment is negligible) and the availability of oil is often described by the Hubbert peak theory [28]. This theory relates the long-term rate of production of conventional oil and other fossil fuel to its consumption and predicts that world oil production will reach a peak and then decline as the reserves are exhausted. In the eminence of this scenario, it becomes important to consider oil substitutes to supply for the world's oil demand and to produce energy carriers and chemicals in the future.

ii. Environment impact

According to Züttel *et al.* [25], the combination of consumption of fossil resources and deforestation is responsible for the emission of 7×10^{12} kg yr^{-1} of

carbon as CO_2. At the same time, the plants and the ocean can naturally sink around 2 x 10^{12} kg yr^{-1} of CO_2 each, via photosynthesis and dissolution, respectively [25]. Thus, according to these estimates, the human activity is responsible for the liberation of an excess of approximately 3 x 10^{12} kg yr^{-1} of carbon in the form of CO_2.

In fact, CO_2 emissions has increased over time [26] and since CO_2 is a greenhouse gas (GHG) and its emission to the atmosphere is related to the raising of Earth average temperature [29], the abundant use of crude oil is linked to a phenomenon named global warming.

To tackle global warming, during the Paris Agreement in 2015, 144 countries agreed that severe measures related to energy use efficiency and sources should be taken. Such measures are meant to deaccelerate global warming and keep it well-below 2°C. To reach that goal, scaled-up action in energy efficiency and especially the use of renewable energy/resources is critical [30] and will be probably one of the most relevant topics of this century.

3. Biomass as alternative of fossil resources

Biomass (for example wood) was the main energy carrier before the discovery of oil in the nineteenth century [31]. Furthermore, biomass was used throughout recorded history to yield valuable products such as medicines, flavours and fragrances [18]. With the discovery of oil as a cheap energy carrier with a high energy density and as a source for chemicals, the use of biomass was soon abandoned [18, 31]. However, biomass has regained attention in the last years since it is renewable on a reasonable timescale and the search for fossil oil substitutes has increased.

According to Europe Biomass Industry Association (EUBIA), Europe, Africa and Latin American are able to produce 8.9, 21.4 and 19.9 EJ (10^{18} Joule) from residual biomass per year, with an energy equivalence of 196, 490 and 448 million tonnes oil equivalent, respectively [31]. It represents 25% of world oil consumption as primary energy [20].

Although many types of renewable sources are available to produce sustainable electricity and heat, such as the sun, the wind and hydroelectric, biomass is the only renewable source that can produce products that can be used in the current infrastructure as fuel or chemical because biomass contains carbon [32].

Biomass processing to obtain multiple bio-based products such as biofuel and chemicals is the concept of a biorefinery [33]. Figure 3 illustrates the ideal fully integrated biomass cycle considering a biorefinery as the processing tool to convert feedstock into several bio-based products [34].

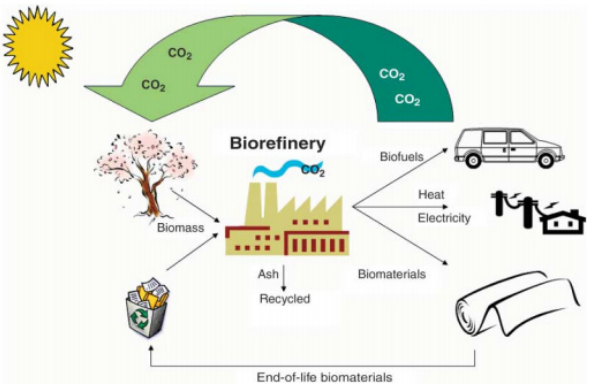

Figure 3. Fully integrated biomass cycle to obtain biofuel, biomaterials and biopower. (From [34]. Reprinted with permission from AAAS.)

Among many biomass products, such as terpenes, fats, oils, lignin and sugars, fats and oils are promising compounds which can be used in industry as fuel or chemicals in the near future [18, 35]. In general, the main chemical difference between biomass based feedstocks and crude oil is the higher oxygen content of the former. Therefore, deoxygenation is a key conversion technology to make chemicals/ fuels from biomass which are compatible with the current industrial infrastructure. In that way the so called drop-in chemicals can be made from biomass [16, 36].

4. Deoxygenation of vegetable oil

Vegetable oil fraction, mainly triglycerides, will be the focus in this thesis, which correspond, together with proteins, extractives and ash typically 15 – 20% of biomass composition by weight [37]. For that fraction deoxygenation is needed to produce olefins and paraffins, which can be used as fuel or building blocks of different chemicals like surfactants and lubricants [16, 36].

Many researches employ fatty acid as model molecule of vegetable oil. To evaluate the differences of vegetable oil and fatty acid as feedstock in deoxygenation reaction, Peng *et al.* [38] and Santillan-Jimenez *et al.* [39] compared activity and selectivity of several catalysts using two different feedstocks: triglycerides and stearic acid (Table 2). Their results indicate that although the rate of stearic acid conversion are higher than that obtained with triglycerides, those rates are in a similar range. Furthermore, selectivity for C17 and C18 hydrocarbons was comparable for both feedstocks. As conclusion, fatty acids are considered as representative model molecules of vegetable oil in deoxygenation reaction.

Table 2. Comparison of deoxygenation (DO) average activity between triglycerides and fatty acid feedstocks.

Catalyst	Feedstock	Reaction conditions	Average activity (10^{-1} mol_{DO} mol^{-1}_{metal} s^{-1})
Ni/H-β [38]	Microalgae oil	260 °C, 40 bar H_2	0,38
	Stearic acid		0,33
Pd/C [39]	Triesterin	300 °C, 9 bar H_2	0,42
	Stearic acid		0,60

The three main reactions (Figure 4) during fatty acid deoxygenation are: (i) decarbonylation *i.e.* the removal of oxygen as CO and water with the formation of alkene; (ii) decarboxylation *i.e.* the removal of oxygen as CO_2 with the formation of alkane; and (iii) hydrodeoxygenation *i.e.* the removal of oxygen as water via participation of hydrogen with the formation of an alkane with the same number of carbon as the original fatty acid [16].

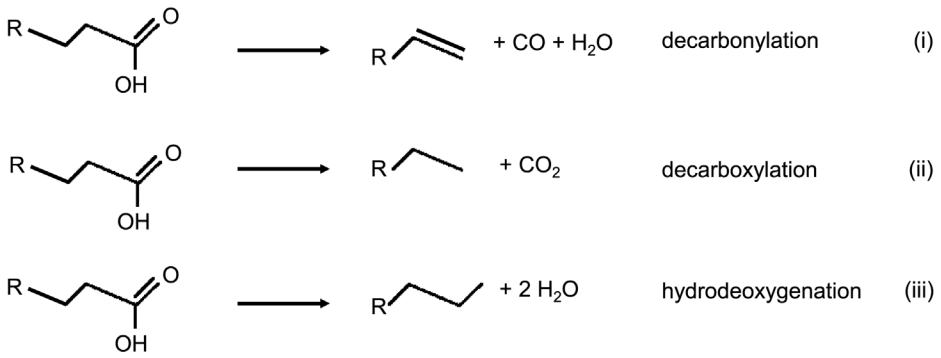

Figure 4. Overview of possible fatty acid deoxygenation reactions [16].

Metal sulfides and noble metals are the most studied catalysts for deoxygenation reactions [40]. Recently, transition metal carbides and phosphides also appeared as potential catalysts for these reactions and triggered the interest on this new class of catalysts [41 – 44]. Next, we describe those catalysts and their application for HDO reactions.

5. Catalysts for hydrodeoxygenation reactions

5.1 Metal sulfides

Conventional catalysts for hydrodesulfurization and hydrodenitrogenation reactions, such as the alumina supported sulfides of NiMo and CoMo are often employed in hydrodeoxygenation reactions [45 – 48]. Ni acts as Mo promoter in catalysts for deoxygenation of vegetable oil. For example, rapeseed oil deoxygenation occurs at 260 °C and 3.5 MPa H_2 and resulted in 92% conversion over sulfided $NiMo/Al_2O_3$ catalyst, while the same reaction over sulfided Mo/Al_2O_3 and sulfided Ni/Al_2O_3 catalysts reached 60 and 38% of conversion, respectively thus indicating the beneficial effect of having both components [49]. Furthermore, when sulfided Ni/Al_2O_3 and Mo/Al_2O_3 are used separately in deoxygenation reactions, Ni favors the decarbonylation/decarboxylation route while Mo favors the hydrodeoxygenation one. On the other hand, sulfided $NiMo/Al_2O_3$ are active for both the decarbonylation/decarboxylation and the hydrodeoxygenation pathways [49].

Metal sulfides are active for deoxygenation reactions, however they deactivate due to sulfur removal from their active sites to form H_2S [50]. This disadvantage can be partially overcome by the addition of sulfur components, such as dymethylsulfide to the feed (0.5 wt%). However, the presence of H_2S will decrease the HDO/DCO ratio decreasing the production of hydrocarbons with higher energy content. Furthermore, the presence of sulfur on the products stream is undesired, specially for environmental reasons [50].

5.2 Metals

Metals are also active for the deoxygenation of vegetable based feedstocks [51 – 56]. For example, Morgan *et al.* [51] used 20 wt% Ni/C, 5 wt% Pd/C and 1 wt% Pt/C for the deoxygenation of triglycerides under inert atmosphere. The authors observed that although all catalysts performed deoxygenation, as shown in Table 3, Ni catalyst perfomed cracking as side reaction in higher extension compared to Pd and Pt catalysts. However, weigth based activities were reported instead of turn over frequencies which makes it difficult to make a fair comparison between the activity of the evaluated catalysts.

Table 3. Conversion of 20 g triglicerides over 0.22 g of Pt/C, Pd/C and Ni/C catalysts at 350 °C and 7 bar N_2 [51].

	Conversion to hydrocarbons (%)		
	Tristearin	Triolein	Soybean oil
1% Pt/C	42	24	23
5% Pd/C	29	47	30
20% Ni/C	85	81	92

Noble metals are often used as catalysts for deoxygenation reactions because of their good stability (Table 4). However, their limited availability and to a certain extent their high prices spurs research towards more readily available metals. For instance, the total amount of the world resources of platinum group metal, which includes platinum and palladium – common noble metals used as catalyst for deoxygenation processes – are more restricted compared to the total world resources of nickel and molybdenum, which are common transition metals used in phosphides and carbides (Table 5).

Table 4. Examples of studies employing metal as catalyst for deoxygenation reactions.

Catalyst	**Feedstock**	**Reaction conditions (P, T, reactor, atmosphere)**
[53] Pd/C	Stearic acid Ethyl stearate Triesterin	17 – 40 bar 300 – 360 °C Semi-batch He, H_2, 5% H_2/He
[54] Pt/Al2O3	Methyl octanoate Methyl stearate	6.9 bar 300 – 350 °C Semi-bacth He, H_2
[51] Ni/C Pd/C Pt/C	Triesterin Triolein Soybean oil	6.9 bar 350 °C Batch N_2

[55] Pt/Al2O3 Pt/SiO2 PtSn/SiO2 PtSnK/SiO2	Methyl octanoate Methyl laurate	3.2 and 5.2 bar 320 – 350 °C Semi-batch He
[56] Pd/SiO2 Pd/Al2O3 Pd/C	Stearic acid Lauric acid Capric acid	15.2 bar 300 °C Semi-batch 5% H_2/He

Table 5. Estimated total amount of metal world resources [57].

Metal	World resources (kilograms)
Platinum group metal	$100x10^6$
Nickel	$130x10^9$
Molybdenum	$19.4x10^9$

5.3 Transition metal carbides and phosphides

Transition metal carbides can have simple crystalline structure, with metal atoms at the vertex of face centered cubic (fcc), hexagonal closed packed (hcp) and simple hexagonal (hex) structures. Non-metallic atoms (carbon) are located between the metallic atoms, forming octaedric sites on fcc and hcp structures and trigonal prism sites on hex structure (Figure 5) [4]. These materials are able to adsorb and to transfer hydrogen to reactant molecules, making them promising catalysts for hydrotreating reactions [58].

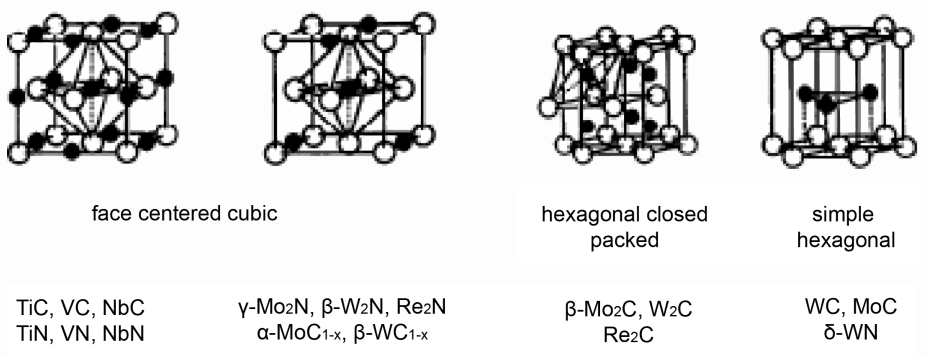

Figure 5. Common crystal structures of carbides and nitrides, where black circles are non metal atoms (C, N) and white circles are metal atoms [4].

Recent studies have shown that transition metal carbides are active and stable for deoxygenation reactions. Sousa *et al.* [41], for example, used β-Mo_2C/Al_2O_3 in sunflower oil hydrodeoxygenation at 360 °C and 5 MPa and concluded that the oil is transformed into saturated hydrocarbons in two steps. In the first step triglycerides undergo thermal cracking to form free fatty acids and in the second step the free fatty acids are hydrogenated to form n-alkanes. Gosselink *et al.* [42] found similar result when they used tungsten-carbide based catalysts in stearic acid deoxygenation. However, when the carbide was converted to an oxide the reaction pathway shifted from hydrodeoxygenation to decarboxylation/decarbonylation.

Besides transition metal carbides, transition metal phosphides are also potential catalysts for hydrotreating reactions [12, 13, 43, 44, 59 – 65]. When comparing the structures of carbides and phosphides, the main differences are the result of the larger size of P compared to C. While the carbon atoms occupy the interstices between the metallic atoms to form simple structures in the carbides, the phosphorus atoms cannot ocuppy the same position in the phosphides. Instead, metal atoms form triagular prisms around the phosphorus atoms on phosphides (Figure 6). This phosphides structure enable reactant molecules to access active sites located on the surface edges of crystalline structure [66].

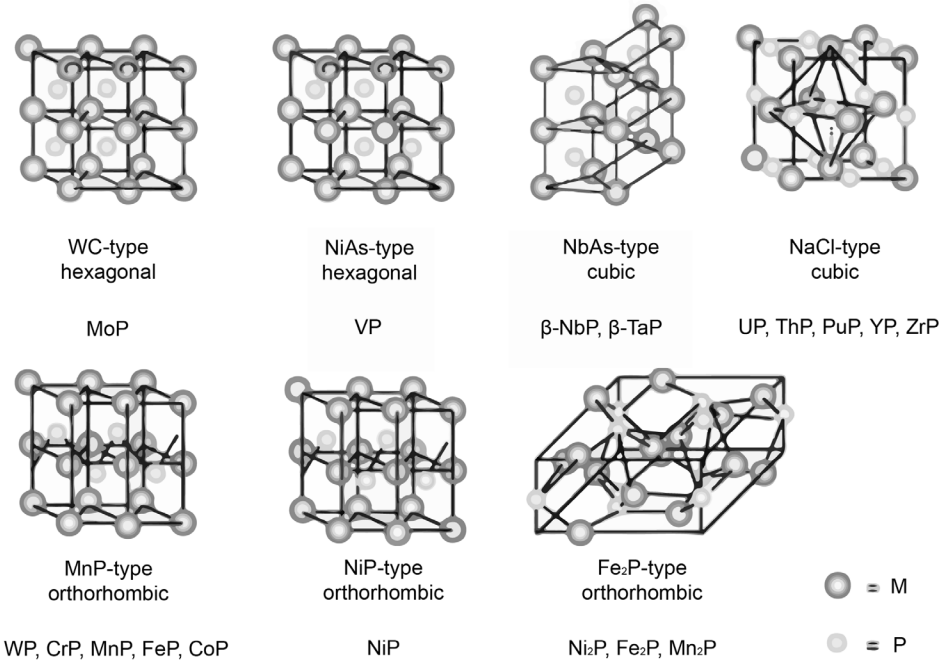

Figure 6. Crystal structures of metal rich phosphides [66].

Based on the metal/phosphorus ratio on the phosphides structure, they are described as metal rich or as phosphorus rich. While metal rich phosphides have metallic properties, phosphorus rich phosphides are semiconductors and less stable than the former. Metal rich transition metal phosphides, in turn, combine properties of metallic and ceramic materials. They are good heat and electricity conducters, hard, resistant and thermally and chemically stable [66].

Transition metal phosphides are active for hydrodesulfurization and hydrodenitrogenation reactions [59 – 62], and also for hydrodeoxygenation reactions [12, 13, 42, 43, 63 – 65]. Yang *et al.* [64] and Oyama *et al.* [44], for example, showed that transition metal phosphides can have even higher activity for deoxygenation reactions than metals and commercial sulfides.

Transition metal phosphides catalysts can show different activity and selectivity depending on the transition metal employed and on their synthesis histrory. For example, for deoxygenation of methyl laurate (a C12 ester) at 300 ^{o}C and 2 MPa, while Ni, Co and Fe phosphides presented C11 hydrocarbons as the main products (decarbonylation/decarboxylation pathway), Mo and W phoshphides produced predominantly C12 hydrocarbons (hydrodeoxygenation pathway). This difference on reaction pathways was attributed to the electron density of the metal sites. Catalysts with lower electron density of metal site favored C12 hydrocarbons products because positive charge in metal site increases its electrophilicity. As consequence, they may preferentially adsorb the oxygen atom of the group C=O, resulting in the activation of C=O group and its hydrogenation to produce C12 (hydrodeoxygenation pathway). Moreover, Ni_2P/SiO_2 was the most active catalyst, which was attributed to Ni_2P high superficial site density, high electronic density and Brønsted acidity [63].

Although transition metal carbides and phosphides are potential catalysts for hydrodeoxygenation reactions, they are still not widely used for commercial applications most likely due to limited control and understanding of the relation between their structure and physico-chemical properties and their catalytic performance. In this chapter we showed many works employing transition metal carbides and phosphides for deoxygenation ractions. However, the understanding of the relation between specific transition metal carbides and phosphides properties and their activity in lipid deoxygenation is unknown.

In this thesis I report my investigations on the relation between some essential transition metal carbides (Mo_2C and W_2C) and phosphides (Ni_2P) catalyst properties such as nature of the support and loading as function of their synthesis history and relate that to their performance in stearic acid deoxygenation. I also compared catalytic performance of carbides and phosphides on deoxygenation of

stearic acid at the same reaction conditions, which was still not tested and absent from the current literature.

In addition to the present Introduction chapter, this thesis is divided in 7 chapters.

Chapter 2 is a minireview on the stability of transition metal carbides in liquid phase reactions. In this chapter we discuss the relation between the deactivation routes and specific catalyst properties. For example, we show that carbon based supports are likelly a good choice for carbides in coke-sensitive reactions. Moreover, carbides with larger particle size seems to be more resistent to oxidation. This chapter provides information to avoid carbide deactivation by controlling catalyst properties and reaction conditions. In **chapter 3** we explore the role of different carbon based supports – activated carbon (AC), carbon nanofibers (CNF) and carbon-covered alumina (CCA) – on the activity and selectivity of supported W_2C catalysts for hydrodeoxygenation of stearic acid. Our results demonstrate that the support did not have a significant influence on the catalytic acitivity of carbides but it influenced the product distribution, what was attributed to differences in the support pore size and acidity. For instance, the larger pore size of W_2C/CNF favoured the production of C18-unsaturated at conversion rates below 30% while the higher acidity of W_2C/CCA favoured the production of C18-unsaturated at conversion rates above 50%. In **chapter 4**, we compared, for the first time, the catalytic performance of transition metal carbide (Mo_2C/CNF) and phosphide (Ni_2P/CNF) in the hydrodeoxygenation of stearic acid. While Mo_2C/CNF favored the hydrodeoxygenation (HDO) pathway with C18 hydrocarbon as the main product, Ni_2P/CNF favored the hydrogenation of carboxilic acid followed by the decarbonylation of aldehyde (HDCO pathway), resulting in C17 hydrocarbon as the main product. Density-functional-theory (DFT) calculations were performed to provide information about the activation energy of the C-C and/or C-OH bonds involved in the reaction. In **chapter 5**, in turn, we focus on synthesis method effects on molybdenum carbide phase and their activity and selectivity in stearic acid HDO. We show that the formation of alpha or beta molybdenum carbide depends on the Mo/C ratio employed during the catalyst synthesis. Furthermore we show that α-MoC_{1-x}/CNF presented a better catalytic performance (in weight basis) than β-Mo_2C/CNF due to the α-MoC_{1-x}/CNF lower site density, what makes the Mo atoms more accessible for large reactant molecules such as stearic acid. In **chapter 6,** we investigate the influence of loading and particle size of Ni_2P/AC in stearic acid HDO. Although particle size had no influence on catalytic activity, it influenced product distribution, with small particles favouring the HDCO pathway (hydrogenation of carboxilic acid followed by the decarbonylation

of aldehyde) and big particles favouring the decarbonylation/decarboxylation (DCO) pathway. We suggest that the difference in product distribution and consequently in the reaction pathways over nickel phosphide with different particle size is related to differences in concentration of Ni(1) and Ni(2) type sites in the catalysts. In **chapter 7** we investigated the decrease of nickel phosphide synthesis temperature by addition of small amounts of different noble metals. By the addition of 1% Pd, Rh or Pt, the synthesis temperature of Ni_2P/SiO_2 decreased around 200 °C, via hydrogen spillover. Finally, in **chapter 8** we discuss our main findings and present arguments to support Mo/W-carbides and Ni-phosphides as potential substitutes of noble metals in vegetable oil deoxygenation reactions.

Figure 7 presents a schematic overview of this thesis with the main subjects studied in each chapter.

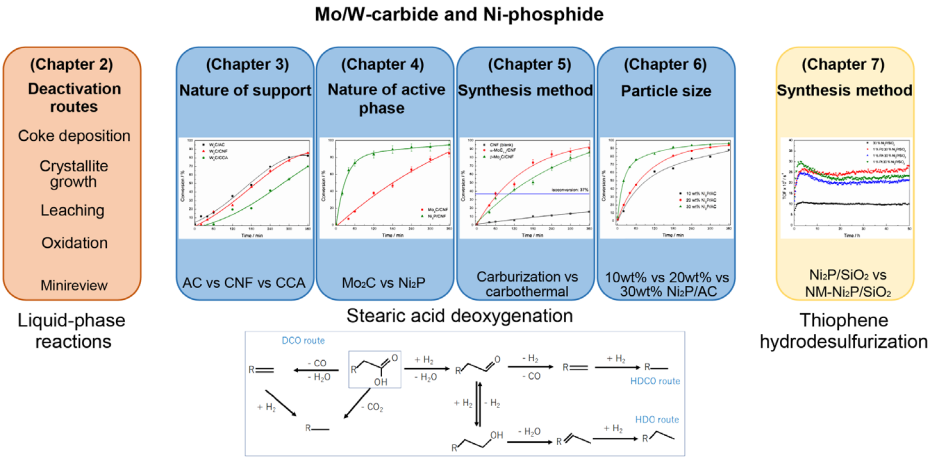

Figure 7. Schematic overview of the thesis.

References

[1] I. Chorkendorff and J. W. Niemantsverdriet, Concepts of Modern Catalysis and Kinetics, Second Edition, Published by Willey-Vch, 2007.
[2] Market Report – Global Catalyst Market, Third Edition, Published by Acmite Market Intelligence, March 2015.
[3] C. H. Bartholomew and R. J. Farrauto, Fundamentals of Industrial Catalytic Processes, Second Edition, Published by John Wiley & Sons, 2011.
[4] S. T. Oyama, Catal. Today (1992), 15, 179 – 200.
[5] D. Kubicka, J. Horácek, M. Setnicka, R. Bulánek, A. Zukal, I. Kubicková, Appl. Catal. B: Environm. (2014), 145, 101 – 107.
[6] J. M. Martínez de la Hoz, P. B. Balbuena, J. Phys. Chem. C (2011), 115, 21324 – 21333.
[7] F. G. Baddour, C. P. Nash, J. A. Schaidle, D. A. Ruddy, Angew. Chem. Int. Ed. (2016), 55, 9026 – 9029.
[8] B. Dhandapani, T. St. Clair, S. T. Oyama, Appl. Catal. A: Gen. (1998), 168, 219 – 228.
[9] C. Li, M. Zheng, A. Wang, T. Zhang, Energy Environ. Sci. (2012), 5, 6383 – 6390.
[10] J. B. Claridge, A. P. E. York, A. J. Brungs, C. M.-Alvarez, J. Sloan, S. C. Tsang, M. L. H. Green, J. Catal. (1998), 180, 85 – 100.
[11] J.-S. Choi, G. Bugli, G. D.-Mariadassou, J. Catal. (2000), 193, 238 – 247.
[12] H. Y. Zhao, D. Li, P. Bui, S. T. Oyama, Appl. Catal. A: Gen. (2011), 391, 305 – 310.
[13] R. H. Bowker, M. C. Smith, M. L. Pease, K. M. Slenkamp, L. Kovarik, M. E. Bussell, ACS Catal. (2011), 1, 917 – 922.
[14] R. B. Levy, M. Boudart, Science (1973), 181, 547 – 549.
[15] W. Li, B. Dhandapani, S. T. Oyama, Chem. Lett. (1998), 27, 207 – 208.
[16] R. W. Gosselink, S. A. W. Hollak, S.-W. Chang, J. van Haveren, K. P. de Jong, J. H. Bitter, D. S. van Es, ChemSusChem (2013), 6, 1576 – 1594.
[17] www.biobasedeconomy.nl Accessed in 12th April 2017.
[18] P. Gallezot, Chem. Soc. Rev. (2012), 41, 1538 – 1558.
[19] OPEC Secretariat, OPEC Energy Review (2015), 39, 349 – 375.
[20] BP Statistical Review of World Energy June 2016. Accessible at bp.com/statisticalreview.
[21] O. C. Eneh, Journal of Applied Sciences (2011), 11, 2084 – 2091.
[22] A. I. Waddams, Chemicals from Petroleum, 1973, John Murray, London.
[23] C. N. Kimberlin, J. Chem. Educ (1957), 34, 569 – 569.
[24] E.O. Arene and T. Kitwood, An introduction to the chemistry of carbon compounds, 1979, Longman Group Ltd., London.
[25] A. Züttel, A. Remhof, A. Borgschulte, O. Friedrichs, Phil. Trans. R. Soc. A (2010), 368, 3329 – 3342.
[26] N. Abas, A. Kalair, N. Khan, Futures (2015), 69, 31 – 49.
[27] Eidgenössischen Technischen Hochschule Zürich. 2000 Magazine bulletin No. 276. Zurich, Switzerland: ETH.
[28] M. K. Hubbert, Nuclear energy and fossil fuels. Drilling and Production Practice, Publication No. 95. Washington, DC: American Petroleum Institute & Shell Development Co.
[29] V. K. Arora, J. F. Scinocca, G. J. Boer, J. R. Christian, K. L. Denman, G. M. Flato, V. V. Kharin, W. G. Lee, W. J. Merryfield, Geophys. Res. Lett. (2011), 38, 1 – 6.
[30] Energy, Climate Change & Environment – 2016 Insights. International Energy Agency, France, accessible at www.iea.org.
[31] G. W. Huber, S. Iborra, A. Corma, Chem. Rev. (2006), 106, 4044 – 4098.
[32] F. Ma, M. A. Hanna, Bioresour. Technol. (1999), 70, 1 – 15.

[33] S. N. Naik, V. V. Goud, P. K. Rout, A. K. Dalai, Renew. Sust. Energ. Rev. (2010), 14, 578 – 597.
[34] A. J. Ragauskas, C. K. Williams, B. H. Davison, G. Britovsek, J. Cairney, C. A. Eckert, W. J. Frederick Jr., J. P. Hallet, D. J. Leak, C. L. Liotta, J. R. Mielenz, R. Murphy, R. Templer, T. Tschaplinski, Science (2006), 311, 484 – 489.
[35] A. Corma, S. Iborra, A. Velty, Chem. Rev. (2007), 107, 2411 – 2502.
[36] P. Mäki-Arvela, I. Kubickova, M. Snare, K. Eränen, D. Yu. Murzin, Energy Fuels (2007), 21, 30 – 41.
[37] S. Nizamuddin, H. A. Baloch, G. J. Griffin, N. M. Mubarak, A. W. Bhutto, R. Abro, S. A. Mazari, B. A. Ali, Renew. Sust. Energ. Rev. (2017), 73, 1289 – 1299.
[38] B. Peng, Y. Yao, C. Zhao, J. A. Lercher, Angew. Chem. Int. Ed. (2012), 51, 2072 – 2075.
[39] E. Santillan-Jimenez, T. Morgan, J. Lacny, S. Mohapatra, M. Crocker, Fuel (2013), 103, 1010 – 1017.
[40] I. Kubickova, D. Kubicka, Waste Biomass Valori. (2010), 1, 293 – 308.
[41] L. A. Sousa, J. L. Zotin, V. Teixeira da Silva, Appl. Catal. A: Gen. (2012), 449, 105 – 111.
[42] R. W. Gosselink, D. R. Stellwagen, J. H. Bitter, Angew. Chem. Int. Ed. (2013), 52, 5089 – 5092.
[43] H. Shi, J. Chen, Y. Yang, S. Tian, Fuel Process. Technol. (2014), 118, 161 – 170.
[44] S. T. Oyama, X. Wang, Y.-K. Lee, W.-J. Chun, J. Catal. (2004), 221, 263 – 273.
[45] V. N. Bui, D. Laurenti, P. Afanasiev, C. Geantet, Appl. Catal. B: Environm. (2011), 101, 239 – 245.
[46] M. Ruinart De Brimont, C. Dupont, A. Daudin, C. Geantet, P. Raybaud, J. Catal. (2012), 286, 153 – 164.
[47] C. Dupont, R. Lemeur, A. Daudin, P. Raybaud, J. Catal. (2011), 279, 276 – 286.
[48] A. M. Robinson, J. E. Hensley, J. W. Medlin, ACS Catal. (2016), 6, 5026 – 5043.
[49] D. Kubicka, L. Kaluza, Appl. Catal. A: Gen. (2010), 372, 199 – 208.
[50] D. Kubicka, J. Horacek, , Appl. Catal. A: Gen. (2011), 394, 9 – 17.
[51] T. Morgan, D. Grubb, E. S.-Jimenez, M. Crocker, Top. Catal. (2010), 53, 820 – 829.
[52] I. Simakova, O. Simakova, P. Mäki-Arvela, A. Simakov, M. Estrada, D. Yu. Murzin, Appli. Catal. A: Gen. (2009), 355, 100 – 108.
[53] I. Kubickova, M. Snare, K. Eränen, P. Mäki-Arvela, D. Yu. Murzin, Catal. Today (2005), 106, 197 – 200.
[54] P. T. Do, M. Chiappero, L. L. Lobban, D. E. Resasco, Catal. Lett. (2009), 130, 9 – 18.
[55] M. Chiappero, P. T. M. Do, S. Crossley, L. L. Lobban, D. E. Resasco, Fuel (2011), 90, 1155 – 1165.
[56] J. P. Ford, J. G. Immer, H. H. Lamb, Top. Catal. (2012), 55, 175 – 184.
[57] U.S. Geological Survey, 2017, Mineral commodity summaries 2017: U.S. Geological Survey, 202 p., http://doi.org/10.3133/70180197.
[58] E. Furimsky, Appl. Catal. A: Gen. (2003), 240, 1 – 28.
[59] R. Prins, M. E. Bussel, Catal. Lett. (2012), 142, 1413 – 1436.
[60] I. I. Abu, K. J. Smith, J. Catal. (2006), 241, 356 – 366.
[61] A. Montesinos-Castellanos, T. A. Zepeda, B. Pawelec, E. Lima, J. L. G. Fierro, A. Olivas, J. A. de los Reyes H., Appl. Catal. A: Gen. (2008), 334, 330 – 338.
[62] Y. Kanda, C. Temma, K. Nakata, T. Kobayashi, M. Sugioka, Y. Uemichi, Appl. Catal. A: Gen. (2010), 386, 171 – 178.
[63] J. Chen, H. Shi, L. Li, K. Li, Appl. Catal. B: Environm. (2014), 144, 870 – 884.

[64] Y. Yang, C. O.-Hernández, V. A. de la Pena O'Shea, J. M. Coronado, D. P. Serrano, ACS Catal. (2012), 2, 592 – 598.
[65] V. M. Whiffen, K. J. Smith, Energy Fuels (2010), 24, 4728 – 4737.
[66] S. T. Oyama, T. Gott, H. Zhao, Y.-K. Lee, Catal. Today (2009), 143, 94 – 107.

Chapter 2

Stability of transition metal carbides in liquid phase reactions relevant for biomass-based conversion

This chapter was published in adapted form as:
L. Souza Macedo, D. R. Stellwagen, V. Teixeira da Silva, J. H. Bitter, Stability of Transition-metal Carbides in Liquid Phase Reactions Relevant for Biomass-Based Conversion, ***ChemCatChem***, 7, **2015**, 2816 – 2823.

1. Introduction

Before the petroleum era in the XIXth century, biomass was the most prominent feedstock used to satisfy society's needs for food, feed, energy, and materials. However, in mid XXth century petroleum arose as a cheap energy carrier and versatile feedstock for materials, which facilitated industrialization and improved the quality of life [1]. In recent years, however, it has been realized that fossil resources besides contributing to environmental pollution are not renewable therefore use of biomass as energy carrier has regained in interest. In addition to being renewable, biomass holds several advantages such as decreasing our dependency on limited fossil resources, diversification of resources, increased sustainability and potential for regional and rural development [2].

To convert feedstocks currently 85% of all industrial processes use one or more catalytic steps [3]. Therefore catalysis and catalyst development is a crucial element in developing industrial processes. With the shift from fossil resources to biomass based resources new challenges arise for catalysis. These challenges relate to the different nature of the feedstock. A general comparison between the elemental composition of different types of biomass and crude oil is given in Table 1. The most important difference is the higher oxygen content in biomass and the presence of water in biomass. Therefore, to arrive at 'drop-in' molecules *i.e.*, molecules which are the same or very similar to those which are currently used, deoxygenation is an important reaction as well as processing under aqueous conditions. Both possess challenges for current catalytic conversion. Since heterogeneous catalysts are easier to separate from a reaction mixture and have, in general, a high thermal stability [4], we will focus in this mini review on the use of heterogeneous catalysts. Specifically we will focus on metal (Mo, W) carbide based catalysts.

Up to now often, though not exclusively, noble metal based catalysts are used to process biomass-based feedstock. The main reason for that is the stability of noble metals under the demanding conditions needed for the biomass-based conversions especially acidic, basic and aqueous conditions [5]. However, noble metals are scarce and replacing them by more readily available metals will decrease the dependency on a limited number of metal resources. Non-noble metals such as Fe, Co, Ni, Cu and transition metal carbides are able to replace noble metals (see below for some examples). Levy and Boudart [6] showed that W-carbide and Pt have similarities in electronic structure and in catalytic behaviour in the formation of water from hydrogen and oxygen as well as in isomerization of 2,2-dimethylpropane to 2-methylbutane. Later, Oyama *et al.* [7] showed that group 6 metal carbides were active for a series of reactions such as ammonia synthesis and cyclohexene hydrogenation. Iglesia *et al*. showed that W-carbides can replace

Pt in hydro-isomerization reactions [8, 9, 10] and found out that the performance of the carbides depended strongly on their pre-treatment. W-carbide resembled Pt but its performance depended crucially on the presence of oxygen-containing species on the surface, *i.e.*, oxides and/or oxy-carbides.

Only recently transition metal carbides were shown to be active for biobased conversions [5, 11-21]. Thus, transition metal carbides can replace noble metals in biomass-based conversion and sometimes they even outperform the noble metals, for example with respect to selectivity for hydrodeoxygenation of biobased conversion. The carbides are highly selective in HDO of vegetable oils to hydrocarbons where they selectively cleave C – O bonds scissions without C – C bond cleavage [16, 22]. Furthermore, Gosselink *et al.* [23, 24] showed when using carbides for HDO high yields of (valuable) unsaturated compounds could be obtained, even in the presence of high pressures of H_2. When noble metals were employed as catalyst for that reaction, only saturated products were obtained.

Though activity of transition metal carbide has been described in literature, the stability of this type of catalysts which is crucial for industrial implementation gained less attention. Therefore this mini review focuses on the stability of transition metal carbides, especially W and Mo carbide, which are the most used as potential replacements of noble metals.

To set the mind on the type of reactions we highlight here some relevant results for the use of noble and non-noble metals in biomass-based conversions are given first.

Table 1. Elemental composition of some biomass sources and crude oil.

	Alfafa stems	**Wheat straw**	**Rice hulls**	**Switch grass**	**Sugar cane bagasse**	**Willow wood**	**Crude oil**
	(wt % dry mass) [25]						(wt %) [5]
Carbon	47.2	44.9	38.8	46.7	48.6	49.9	85.2
Hydrogen	6.0	5.5	4.8	5.8	5.9	5.9	12.8
Oxygen	38.2	41.8	35.5	37.4	42.8	41.8	0.1
Nitrogen	2.7	0.4	0.5	0.77	0.2	0.6	0.1
Sulphur	0.2	0.2	< 0.1	0.2	< 0.1	0.1	1.8
Chlorine	0.5	0.2	0.1	0.2	< 0.1	< 0.1	-
Ash	5.2	7.0	20.3	8.9	2.5	1.7	-
Total	100	100	100	100	100	100	100

Many authors employed noble metals as active phase in hydrodeoxygenation reactions of fatty acids [26-29] and triglycerides [30, 31] achieving high conversion and selectivity. Both the active phase (metal) and support properties define the reaction pathway *i.e.*, decarbonylation (removal of oxygen as CO with the concomitant formation of an alkene), decarboxylation (removal of oxygen as CO_2 with the formation of an alkane) or hydrodeoxygenation (removal of oxygen as water with the use of hydrogen) [see [24] and the references therein for a review on this topic]. Peng *et al*. [32, 33] reported differences in selectivity when Ni/H-β and Ni/ZrO_2 were used for deoxygenation of microalgae oil. Whilst over the former catalyst mainly hydrodeoxygenation products were formed, over the later mainly decarbonylation/decarboxylation products were obtained. The authors suggested that the difference in acidic properties of supports was the main cause for the difference in selectivity. The presence of Brønsted acid sites in zeolites may facilitate the dehydration step in hydrodeoxygenation, thus favouring this route over decarbonylation/decarboxylation when Ni/H-β was employed as catalyst. Gao *et al.* [34] studied deoxygenation of guaiacol, a model compound for lignin, and showed that the nature of the metal (Pt, Pd, Ru, Ru) supported on carbon has a significant influence on the selectivity of the deoxygenation reaction (Figure 1). The most pronounced difference was the formation of phenol over Pd, Rh and Ru while when Pt was used besides phenol also a significant amount of cyclopentanone was produced. This result remains an enigma up to now.

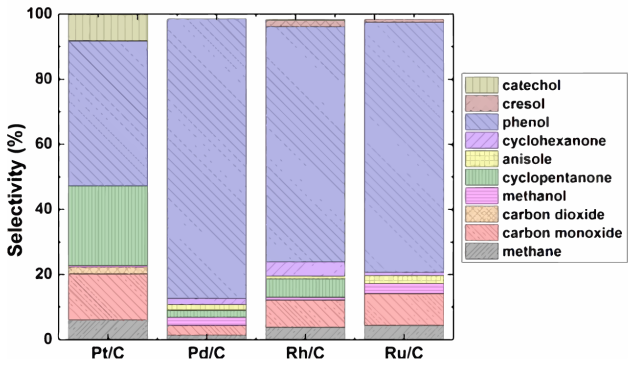

Figure 1. Distribution of major products in deoxygenation of guaiacol using carbon supported noble metal catalysts (Reprinted with permission from [34]. Copyright 2018 American Chemical Society).

Non-noble metals, e.g. Ni, were also shown to be active for deoxygenation reactions. Zhao *et al*. [35], for example, used RANEY® Ni combined with Nafion/SiO_2 as catalyst for hydrodeoxygenation of bio-derived phenols to hydrocarbons. In this

reaction, RANEY® Ni acted as hydrogenation catalyst whilst Nafion/SiO_2 acted as a solid Brønsted acid catalyst for hydrolysis and dehydration, facilitating elimination of water in the hydrodeoxygenation reaction. The authors obtained 100% of conversion and 99% of selectivity to cycloalkane at 273 °C and 40 bar H_2, however, no information about stability was provided.

In a number of cases catalyst deactivation has been observed though. For example, Mäki-Arvela *et al.* [28] observed deactivation of Pd/C in deoxygenation of lauric acid in the first hour of reaction at 270 °C and 10 bar. This deactivation was attributed to poisoning by product gases (CO and CO_2) and coke deposition.

Conventional hydroprocessing catalysts, such as sulphided $CoMo/Al_2O_3$ and $NiMo/Al_2O_3$, are also being used [36-41] for deoxygenation reactions of either lipid based feedstocks [36, 38, 39] and lignin based feedstocks [37, 40, see 41 and the references therein for a review on this topic]. A prime industrial example of deoxygenation is the production of biodiesel by hydrogenation from lipid based feedstocks by Neste Oil [42]. The stability of these (sulphided) catalysts remains a point of concern. Deactivation of these catalysts can be caused by active site poisoning by strongly adsorbing species, pore mouth constriction and blockage, and sintering of active phase [43]. Furthermore, the sulphides can deactivate due to sulphur loss from the active sites. In the latter case their activity can be stabilized by adding sulphur containing compounds in the feedstock however leached sulphur can end up in the end product which is highly undesired [44].

For the carbide based catalysts, the topic of this mini review, the role of active phase [14], support [20] and crystallite size [21] on activity and selectivity in hydrodeoxygenation reactions has been described before. However the role of these parameters on the stability of metal carbides is not well-studied. Therefore, in this short review we will provide an overview on the stability of metal carbides in liquid phase reactions. We will focus on the influence of catalyst properties such as type of support and active phase and reaction parameters such as temperature and solvent on the pathway of catalyst deactivation.

There are four important pathways for catalyst deactivation [43, 45] *i.e.*,

- coke deposition
- crystallite growth (sintering and Ostwald ripening)
- leaching
- oxidation

In the next sections we will discuss the influence of these four issues on the overall performance of transition metal carbide based catalysts when they are used in liquid phase transformation of biomass-based molecules.

2 Mechanisms of deactivation

2.1 Coke deposition

Coke is defined as a product of decomposition or condensation of a carbon-based material on a catalyst surface. Coke formation can negatively influence the activity of a catalyst in two ways either via chemical modification of active site or by physically blocking the active site. When coke chemisorbs on a catalyst surface it acts as a catalyst poison due its strong interaction with the active sites making it inaccessible for the reactants. For physical blocking the coke does not necessarily interact with the active site. In that case coke can block part of the catalyst thus preventing the reactants to reach the active site e.g. blocking pores or covering the surface of catalyst (Figure 2) [45].

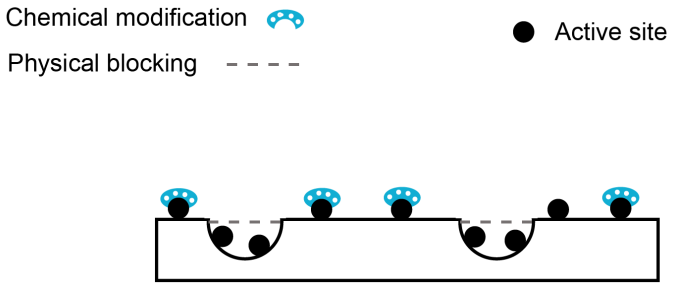

Figure 2. Scheme of ways of coke deposition on catalyst surface: chemical modification and physical blocking.

Coke deposition can be responsible for a decrease in catalytic activity for some types of reaction, classified as coke-sensitive reactions. Examples of this class of reactions are catalytic cracking [46] and hydrogenolysis [47]. On the other hand, in coke-insensitive reactions, the amount of coke is not very important for catalyst activity. In that class of reactions the active site is kept clean by hydrogenating the formed coke species mainly to methane which then desorbs from the catalyst surface [48]. Some reactions can change from coke-sensitive to coke-insensitive depending on reaction conditions (the examples given first are for gas-phase reactions). Pham-Huu *et al.* [49], for example, showed that Mo_2C deactivated when the hydrogenolysis of methylcyclopentane (MCP) was performed at 6 bar and 350 ^{o}C due to coke deposition. However, when the pressure was increased to 18 bar catalyst deactivation was much less pronounced, showing that pressure is a key parameter on catalyst stability for this reaction. Ribeiro *et al.* [10] synthesized WC and β-W_2C by carburization of WO_3 and used the carbides as catalysts for alkane hydrogenolysis. These catalysts deactivated rapidly by strong adsorption of carbon fragments formed from alkanes however that resulted in a high selectivity to

hydrogenolysis product. A subtle treatment of the carbide surface with oxygen lead to a decrease in hydrogenolysis and deactivation rates. Oxygen-exposed carbides catalyzed n-hexane and n-heptane isomerization with high selectivity *i.e.* the selectivity changed from hydrogenolysis for the carbides to isomerization for the oxygen treated carbides.

Bartholomew *et al*. [50, 51] evaluated the influence of the support on coke formation for both carbon monoxide and carbon dioxide hydrogenation reactions using nickel as active phase. They concluded that the decreasing order for coke deposition rate was Ni/TiO_2 > Ni/Al_2O_3 > Ni > Ni/SiO_2. This trend was attributed to changes in electronic properties of Ni due to strong interaction with support, migration of suboxide species from support onto the metal and differences in nickel crystallite sizes.

To the best of our knowledge there are two cases where coke formation was claimed to be the primary cause of deactivation for carbide catalysts in liquid phase (Table 2). Zhang *et al.* [52] studied the catalytic activity of NiMo carbide supported on silica for the hydrodeoxygenation of ethyl benzoate, acetone and acetaldehyde (T= 300 °C, p= 50 bar). Temperature Programmed Oxidation (TPO) experiments were performed with fresh and spent catalysts to investigate coke formation (Figure 3). A weight loss up to 150 °C was observed which was ascribed to the desorption of water from carbide surface (circle remark in graph). Above 150 °C, a weight increase was observed for Mo and NiMo carbides profiles, which was attributed to the oxidation of lattice carbon resulting in WO_3 and CO_2 (rectangle remark in graph). For the passivated Mo-carbide also a weight loss was observed at 600 °C (rounded rectangle remark in graph), which was ascribed to oxidation of carbon residues present on the catalyst surface after catalyst synthesis (the catalyst was synthesized by carburization with of methane). For used NiMo-carbide, the same weight loss between 150 and 390 °C (rectangle remark in graph) was observed as for the fresh NiMo-carbide catalsyts, indicating the maintenance of the basic carbide structure. However for the spent catalysts also a clear weight loss was observed above 600 °C (rounded rectangle remark in graph) which has been assigned to the oxidation of coke species formed during reaction.

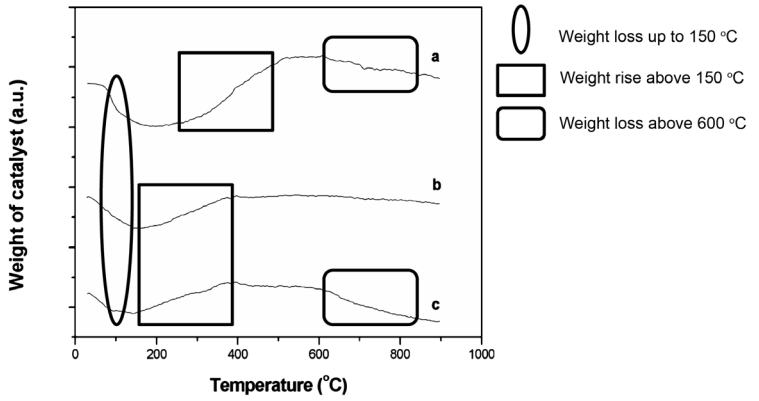

Figure 3. TPO profiles of (a) passivated Mo carbide, (b) passivated NiMo carbide, and (c) used NiMo carbide used for hydrodeoxygenation of ethyl benzoate. (Reprinted (adapted) with permission from [52]. Copyright 2018 American Chemical Society).

The catalysts described up to now are silica supported carbides which are applied in liquid phase reactions. The number of studies on the role of coke formation on carbon supported carbide catalysts seems to be limited. The paper from Jongerius *et al*. [53] is, to the best of our knowledge, the only one that used carbon supported carbide which suggested that coke formation could be the reason of catalyst deactivation. In that paper, the authors describe the use of Mo_2C/CNF for hydrodeoxygenation of guaiacol (350 °C and 50 bar H_2). After use, XRD did not show reflections related to Mo-oxide therefore the observed deactivation could not be ascribed to oxidation of the catalyst. Therefore, despite the fact that some amorphous oxide species could have been formed on the catalyst surface the authors suggested that deactivation occurred due another reason. Though the main reason for deactivation was suggested to be sintering (see below) it was also suggested that coke formation or encapsulation of carbide particles in the carbon contributed to deactivation although proof is limited.

As carbon is a stable support under relevant reaction conditions for biomass-based conversion it is worth to study carbon supported carbides in more detail. A major drawback of carbon based catalysts is, however, that once catalysts deactivated by coke formation, regeneration can be cumbersome since oxidative regeneration might result in support degradation (oxidation). Regeneration under reducing conditions (hydrogenation) has been shown to be successful though [49].

Table 2. Description of works that reported coke formation as the main cause of catalyst (carbides) deactivation in liquid phase reactions.

Reaction	Catalyst	Conversion	Degree of deactivation	Reference
HDO of ethyl benzoate	$NiMoC/SiO_2$	99 % (initial)	32.3 % (72 h)	[52]
HDO of guaiacol	Mo_2C/CNF	68 % (2 run)	25 % (3 run)	[53]

2.2 Crystallite growth

During crystallite growth the active surface area of the catalyst is lost due to an increase in the crystallite size. Two major routes of crystallite growth exist:

1. coalescence *i.e.* the merger of two smaller crystallites to a bigger one or via species moving over the surface of the support. This process is often referred to as sintering;

2. Ostwald ripening, where smaller particles and species dissolve into solution or evaporate to the gas phase followed by precipitation on larger particles [54].

For both mechanisms the driving force is the lower surface energy of larger particles thus these particles are thermodynamically more stable. These main mechanisms of crystallite growth have been reviewed [45, 55]. Once crystallite growth is difficult to revert its prevention is much easier than its cure.

Some key parameters of the catalyst and reaction conditions have been identified to influence crystallite growth of supported metal nanoparticles such as temperature, atmosphere, metal type, support surface area, texture and porosity [45]. Besides these characteristics, rate of sintering is also influenced by factors like presence of water vapour, low Tamman temperature of metals and strength of metal-support interaction. Fuentes [56], Baker *et al.* [57] and Bartholomew *et al.* [58, 59] showed that it is possible to quantitatively determine the effects of temperature, atmosphere, metal, promoter and support by fitting the sintering kinetic data to the general power law expression (GPLE).

The activity of a catalyst expressed as moles of feedstock converted per mol of accessible site per unit of time (Turn Over Frequency or TOF) can either increase, decrease or remain unaffected as function of increasing particle size [56]. The former two classes are classified as structure sensitive while the latter is classified as a structure insensitive reaction. Thus, crystallite growth can be an important mechanism of catalyst deactivation in structure sensitive reactions.

Some authors identified sintering as one of the reasons of catalyst

deactivation. Li *et al.* [60] used Ni-Mo_2C/SiO_2 and Ni-W_2C/SiO_2 for alkane production with 2-methylfuran and mesityl oxide from lignocellulose. An alkylation reaction between 2-methylfuran and mesityl oxide was performed and, subsequently, HDO of the alkylation products was carried out at 300 ºC. TEM images (Figure 4) showed that particles of Ni-Mo_2C/SiO_2 and Ni-W_2C/SiO_2 slightly increased after reaction from 8.2 to 9.3 nm (Ni-Mo_2C/SiO_2) and from 5.8 to 6.3 nm (Ni-W_2C/SiO_2), which was attributed to particle agglomeration. However, authors identified the occurrence of oxidation of carbides after reaction by XPS analysis, thus the increasing in particle size can be related to this change in active phase instead of to the sintering of carbides particles. Despite the fact that Li *et al*. [60] observed particle growth, no direct relation with activity could be established in this case.

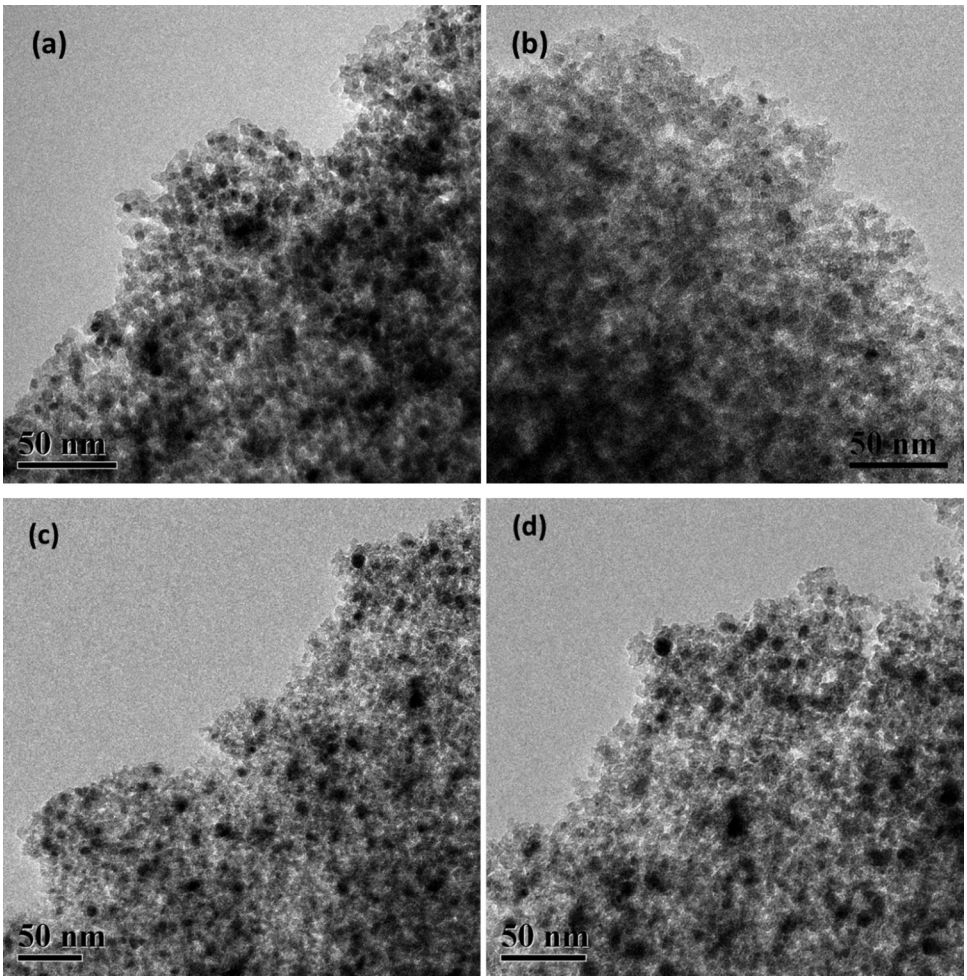

Figure 4. TEM images of (a) fresh Ni-Mo_2C/SiO_2, (b) used Ni-Mo_2C/SiO_2, (c) fresh Ni-W_2C/SiO_2 and (d) used Ni-W_2C/SiO_2 [60].

Jongerius *et al*. [53] also identified sintering as a reason for catalyst deactivation in liquid phase reaction. Authors used W_2C/CNF for hydrodeoxygenation of guaiacol (350 °C and 50 bar H_2) and tested catalyst stability reusing it after re-carburation process. They observed an increasing in particle size from 4 nm for the fresh catalyst to 9 nm for re-carburized sample and attributed sintering to the loss in activity (from 66% in the first run to 48% in the run after re-carburation).

2.3 Leaching

Leaching is the process of dissolution of part of the catalysts active phase. This can lead to loss of active material or to homogeneous catalysed reactions. Li *et al.* [61] studied the leaching of Ni and W from Ni-W_2C/AC during the hydrocracking of woody biomass at 235 °C and 60 bar H_2. ICP (inductively coupled plasma) was used to identify the amount of leached material. The authors observed that after the third recycle, total Ni and W leaching reached 19,5% and 11,2% of the initial amount, respectively. Ji *et al.* [62] studied the leaching of Ni and W from Ni-W_2C/AC used for the conversion of cellulose into ethylene glycol. After the third run, ICP analysis indicated that the amount of Ni and W in liquid products was 58,1 and 123,2 ppm, representing a loss of 18,9 %Ni and 10,9 %W. At the same time the ethylene glycol yield decreased from 73 to 57,8% indicating that leaching was an important reason for catalyst deactivation.

We noted that all papers describing the deactivation by leaching of the carbides used catalysts based on carbon supports (Table 3) and water as solvent. A strong interaction between carbide phase and the carbon support is not guaranteed. This in combination with the polar solvent can be a reason for the observed leaching.

Table 3. Articles reporting leaching as the main cause of catalyst (carbides) deactivation in liquid phase reactions.

Reaction[1]	**Catalyst**	**Solvent**	**Conversion**	**Degree of deactivation after 2nd run**	**Ref**
Cellulose conversion to ethylene glycol T = 245 °C P = 60 bar	Ni-W_2C/AC	Water	73 %	15.1 %	[62]

Hydrocracking of raw woody T = 235 °C P = 60 bar	Ni-W_2C/AC	Water	50 %	14 %	[61]

[1]Only reference [61] mentioned average catalyst particle size, which was 9,7 nm.

2.4 Oxidation

Carbides are stable catalysts for many kinds of gas phase reactions such as HDS [63-64]. However, because of their pyrophoric character, their contact with oxygen should be prevented in order to avoid the loss of active phase due to oxidation and burning of pyrolytic carbon deposited on its surface during their synthesis.

In oxidizing conditions metal oxides are more stable compared to the carbides. Calculations of ΔG (free Gibbs energy) for the oxidation of Mo_2C in both oxygen and water were done by Ruddy *et al*. [65]. For all concentrations of O_2 the ΔG of Mo-carbide oxidation was strongly negative (ΔG varied from -1077 to -1545 kJ mol^{-1} depending on O_2 concentration ranging from 2,5 to 4 mols of O_2 per mol of Mo_2C). For oxidation of Mo_2C by water the ΔG of oxidation becomes negative (ΔG = -17 kJ mol^{-1}) above stoichiometric amounts of water. Thus, oxidation is always a risk for this type of catalysts. The driving force for oxidation in aqueous conditions (without oxygen) is obviously lower than in air though oxidation in water can still be expected. Please note that the thermodynamic data is based on bulk compounds at 300 °C. Smaller particles might be easier to oxidize [21] and oxidation of W_2C is more favourable than of Mo_2C surface [53].

Table 4 gives an overview of studies reporting oxidation of Mo,W-carbides as main reason for catalyst deactivation in liquid phase. The reactions range from hydrodeoxygenation of guaiacol, oleic acid, 2-methylfuran and mixture of phenol and 1-octanol and mesityl oxide to hydrocracking of raw woody to deoxygenation of stearic acid.

Jongerius *et al.* [53] and Hollak *et al.* [23] used W_2C/CNF for the hydrodeoxygenation of guaiacol and oleic acid, respectively (350 °C and 50 bar H_2). The catalysts were characterized after reaction and XRD results showed diffractions representative of a WO_x phase when samples were reused without treatment with hydrogen. When re-carburation was done after reaction [53] the carbide phase was recovered (Figure 5) although an increase in particle size caused by sintering was observed. Li *et al.* [61] also observed diffraction lines related to WO_x phase in XRD after use of Ni-W_2C/AC for hydrocracking of raw woody biomass at 235 °C and 60 bar H_2 with water as solvent. Therefore oxidation was indicated as a reason

of catalyst deactivation though together with leaching (analysed by ICP). Li *et al.* [60] used Ni-Mo_2C/SiO_2 and Ni-W_2C/SiO_2 as catalysts for HDO of products from alkylation of 2-methylfuran and mesityl oxide. XPS spectra showed that the ratio of oxide to carbide on the surface of catalysts increased after reaction from 0,71 to 0,98 for Ni-Mo_2C/SiO_2 and from 5,86 to 10,14 for Ni-W_2C/SiO_2, which was attributed to oxidation of Mo_2C and W_2C by water generated during HDO. Mortensen *et al.* [66] used Mo_2C/ZrO_2 in hydrodeoxygenation of 1-octanol and phenol at 320 °C and 100 bar and observed a deactivation of catalyst over 76 hours of reaction, with conversion decreasing from 70% to 37% for 1-octanol and from 37% to 19% for phenol. In situ XRD showed the Mo_2C was transformed to MoO_2 during reaction due to formation of water in HDO process.

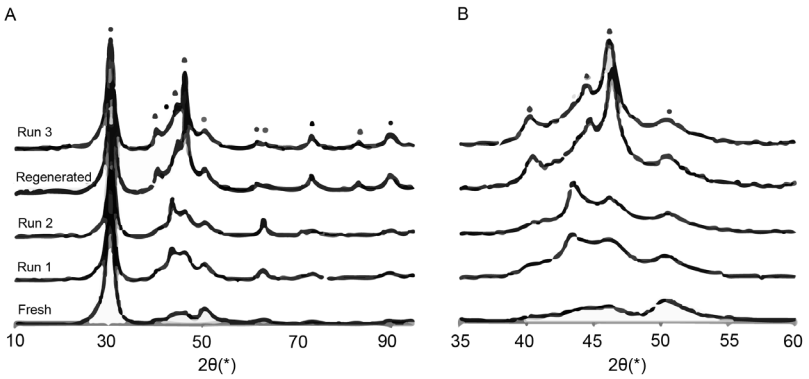

Figure 5. (a) full X-ray diffraction patterns and (b) zoomed in X-ray diffraction patterns of fresh W_2C/CNF (fresh), spent W_2C/CNF (run 1), reused W_2C/CNF (run 2), spent W_2C/CNF after reactivation at 1000 °C (regenerated), and spent reactivated W_2C/CNF (run 3). Reflections are given for graphitic carbon (●), XO_2 (■), and X_2C (▲), with X = W or Mo [53].

All works described in this section used catalysts with crystallite size lower than 20 nm (Li *et al.* [60] and Mortensen *et al.* [66] didn't give information about crystallite size) however a clear relation between particle size and oxidation rate has not been studied. However, recently, Stellwagen *et al.* [21] studied the activity and stability of tungsten and molybdenum carbide in stearic acid deoxygenation at 350 °C and 30 bar of hydrogen using both 2 and 10 nm carbide particles supported on carbon. These authors showed that 10 nm particles were more active as a result of the lower oxidation degree of the particles. Even though the reaction was performed without oxygen the small particles were still oxidized to a significant extent (Figure 6).

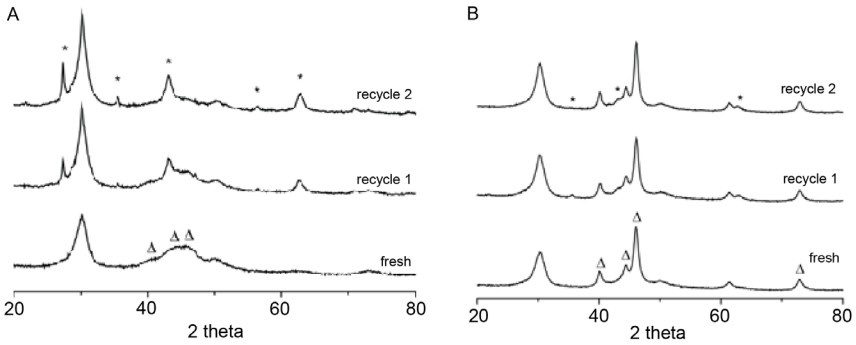

Figure 6. Fresh and spent W_2C/CNF catalysts. (a) sample with crystallite size of 2 nm. New peaks in the spent catalysts (*) can be identified as WO_2 and $WO_{2.72}$ crystallites. The original W_2C phase (Δ) disappears upon recycle. (b) sample with crystallite size 10-12 nm. The carbide structure (Δ) is observed in all diffractograms. Peaks related to trace WO_2 (*) can also be observed [21].

Table 4. Description of works that reported oxidation as the main cause of catalyst (carbides) deactivation in liquid phase reactions.

Reaction	Catalyst	Crystallite size	Conversion	[1]Degree of deactivation	Ref
HDO of guaiacol	W_2C/CNF	4 nm	66 %	27.3 (3 run)	[53]
HDO of oleic acid	W_2C/CNF	5 nm	70 %	31.4 (2 run)	[23]
Hydrocracking of raw woody	Ni-W_2C/AC	-	50 %	14 (2 run)	[61]
HDO of products of alkylation of 2-methylfuran and mesityl oxide	Ni-Mo_2C/SiO_2 Ni-W_2C/SiO_2	-	70 % 20 %	- -	[60]
HDO of phenol	Mo_2C/ZrO_2	-	37%	49 (76h)	[66]
HDO of 1-octanol	Mo_2C/ZrO_2	-	70%	47 (76h)	[66]
Deoxygenation of stearic acid	Mo_2C/CNF W_2C/CNF	2 nm 2 nm	85 % 85 %	30 (5 h) ~50 (5h)	[21]
Deoxygenation of stearic acid	Mo_2C/CNF W_2C/CNF	10 nm 10 nm	85 % 85 %	0 (5h) 0 (5h)	[21]

[1] Degree of deactivation was calculated in two ways: by difference between catalyst activity on first run and second or third run divided by activity of catalyst in first run for reactions in batch system; and by the difference between catalyst activity on the beginning of reaction (time = 0) and final reaction time divided by activity of catalyst in the beginning of reaction for continuous system.

- Information not provided.

3. Conclusions and research opportunities

Transition metal carbides are potential candidates to replace noble metal catalysts in liquid phase reactions. Especially for deoxygenation of biomass-based feedstock they hold great potential. However, their stability is not a well-studied topic until now. Only a limited number of studies explored this issue in catalysts performance although stability is a very important parameter in catalysts evaluation. This mini review shows that transition metal carbides can deactivate in liquid phase reactions by coke formation, sintering, leaching and oxidation. We have demonstrated that although there are no studies relating catalysts and reaction characteristics with each kind of deactivation route, there are some trends based on works that analysed carbides deactivation. The nature of support can influence catalyst deactivation by coke deposition and leaching. While carbon based supports seem to be a good choice for carbides in coke-sensitive reactions, once a strong interaction between these supports and carbides active phases is not guaranteed, deactivation by leaching is facilitated when carbon based materials are employed. Catalyst crystallite size can be related to catalyst deactivation by oxidation, once all works that reported catalyst deactivation by oxidation used samples with crystallite size smaller than 20 nm and it was shown that bigger crystallite size (10 nm) of carbides have more resistance to oxidation than smaller particles (2 nm). Since the application of carbides for biobased conversion has been increasing in the last years, many aspects of this catalyst can be understood for biomass conversion, especially in liquid phase reaction. As a consequence of carbides being a new class of catalyst to be employed on biomass conversion, there are not many reports regarding their stability in liquid phase reaction and about reactivating them. Thus, it is a subject for future studies, especially regarding the route of carbides deactivation. Furthermore, considering that phosphides are catalysts with different structure compared to carbides but with similar catalytic properties, the study of biomass conversion with phosphides as catalysts is also promising to the community. Some groups have already started to study phosphides as catalyst for biomass conversion in liquid phase reactions and have observed the same routes of deactivation as for carbides, such as coke deposition, leaching and oxidation [67-69]. Thus, the deeper study about deactivation of phosphides also seems to be valuable to community.

References

[1] G. W. Huber, S. Iborra, A. Corma, *Chem. Rev*. **2006**, *106*, 4044 – 4098.
[2] H. Langeveld, J. Sanders, M. Meeusen in *The Biobased Economy Biofuels, Materials and Chemicals in the Post-oil Era*, Earthscan, **2010**.
[3] K. P. de Jong (ed) in *Preparation of solid catalysts*, Wiley-VCH, **2009**.
[4] M. Heitbaum, F. Glorius, I. Escher, *Angew. Chem.* **2006**, *45*, 4732 – 4762.
[5] E. Furimsky, *Appl. Catal. A: Gen*. **2000**, *199*, 147 – 190.
[6] R. B. Levy, M. Boudart, Science **1973**, *181*, 547 – 549.
[7] S. T. Oyama, *Catal. Today* **1992**, *15*, 179 – 200.
[8] E. Iglesia, F. H. Ribeiro, M. Boudart, J. E. Baumgartner, *Catal. Today* **1992**, 15, 307 – 337.
[9] F. H. Ribeiro, R. A. Dalla Betta, M. Boudart, J. Baumgarner, E. Iglesia, *J. Catal.* **1991**, *130*, 86 – 105.
[10] F. H. Ribeiro, M. Boudart, R. A. Dalla Betta, E. Iglesia, *J. Catal.* **1991**, *130*, 498 – 513.
[11] H. H. Hwu and J. G. Chen, *Chem. Rev*. **2005**, *105*, 185 – 212.
[12] A. L. Stottlemyer, T. G. Kelly, Q. Meng, J. G. Chen, *Surf. Sci. Rep.* **2012**, *67*, 201 – 232.
[13] G. L. Bezemer, J. H. Bitter, H. P. C. E. Kuipers, H. Oosterbeek, J. E. Holewijn, X. Xu, F. Kapteijn, A. J. van Dillen, K. P. de Jong, *J. Am. Chem. Soc.* **2006**, *128*, 3956 – 3964.
[14] N. Ji, T. Zhang, M. Zheng, A. Wang, H. Wang, X. Wang, J. G. Chen, *Angew. Chem. Int. Ed.* **2008**, *47*, 8510 – 8513.
[15] W. Chen, Z. Fan, X. Pan, X. Bao, *J. Am. Chem. Soc.* **2008**, *130*, 9414 – 9419.
[16] L. A. Sousa, J. L. Zotin, V. Teixeira da Silva, *Appl. Catal. A: Gen*. **2012**, *449*, 105 – 111.
[17] M. A. Patel, M. A. S. Baldanza, V. Teixeira da Silva, A. V. Bridgwater, *Appl. Catal. A: Gen*. **2013**, *458*, 48 – 54.
[18] E. F. Mai, M. A. Machado, T. E. Davies, J. A. Lopez-Sanchez, V. Teixeira da Silva, *Green Chem.* **2014**, *16*, 4092 – 4097.
[19] E. Furimsky, *Catal. Today* **2013**, *217*, 13 – 56.
[20] Y. Qin, P. Chen, J. Duan, J. Han, H. Lou, X. Zheng, H. Hong, *R. Soc. Chem. Adv.* **2013**, *3*, 17485 – 17491.
[21] D.R. Stellwagen, J.H. Bitter, *Green Chem.* **2015**, *17*, 582 – 593.
[22] H. Ren, W. Yu, M. Salciccioli, Y. Chen, Y. Huang, K. Xiong, D. G. Vlachos, J. G. Chen, *ChemSusChem* **2013**, *6*, 798 – 801.
[23] S. A. W. Hollak, R. W. Gosselink, D. S. van Es, J. H. Bitter, *ACS Catal.* **2013**, *3*, 2837 – 2844.
[24] R. W. Gosselink, S. A. W. Hollak, S.-W. Chang, J. van Haveren, K. P. de Jong, J. H. Bitter, D. S. van Es, *ChemSusChem* **2013**, *6*, 1576 – 1594.
[25] B. M. Jenkins, L. L. Baxter, T. R. Miles Jr., T. R. Miles, *Fuel Process. Technol*. **1998**, *54*, 17 – 46.
[26] J. P. Ford, J. G. Immer, H. H. Lamb, *Top. Catal*. **2012**, *55*, 175 – 184.
[27] C. Detoni, F. Bertella, M. M. V. M. Souza, S. B. C. Pergher, D. A. G. Aranda, *Appl. Clay Sci.* **2014**, *95*, 388 – 395.
[28] P. Mäki-Arvela, M. Snare, K. Eränen, J. Myllyoja, D. Yu. Murzin, *Fuel* **2008**, *87*, 3543 – 3549.
[29] M. Snare, I. Kubicková, P. Mäki-Arvela, K. Eränen, D. Y. Murzin, *Ind. Eng. Chem. Res.* **2006**, *45*, 5708 – 5715.
[30] T. Morgan, D. Grubb, E. Santillan-Jimenez, M. Crocker, *Top. Catal.* **2010**, *53*, 820 – 829.

[31] M. Chiappero, P. T. Mai Do, S. Crossley, L. L. Lobban, D. E. Resasco, *Fuel* **2011**, *90*, 1155 – 1165.
[32] B. Peng, Y. Yao, C. Zhao, J. A. Lercher, *Angew. Chem.* **2012**, *124*, 2114 – 2117. *Angew. Chem. Int. Ed.* **2012**, *51*, 2072 – 2075.
[33] B. Peng, X. Yuan, C. Zhao, J. A. Lercher, *J. Am. Chem. Soc.* **2012**, *134*, 9400 – 9405.
[34] D. Gao, C. Schweitzer, H. T. Hwang, A. Varma, *Ind. Eng. Chem. Res.* **2014**, *53*, 18658 – 18667.
[35] C. Zhao, Y. Kou, A. A. Lemonidou, X. Li, J. A. Lercher, *ChemComm* **2010**, *46*, 412 – 414.
[36] E. Laurent, B. Delmon, *Ind. Eng. Chem. Res.* **1993**, *32*, 2516 – 2524.
[37] A. L. Jongerius, R. Jastrzebski, P. C. A. Bruijnincx, B. M. Weckhuysen, *J. Catal.* **2012**, *285*, 315 – 323.
[38] O. I. Senol, T. –R. Viljava, A. O. I. Krause, *Catal. Today* **2005**, *106*, 186 – 189.
[39] D. Kubicka, J. Horácek, *Appl. Catal. A: Gen.* **2011**, *394*, 9 – 17.
[40] Y. –C. Lin, C. –L. Li, H. –P. Wan, H. –T. Lee, C. –F. Liu, *Energ. Fuel.* **2011**, *25*, 890 – 896.
[41] Q. Bu, H. Lei, A. H. Zacher, L. Wang, S. Ren, J. Liang, Y. Wei, Y. Liu, J. Tang, Q. Zhang, R. Ruan, *Bioresource Technol.* **2012**, *124*, 470 – 477.
[42] J. Myllyoja, P. Aalta, E. Harlin, Process for the manufacture of diesel range hydrocarbons **2010**, Patent application number: 20100287821.
[43] E. Furimsky, F. E. Massoth, *Catal. Today* **1999**, *52*, 381 – 495.
[44] D. Kubica, L. Kaluza, *Appl. Catal. A: Gen.* **2010**, *372*, 199 – 208.
[45] C. H. Bartholomew, *Appl. Catal. A: Gen.* **2001**, *212*, 17 – 60.
[46] K. A. Cumming, B. W. Wojciechwski, *Cataly. Rev.* **1996**, *38*, 101 – 157.
[47] J. Barbier, *Appl. Catal.* **1986**, *23*, 225 – 243.
[48] P. G. Menon, *J. Mol. Catal.* **1990**, *59*, 207 – 220.
[49] C. P.-Huu, A. P. E. York, M. Benaissa, P. Del Gallo, M. J. Ledoux, *Ind. Eng. Chem. Res.* **1995**, *34*, 1107 – 1113.
[50] C. H. Bartholomew, M. V. Strasburg, H. –Y. Hsieh, *Appl. Catal.* **1988**, *36*, 147 – 162.
[51] C. K. Vance, C. H. Bartholomew, *Appl. Catal.* **1983**, *7*, 169 – 177.
[52] W. Zhang, Y. Zhang, L. Zhao, W. Wei, *Energ. Fuel.* **2010**, *24*, 2052 – 2059.
[53] A. L. Jongerius, R. W. Gosselink, J. Dijkstra, J. H. Bitter, P. C. A. Bruijnincx, B. M. Weckhuysen, *ChemCatChem* **2013**, *5*, 2964 – 2972.
[54] A. K. Datye, Q. Xu, K. C. Kharas, J. M. McCarty, *Catal. Today* **2006**, *111*, 59 – 67.
[55] C. H. Bartholomew, *Stud. Surf. Sci. Catal.* **1997**, *111*, 585 – 592.
[56] G. A. Fuentes, *Appl. Catal.* **1985**, *15*, 33 – 40.
[57] R. T. Baker, C. H. Bartholomew, . B. Dadyburjor, Stability of Supported Catalysis: Sintering and Redispersion, Catalytic Studies Division, Catalytica Inc., Mt. View, Califórnia, **1991**.
[58] C. H. Bartholomew, Catalysis, Specialist Periodical Report, Vol. 10, Royal Society of Chemistry, **1992**.
[59] C. H. Bartholomew, *Stud. Surf. Sci. Catal.* **1994**, *88*, 1 – 18.
[60] S. Li, N. Li, G. Li, A. Wang, Y. Cong, X. Wang, T. Zhang, *Catal. Today* **2014**, *234*, 91 – 99.
[61] C. Li, M. Zheng, . Wang, T. Zhang, *Energ. Environ. Sci.* **2012**, *5*, 6383 – 6390.
[62] N. Ji, M. Zheng, A. Wang, T. Zhang, J. G. Chen, *ChemSusChem* **2012**, *5*, 939 – 944.
[63] A. C. L. Gomes, M. H. O. Nunes, V. Teixeira da Silva, J. L F. Monteiro, *Stud. Surf. Sci. Catal.* **2004**, *154*, 2432 – 2440.

[64] C. C. Yu, S. Ramanathan, B. Dhandapani, J. G. Chen, S. T. Oyama, *J. Phys. Chem. B* **1997**, *101*, 512 – 518.
[65] D. A. Ruddy, J. A. Schaidle, J. R. Ferrell III, J. Wang, L. Moens, J. E. Hensley, *Green Chem.* **2014**, *16*, 454 – 490.
[66] P. M. Mortensen, H. W. P. de Carvalho, J. –D. Grunwaldt, P. A. Jensen, A. D. Jensen, *J. Catal.* **2015**, *328*, 208 – 215.
[67] K. Li, R. Wang, J. Chen, *Energ. Fuel.* **2011**, *25*, 854 – 863.
[68] V. M. L. Whiffen, K. J. Smith, *Top. Catal.* **2012**, *55*, 981 – 990.
[69] Z. Guanhong, Z. Mingyuan, W. Aiqin, Z. Tao, *Chinese J. Catal.* **2010**, *31*, 928 – 932.

Chapter 3

Activated carbon, carbon nanofibers and carbon-covered alumina as support for W_2C in stearic acid hydrodeoxygenation

Co-authors of this chapter are V. Teixeira da Silva and H. Bitter (manuscript in preparation)

Abstract

Deoxygenation reactions to enable the creation of fuels and chemicals from vegetable oils require the use of catalysts, but conventional hydrotreating catalysts and noble metal catalysts have drawbacks. This paper reports on an investigation of tungsten carbide (W_2C) on three types of carbon support, namely activated carbon (AC), carbon nanofibers (CNFs) and carbon-covered alumina (CCA). We evaluated their activity and selectivity in stearic acid hydrodeoxygenation at 350 ºC and 30 bar H_2. Although all three W_2C catalysts displayed similar intrinsic catalytic activities, the support did influence product distribution. At low conversions (< 5%), W_2C/AC yielded the highest amount of oxygenates relative to W_2C/CNF and W_2C/CCA. This suggests that the conversion of oxygenates into hydrocarbons is more difficult over W_2C/AC than over W_2C/CNF and W_2C/CCA, which we relate to the lower acidity and smaller pore size of W_2C/AC. The support also had an influence on the C18-unsaturated/C18-saturated ratio. At conversions below 30%, W_2C/CNF presented the highest C18-unsaturated/C18-saturated ratio in product distribution, which we attribute to the higher mesopore volume of CNF. However, at higher conversions (> 50%), W_2C/CCA presented the highest C18-unsaturated/C18-saturated ratio in product distribution, which appears to be linked to W_2C/CCA having the highest ratio of acid/metallic sites.

1. Introduction

Fossil resources like oil, gas and coal have been the main sources for the production of chemicals and fuels in the last 150 years. However, for political and environmental reasons, biomass is gaining attention as an alternative source [1]. Vegetable oils are especially interesting since their chemical structure and properties are close to those of the fuel that we currently make from crude oil. There are also important differences such as the higher viscosity and flash point as result of the higher oxygen content of vegetable oil. Therefore, vegetable oils need treatment before they can be turned into fuel-like substances. One such conversion route is microemulsification, in which the viscosity of vegetable oil is decreased by the formation of micelles with short-chain alcohols. This method results in a vegetable oil with similar combustion properties as fossil fuel [2 – 5]. Other methods to improve the combustion properties of vegetable oils are pyrolysis (in which vegetable oil is thermally decomposed leading to a mixture of olefins, paraffins, carboxylic alcohols and aldehydes) [6 – 10], transesterification (in which vegetable oil is transformed to biodiesel) [11 – 15] and deoxygenation (in which oxygen atoms of vegetable oil are removed, yielding hydrocarbons) [16 – 20].

Conventional hydrotreating catalysts (metal sulfides) are active for deoxygenation reactions, but can become deactivated due to the loss of sulfur. Their activity can be retained by adding sulfur compounds to the feed; however, this can result in traces of unwanted sulfur in the final products [19]. It is possible to avoid this drawback by using noble metals as active catalyst phase [21]. Many researchers have therefore studied deoxygenation reactions using noble metals as the active catalyst phase [22 – 26], but noble metals are scarce and their low availability makes their industrial use costly.

Transition metal carbides are potential alternatives for use in deoxygenation reactions since they have similar electronic properties as noble metal catalysts [27 – 31]. During deoxygenation of triglycerides/fatty acids in the presence of hydrogen, they promote mainly hydrodeoxygenation although products of decarbonylation/decarboxylation are also observed in lower amounts [32 – 35].

In general, the support plays an important role in catalytic activity and selectivity as the support can influence the electronic structure of the active phase by changing its density of states [36 – 38] or its dispersion [26]. In addition, support acidity may affect product distribution in several reactions by affecting the orientation of molecule adsorption [39], while physical properties of the support (e.g. pore size) may influence the diffusion of reactant and product molecules to and from the active sites [40].

Activated carbon (AC) is widely used as catalyst support [41 – 43]. Activated

carbon supports contain layers of graphene with curved sections and pronounced cross-linking. After the activation process, the carbon has micropores and, depending on the precursor, may also have mesopores and macropores [44]. Activated carbon presents several advantages as a support for catalysts, such as low synthesis cost, high specific surface area, resistance to acidic and alkaline environments, easy control of textural properties (pore volume and pore size distribution) and thermal stability. On the other hand, activated carbon presents low mechanical strength and, because it is mostly microporous, may impose mass transfer limitations [45]. Other carbon materials, such as carbon nanofibers, have larger pores than microporous activated carbon and consequently are less associated with mass transfer limitations.

Carbon nanofiber (CNF) supports contain organized graphene sheets in their structure and have properties of both activated carbon and graphite. As a consequence, carbon nanofibers have desirable characteristics for use as catalyst support, such as high specific surface area, purity, inertness and, due to their large diameter, carbon nanofibers allow easy diffusion of reactant and product molecules [46]. Carbon nanofibers have been used as catalyst support for different reactions, such as cinnamaldehyde hydrogenation [39, 47] and deoxygenation of triglycerides [48 – 50].

Another promising carbon-based material for use as catalyst support is carbon-covered alumina (CCA). Alumina (aluminum oxide) already is a widely used material as catalyst support because of its mechanical and textural properties; however, it has some drawbacks such as its strong interaction with metals. To overcome this drawback, alumina can be covered with a thin carbon layer. As a consequence, CCA combines the mechanical and textural properties of alumina with the surface chemistry of carbon [51]. The first time CCA was used as catalyst support, CCA was synthesized via cyclohexane or ethene pyrolysis over the γ-Al_2O_3 surface and cobalt sulfide was used as active phase for the thiophene hydrodesulfurization reaction [45]. Although X-ray photoelectron spectroscopy results showed that alumina was not fully covered by carbon, the catalyst supported on CCA was three times more active than the catalyst supported on γ-Al_2O_3 [45], making CCA a promising material in the catalysis field.

Although AC, CNF and CCA are effective supports for various catalysts and reactions, these three carbon-based materials have never been directly compared in the same reaction conditions and with the same active phase, as far as we know. In this paper, we report on an evaluation of the effects of these three different carbon-based supports (activated carbon, carbon nanofibers and carbon-covered alumina) on the structure and deoxygenation performance of tungsten carbide. We characterized the catalysts by means of N_2 sorption, X-ray diffraction, CO

chemisorption as well as temperature-programmed desorption of NH_3 and we used the deoxygenation of stearic acid to evaluate catalyst performance. We analyzed the effect of the support on tungsten carbide activity and selectivity in stearic acid deoxygenation by correlating catalyst performance with structure.

2. Experimental

Synthesis of supports

Carbon nanofibers (CNFs) were synthesized using a reduced 5 wt% Ni/SiO_2 growth catalyst (5 g) and a mixture of hydrogen (102 mL min^{-1}), nitrogen (450 mL min^{-1}) and carbon monoxide (266 mL min^{-1}) at 550 ºC and 3.8 bar for 24 hours, as previously reported [52]. After synthesis, the CNF was refluxed in 400 mL 1M KOH for 1 hour to remove the SiO_2, followed by decanting and washing of the residue with 200 mL 1M KOH. This treatment was repeated three times. After the final reflux, the material was washed with demi water. Subsequently, the solid was treated by refluxing it in 400 mL 65% HNO_3 for 1.5 hours to remove exposed nickel and to add oxygen-containing groups on the surface of the CNF. Finally, the CNF was washed with demi water to a neutral pH of the washing water.

Carbon-covered alumina (CCA) was synthesized as follows. A sucrose solution was added to alumina (BASF) via incipient wetness impregnation (weight sucrose/alumina = 0.624). A calcination step was carried out under He flow at 700 ºC for 2 hours to form two monolayers of carbon covering the alumina. The procedure was repeated to add another carbon monolayer (weight sucrose/alumina = 0.380) over the previous two layers.

Catalyst synthesis

15 wt% W_2C catalysts were synthesized via incipient wetness impregnation of $(NH_4)_6H_2W_{12}O_{40}.xH_2O$ (Sigma-Aldrich) solution on the supports – AC (Activated charcoal Norit®, Sigma-Aldrich), CNF and CCA – and the catalysts were activated under argon flow from 25 ºC to 900 ºC (β = 5 ºC min^{-1}) for 6 hours. Between impregnations, the impregnated materials were dried at 120 ºC for 1 hour in static air.

Catalyst characterization

We explored the crystalline structures of the catalysts with X-ray diffraction (XRD). Supported W_2C catalysts were analyzed in a Rigaku Miniflex instrument with copper radiation (CuK_α). The diffraction angle was varied from 10º to 90º, with steps of 1 degree min^{-1} and counting at 2 s $step^{-1}$.

We used nitrogen physisorption to assess the textural properties of the

catalysts. We recorded nitrogen adsorption/desorption isotherms at liquid nitrogen temperature with the use of a Micromeritics TriStar. Samples were pretreated under a vacuum at 400 ºC for 20 hours (Micromeritics VacPrep 061).

Chemisorbed CO was measured in situ to quantify potential active sites. After synthesis, we flushed the catalyst samples with 50 mL min^{-1} helium at 30 ºC for 30 minutes. CO-pulse chemisorption measurements were performed using a custom-made multipurpose machine by pulsing calibrated volumes of a 20% (v/v) CO/He gas mixture over the catalyst. Mass spectrometry (Pfeiffer Vacuum, model D-35614 Asslar) was used to assess the CO uptake.

Temperature-programmed desorption (TPD) of CO was performed after the CO chemisorption to explore the nature of the active sites. Samples were heated from 30 ºC to 1000 ºC under He flow (100 mL min^{-1} and β = 15 ºC min^{-1}) and the ion signal of m/z = 28 was followed in a mass spectrometer (Pfeiffer Vacuum, model D-35614 Asslar).

Transmission electron microscopy (TEM) was used to analyze particle size and particle size distribution. We mounted the samples on a 200 mesh copper grid covered with a pure carbon film, by dusting them onto the surface of the grid. TEM was performed in a JEOL JEM2100 transmission electron microscope operated at 200 kV, and images (4k x 4k) were taken with a Gatan US4000 camera.

Temperature-programmed desorption (TPD) of NH_3 was performed to explore the acidity of catalysts. The total acid sites of catalysts were quantified by adsorption of a 4% (v/v) NH_3/He gas mixture at room temperature, performed in a custom-made machine, where the ion signals m/z = 17 was followed in a mass spectrometer (Pfeiffer Vacuum, model D-35614 Asslar). After purging the synthesized carbides with He (60 mL min^{-1}), 4% (v/v) NH_3/He (60 mL min^{-1}) gas mixture was added to the system resulting in a negative peak (A1) in the ion signal m/z = 17, corresponding to chemisorbed NH_3 + physisorbed NH_3 + NH_3 in the system dead volume. After the ion signal m/z = 17 returned to the baseline, He was flushed into the system to remove the physisorbed NH_3 from the catalyst surface and the NH_3 present in the system dead volume. 4% (v/v) NH_3/He (60 mL min^{-1}) gas mixture was, thus, flushed again into the system resulting in another negative peak (A2) in the ion signal m/z = 17, representing the physisorbed NH_3 and the NH_3 present in the system dead volume. Therefore, the amount of chemisorbed NH_3 on the catalysts was calculated via the subtraction of the areas A1 – A2.

To explore the efficiency of the carbon cover in CCA, we carried out Diffuse Reflectance Infrared Fourier Transform Spectroscopy (DRIFTS) in an infrared spectrometer (Nicolet NEXUS 470 FT-IR) equipped with diffuse reflectance accessories and heating chamber (MCT-A detector, cooled with liquid nitrogen and

with ZnSe windows). Prior to analysis, samples were heated to 500 ºC for 1 hour under He flow and cooled to room temperature. Samples were then saturated with CO_2, the chamber was cleaned with He to remove non-adsorbed CO_2, and the spectrum was taken in the range of 4000 cm^{-1} to 500 cm^{-1} with a resolution of 4 cm^{-1} and 150 scans.

HDO reaction

Reactions were performed in a 100 mL stainless steel Parr autoclave reactor (4590 Micro Bench Top Reactors). The reactor was filled with 2 g of stearic acid (Sigma-Aldrich, ≥ 95%, FCC, FG), 1 g of tetradecane (internal standard, Sigma-Aldrich, ≥ 99%), 0.25 g of catalyst and 50 mL of dodecane as solvent (Sigma-Aldrich, ReagentPlus®, ≥ 99%). After purging with argon, stirring at 800 rpm was started and the reactor was heated to 350 ºC. At this temperature, the total pressure was 10 bar. Subsequently, 30 bar H_2 was added to the system, reaching a final pressure of around 40 bar. Samples of 1 mL were taken during the 6-hour reaction after 0, 20, 40, 60, 120, 180, 240, 300 and 360 minutes.

Gas chromatography (GC) was used to analyze the reaction mixture (Shimadzu 2014, equipped with CP-FFAP column and photoionization detector). We used the following column temperature program: 50 ºC for 1 minute, heating to 170 ºC (β=7 ºC min^{-1}), dwell time 1 minute, ramp to 240 ºC (β=4 ºC min^{-1}), dwell time 15 minutes. Prior to GC, we diluted the samples in CH_3Cl:MeOH (2:1 v/v). Trimethylsulphonium hydroxide (Sigma-Aldrich, ~ 0.25 M in methanol, for GC derivatization) was added to methylate free acids. The injected volume was 1μL for all analysis.

3. Results and discussion

Table 1 displays textural properties of the pure supports (activated carbon – AC, carbon- covered alumina – CCA and carbon nanofiber – CNFs) and of the three supported W_2C catalysts as inferred from nitrogen physisorption. Figure A1 in the Appendix A shows nitrogen adsorption/desorption isotherms for the pure supports and the supported W_2C catalysts.

Table 1. Textural properties of AC, CCA, CNF supports and supported W_2C carbide catalysts. SBET = specific Brunauer-Emmett-Teller (BET) surface area.

Sample	SBET ($m^2\ g^{-1}$)	Micropore area ($m^2\ g^{-1}$)	Micropore volume ($m^3\ g^{-1}$) x 10^{-9}	Total pore volume ($m^3\ g^{-1}$) x 10^{-9}	Average pore size (nm)
AC	823	394	200	500	8.7
CCA	193	44	20	370	9.3
CNF	171	20	9	450	15.1
W_2C/AC	696	335	170	430	8.3
W_2C/CCA	161	39	20	310	9.4
W_2C/CNF	124	7	3	370	15.1

AC presented a higher specific surface area (823 $m^2\ g^{-1}$) compared with CCA (193 $m^2\ g^{-1}$) and CNF (180 $m^2\ g^{-1}$). AC also showed a higher micropore area and volume (394 $m^2\ g^{-1}$ and 200 x 10^{-9} $m^3\ g^{-1}$) than the other supports (CCA: 44 $m^2\ g^{-1}$ and 20 x 10^{-9} $m^3\ g^{-1}$ and CNF: 20 $m^2\ g^{-1}$ and 9 x 10^{-9} $m^3\ g^{-1}$, respectively). On the other hand, CNF had a larger pore size than AC and CCA (CNF: 13.6 nm, AC: 8.7 nm and CCA: 9.3 nm). These results indicate that the supports had significant differences in textural properties, especially regarding surface area and pore size.

The specific Brunauer-Emmett-Teller (BET) surface area of W_2C/AC and W_2C/CCA was around 15% lower than for the pure supports. Since these catalysts were synthesized with a 15 wt% loading, a decrease of up to 15% of the surface area can be attributed to the carbide addition to the support. Thus, W_2C/AC and W_2C/CCA presented similar textural surface areas as the respective pure supports.

On the other hand, the specific surface area, micropore area and micropore volume values of W_2C/CNF (124 $m^2\ g^{-1}$, 7 $m^2\ g^{-1}$ and 3 x 10^{-9} $m^3\ g^{-1}$) are smaller than for pure CNF (171 $m^2\ g^{-1}$, 20 $m^2\ g^{-1}$ and 9 x 10^{-9} $m^3\ g^{-1}$), even when considering that 15% of active phase had been added to the support. These results suggest that some micropores of the CNF were blocked during W_2C/CNF synthesis. However, since total pore volume and pore average size of W_2C/CNF (370 x 10^{-9} $m^3\ g^{-1}$ and 15.1 nm) were similar to those of the pure CNF (450 x 10^{-9} $m^3\ g^{-1}$ and 15.1 nm), taking a margin of 15% into account, we conclude that although micropores might be blocked during W_2C/CNF synthesis, larger pores in the support were still present in the catalyst structure.

To investigate the crystalline structure of the catalysts, we used X-ray diffraction (XRD). Figure 1(A – C) presents the diffractograms of W_2C supported on

AC, CCA and CNF, with the respective precursors and pure supports.

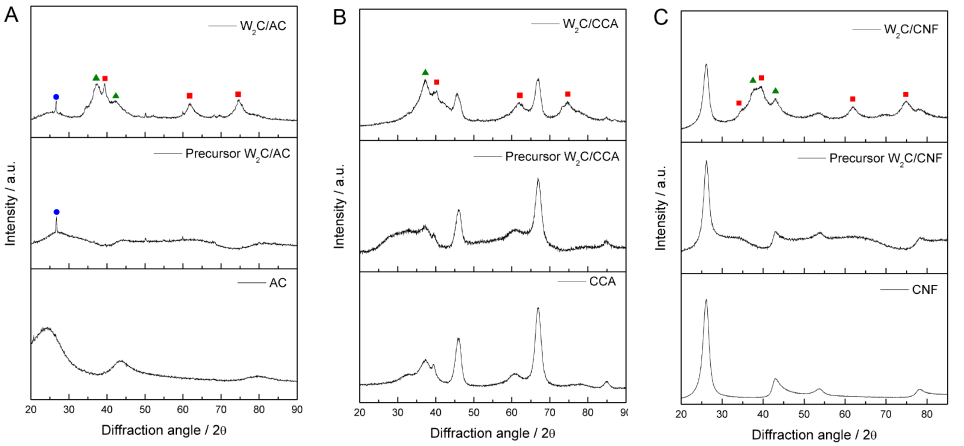

Figure 1. XRD diffractograms of pure support, supported tungsten oxide precursor and tungsten carbide supported by (A) AC, (B) CCA and (C) CNF, ● C ▲ $W_2(C,O)$ ■ W_2C.

The diffractograms of W_2C supported on AC, CNF and CCA show peaks at 2θ values of 36.8º and 42.7º, which corresponds to the oxy-carbide $W_2(C,O)$ phase (PDF#22-0959), indicated by the green triangles, as well as peaks at a 2θ of 39.6º, 61.7º and 72.7º, which corresponds to the W_2C phase (PDF#20-1315), indicated by the red squares. Since the catalysts were passivated with 0.5 (v/v) % O_2/N_2 (50 mL min^{-1}) at 25 ºC for 24 hours before XRD analysis to avoid their complete oxidation when exposed to air, we attribute the presence of the oxy-carbide phase to partial oxidation of catalyst during the passivation treatment.

To analyze the particle size of the carbide, high-resolution transmission electron microscopy (HR-TEM) was performed. Figure 2 displays representative HR-TEM images of tungsten carbide supported on AC, CCA and CNF. Black spots represent the active phase carbide (indicated with the red arrows) and the dark grey area is the support.

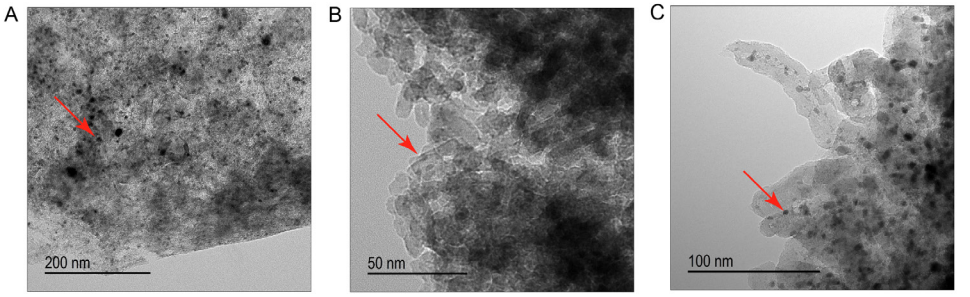

Figure 2. HR-TEM images of A) W_2C/AC, B) W_2C/CCA and C) W_2C/CNF.

We estimated the average particle size based on 250 to 400 particles for each catalyst. Table 2 shows the average particle sizes and Figure 3 displays the particle size distributions.

Table 2. Average particle size of supported W_2C catalysts.

Catalyst	Average particle size (nm)	Standard deviation (nm)
W_2C/AC	6	3
W_2C/CCA	2	1.5
W_2C/CNF	3	2

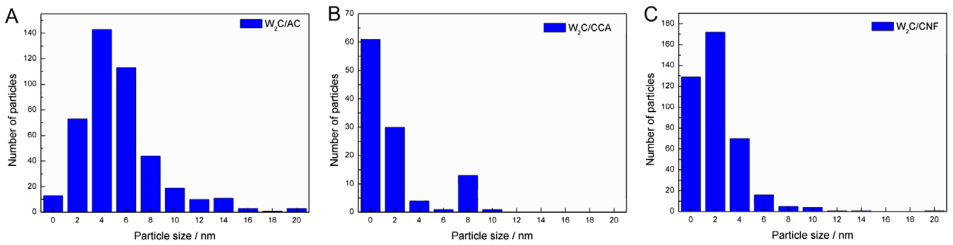

Figure 3. Particle size distribution for tungsten carbide supported on AC, CCA and CNF.

The average particle size of W_2C/AC, W_2C/CCA and W_2C/CNF was 6, 2 and 3 nm, respectively. Although the W_2C/AC catalyst presented a higher particle size average than W_2C/CCA and W_2C/CNF, Figure 3 shows that the largest particles of W_2C/CCA and W_2C/CNF catalysts have a diameter of 10 nm, while the diameter of the largest particles of W_2C/AC is 20 nm. The presence of a few larger particles (> 10 nm) in the W_2C/AC catalyst accounts for its higher average particle size. Since large particles present a high volume-to-surface ratio, those particles likely did not make a significant contribution to the overall weight-based activity. Furthermore, most particles of the three catalysts had an average diameter of less than 6 nm. We therefore concluded that differences in average particle size of the catalysts were not a significant factor.

To enable a fair comparison between the catalytic performance of W_2C/AC, W_2C/CNF and W_2C/CCA, we used CO chemisorption to quantify potential active sites. Table 3 displays the CO chemisorption results for the three catalysts. CO uptake for tungsten carbide catalysts follows the order W_2C/CCA (80 μmol g^{-1}) > W_2C/AC (60 μmol g^{-1}) > W_2C/CNF (34 μmol g^{-1}). The CO uptake value is related to the number of accessible sites that can interact with CO molecules, which means that the catalyst

that presents the highest CO uptake value may have more accessible sites available for reaction according to Lee *et al.* [53].

CO uptake for the AC, CCA and CNF supports was 0, 0 and 1 μmol g^{-1}, respectively. This result indicates that the CO uptake values of supported catalysts are exclusively related to the active phase.

Table 3. CO uptake for AC, CCA, CNF supports and for supported tungsten carbides.

Support	CO uptake (μmol g^{-1})	Catalyst	CO uptake (μmol g^{-1})
AC	0	W_2C/AC	61
CCA	0	W_2C/CCA	80
CNF	1	W_2C/CNF	34

Although CO chemisorption provides information about the density of potential active sites, it does not inform about the nature of these sites. We therefore performed CO TPD analysis, which enabled us to compare the nature of the active sites through the CO-binding strength. Active sites of a different nature bind CO with a different strength, which is indicated by the temperature of the peaks in the CO TPD profile. Stronger bonds result in higher temperatures of CO desorption. Figure 4 displays the CO TPD results of the supported tungsten carbide catalysts, each showing three peaks at 90, 150 and 200 ºC, indicated by the red squares in the figure. These results suggest that although the catalysts are supported by different materials (AC, CCA and CNF), the nature of their active sites is the same.

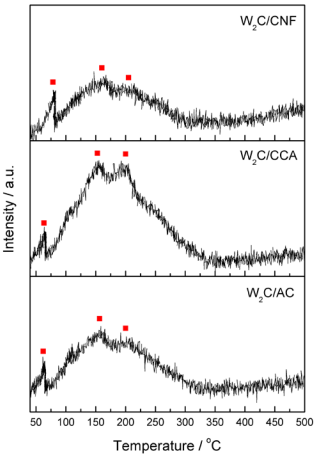

Figure 4. Temperature-programmed desorption of CO from tungsten carbide supported on AC, CCA and CNF.

NH_3 TPD was performed to analyze the acidity of the catalysts. Table 4 displays the density of the catalysts' acidic sites. W_2C/CCA had the highest density of acidic sites (217 μmol g^{-1}) compared with W_2C/AC and W_2C/CNF (44 and 46 μmol g^{-1}, respectively).

Table 4. Acidity of the catalyst as measured via NH_3 temperature-programmed desorption.

Catalyst	**Acidic sites (μmol g^{-1})**
W_2C/AC	44
W_2C/CCA	217
W_2C/CNF	46

The higher acidity of tungsten carbide supported on carbon-covered alumina may be attributed to the acidity of alumina. Although the alumina was completely covered by carbon, as shown by CO_2 Diffuse Reflectance Infrared Fourier Transform Spectroscopy (DRIFTS) analysis (Figure A2), the higher amount of desorbed NH_3 (Table 4) suggests that the porosity of carbon enables the alumina to be available for interaction with external molecules, such as ammonia during NH_3 TPD.

Stearic acid hydrodeoxygenation was performed over supported tungsten carbide catalysts at 350 ºC and 30 bar H_2. Figure 5 displays the stearic acid conversion over time.

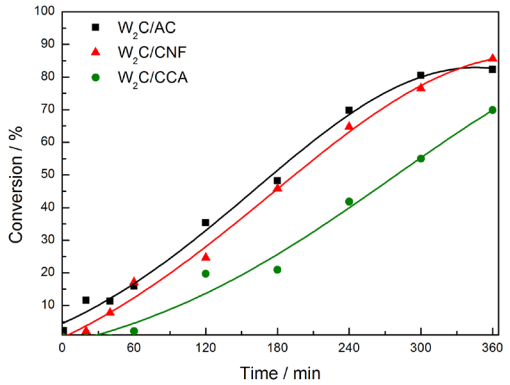

Figure 5. Stearic acid conversion over tungsten carbide supported on AC, CNF and CCA (250 mg catalyst, 2 g stearic acid, 50 mL solvent, 30 bar H_2, 350 ºC).

W_2C supported on CCA presented the lowest stearic acid conversion relative to W_2C supported on AC and CNF (although W_2C/CCA showed the highest CO uptake

value). We propose that this result can be explained by the textural properties. The combination of a lower surface area (161 m^2 g^{-1}) with a smaller pore size (9.4 nm) of the CCA-supported catalyst limits the access of stearic acid to active sites, resulting in a lower stearic acid conversion.

The conversion over the W_2C/AC and W_2C/CNF catalysts was similar and reached the maximum value of 85% at 360 min. W_2C/AC presented a higher CO uptake value (61 μmol g^{-1}), higher specific surface area (696 m^2 g^{-1}) and smaller pore size (8.3 nm) than W_2C/CNF (34 μmol g^{-1}, 124 m^2 g^{-1} and 15.1 nm, respectively). While the higher specific surface area favors the interaction of stearic acid molecules with the catalyst surface, the smaller pore size may limit it. Thus, a balance between pore size and surface area may explain that the stearic acid conversion over the W_2C/AC and W_2C/CNF catalysts was similar. Note that the reaction is not limited by mass transfer limitations (see Figure A3).

To investigate the intrinsic activity of the catalysts, the turnover frequency (TOF) was calculated based on initial reaction rate. Table 5 lists the results. All three catalysts presented a similar TOF for stearic acid HDO reaction at 350 ºC and 30 bar H_2, which indicates that the catalysts have the same intrinsic activity. This result is in accordance with the CO TPD profiles (Figure 5), which shows that the nature of the active sites on the three catalysts was the same.

Table 5. Turnover frequency (TOF) of W_2C supported on AC, CNF and CCA.

Catalyst	**TOF (s^{-1})**
W_2C/AC	2
W_2C/CNF	3
W_2C/CCA	1

Figure 6 displays the product distribution for supported tungsten carbide catalysts for different conversion percentages, to explore the influence of the supports' pore size and acidity on the product distribution in stearic acid HDO.

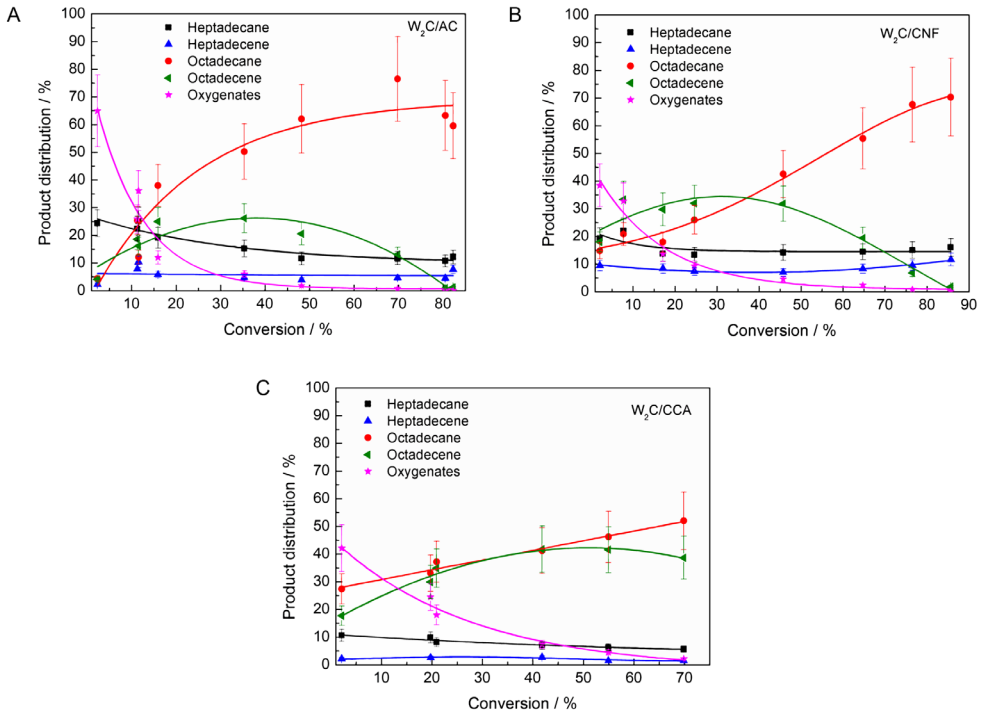

Figure 6. Product distribution for tungsten carbide on A) AC, B) CNF and C) CCA during stearic acid HDO (250 mg catalyst, 2 g stearic acid, 50 mL solvent, 30 bar H_2, 350 ºC).

Figure 6 shows a number of differences between the performance of the catalysts, such as the following, which we will discuss subsequently:

- The selectivity towards oxygenates was higher over W_2C/AC compared with W_2C/CNF and W_2C/CCA at low conversion rates (< 5%).
- The ratio octadecene (C18 unsat) to octadecane (C18 sat) was higher over W_2C/CCA than over W_2C/CNF and W_2C/AC. Only for W_2C/CNF at lower conversion rates (< 30%), the selectivity towards octadecene surpassed that of octadecane.

The selectivity towards oxygenates was higher over W_2C/AC than over W_2C/CNF and W_2C/CCA at low conversion (< 5%).

Oxygenates (octadecanal and octadecanol) were the primary products over all three catalysts, which matches observations by other researchers [54]. However, at conversion below 5%, oxygenates represented 70% (mol) of all products over the W_2C/AC catalyst while they represented only 40% (mol) over the W_2C/CNF and W_2C/CCA catalysts.

According to Kim *et al.* [55], a carbon-based support with a large pore

size facilitates the transport of reactants during hydrodeoxygenation. In addition, Schaidle *et al.* [54] concluded via experimental and theoretical calculations that acid catalysts favor dehydration of oxygenates in the hydrodeoxygenation reaction. Figure 7 summarizes the effect of pore size (A) and acidity (B) on the oxygenates selectivity at 3% conversion of stearic acid HDO.

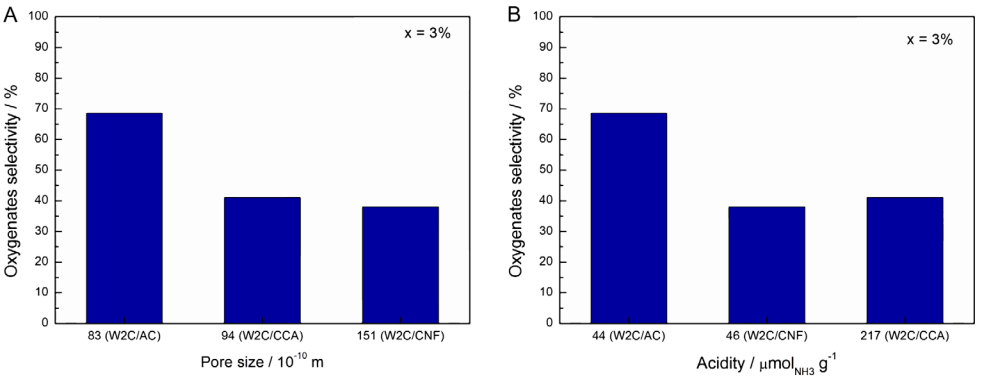

Figure 7. Effect of catalyst pore size (A) and acidity (B) on oxygenates selectivity at 3% conversion in stearic acid HDO (250 mg catalyst, 2 g stearic acid, 50 mL solvent, 30 bar H_2, 350 ºC).

Clearly, neither the pore size nor the acidity related directly to the selectivity. Therefore, we believe that the combination of acidity and porosity determined the performance of the catalysts. However, the exact contribution of each parameter currently remains an enigma.

The ratio C18-unsat:C18-sat was higher over W_2C/CCA than over W_2C/CNF and W_2C/AC. Only for W_2C/CNF at lower conversion rates (< 30%), the selectivity towards C18-unsat surpassed that of C18-sat.

At conversions below 30%, W_2C/CNF produced compounds resulting in a C18-unsat:C18-sat rate greater than 1 while W_2C/AC and W_2C/CCA produced compounds resulting in a C18-unsat:C18-sat rate of less than 1. Apparently, the highest amounts of the unsaturated octadecene were initially formed over the support with the greatest mesopore volume (CNF), which indicates that the alkene was released more easily from CNF than from AC and CCA.

Figure 8 summarizes the influence of pore size on the C18-unsat:C18-sat selectivity for 25% conversion.

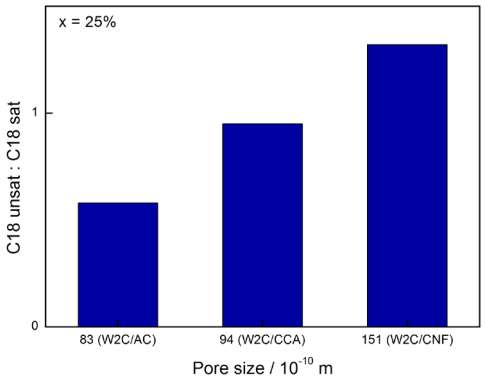

Figure 8. Effect of catalyst pore size on the C18-unsat:C18-sat ration at 25% conversion on stearic acid HDO (250 mg catalyst, 2 g stearic acid, 50 mL solvent, 30 bar H_2, 350 ºC).

At higher conversions, *i.e.* above 50%, the C18-unsat:C18-sat ratio over the W_2C/CCA catalyst was higher than over the W_2C/AC and W_2C/CNF catalysts. According to Schaidle *et al.* [54], the relative extents of hydrogenation and dehydration of oxygenates (aldehyde and alcohol) is related to the ratio between metallic and acidic sites on the carbide surface. Since C18-unsat is produced via dehydration of oxygenates and C18-sat is produced via hydrogenation of C18-unsat, it is expected that catalysts with a higher ratio of acid to metallic sites favor C18-unsat production and catalysts with a lower acid:metallic site ratio favor C18-sat production.

The combination of CO chemisorption (metallic sites) and NH_3 TPD (acid sites) analysis indicates that the W_2C/CCA catalyst had a higher ratio of acid:metallic sites (2.7) than the W_2C/AC (0.7) and W_2C/CNF (1.3) catalysts. This explains why the W_2C/CCA catalyst had the highest C18-unsat:C18-sat ratio (0.87) relative to W_2C/AC (0.3) and W_2C/CNF (0.4) for conversions above 50%.

Figure 9 summarizes the effect of acidity on the C18-unsat:C18-sat rate at 60% conversion of stearic acid HDO.

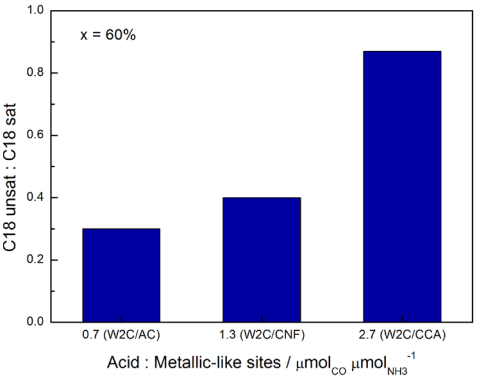

Figure 9. Effect of the acid/metallic site ratio on the C18-unsat:C18-sat ratio at 60% conversion during stearic acid HDO (250 mg catalyst, 2 g stearic acid, 50 mL solvent, 30 bar H_2, 350 ºC).

4. Conclusions

In our study, activated carbon, carbon nanofiber and carbon-covered alumina supports did not appear to influence the nature of the active sites of tungsten carbide catalysts. As a consequence, W_2C/AC, W_2C/CCA and W_2C/CNF presented the same intrinsic activity (TOF) for stearic acid HDO. However, differences in support acidity and pore size did appear to influence stearic acid product distribution. While the larger pore size of W_2C/CNF favored the conversion of oxygenates into hydrocarbons and the production of C18-unsat at low conversions (< 30%), the higher acidity of W_2C/CCA favored the conversion of oxygenates at low conversions (< 30%) and the higher production of C18-unsat at high conversions (> 50%). For a complete understanding of catalyst pore size and acidity effects on the product distribution of stearic acid HDO, further studies might be performed with catalysts with similar acidity but different pore size and catalysts with similar pore size but different acidity.

References

[1] Ragauskas, A. J.; Williams, C. K.; Davison, B. H.; Britovsek, G.; Cairney, J.; Eckert, C. A.; Frederick Jr., W. J.; Hallet, J. P.; Leak, D. J.; Liotta, C. L.; Mielenz, J. R.; Murphy, R.; Templer, R.; Tschaplinski, T. The path forward for biofuels and biomaterials. *Science* **2006**, 311 (5760), 484 – 489.

[2] Ziejewski, M.; Kaufman, K. R.; Schwab, A.W.; Pryde, E. H. Diesel engine evaluation of a nonionic sunflower oil-aqueous ethanol microemulsion. *JAOCS* **1984**, 61 (10), 1620 – 1626.

[3] Goering, C. E.; Fry, B. Engine durability screening test of a diesel oil/soy oil/alcohol microemulsion fuel. *JAOCS* **1984**, 61 (10), 1627 – 1632.

[4] Schwab, A. W.; Bagby, M. O.; Freedman, B. Preparation and properties of diesel fuels from vegetable oils. *Fuel* **1987**, 66 (10), 1372 – 1378.

[5] Pryde, E. H. Vegetable oil as fuel alternatives – symposium overview. *JAOCS* **1984**, 61 (10), 1609 – 1610.

[6] Alencar, J. W.; Alves, P. B.; Craveiro, A. A. Pyrolysis of tropical vegetable oils. *J. Agric. Food Chem.* **1983**, 31 (6), 1268 – 1270.

[7] Schwab, A. W.; Dykstra, G. J.; Selke, E.; Sorenson, S. C.; Pryde, E. H. Diesel fuel from thermal decomposition of soybean oil. *JAOCS* **1988**, 65 (11), 1781 – 1786.

[8] Vonghia, E.; Boocock, D. G. B.; Konar, S. K.; Leung, A. Pathways for the deoxygenation of triglycerides to aliphatic hydrocarbons over activated alumina. *Energy Fuels* **1995**, 9 (6), 1090 – 1096.

[9] Quirino, R. L. Estudo do Efeito da Presença de Alumina Dopada com TiO_2 e ZrO_2 no Craqueamento do Óleo de Soja. Master Dissertation, IQ/UnB, Brasília, DF, Brasil, 2006.

[10] Dupain, X.; Costa, D. J.; Schaverien, C. J.; Makkee, M.; Moulijn, J. A. Cracking of a rapeseed vegetable oil under realistic FCC conditions. *Appl. Catal. B: Environm.* **2007**, 72 (1 – 2), 44 – 61.

[11] Fukuda, H.; Kondo, A.; Noda, H. Biodiesel fuel production by transesterification of oils. *J. Biosci. Bioeng.* **2001**, 92 (5), 405 – 416.

[12] Srivastava, A.; Prasad, R. Triglycerides-based diesel fuels. *Renew. Sust. Energ. Rev.* **2000**, 4 (2), 111 – 133.

[13] Lotero E.; Liu, Y.; Lopez, D. E.; Suwannakarn, K.; Bruce, D.A.; Goodwin Jr., J. G. Synthesis of biodiesel via acid catalysis. *Ind. Eng. Chem. Res.* **2005**, 44 (14), 5353 – 5363.

[14] Leung, D. Y. C.; Wu, X.; Leung, M. K. H. A review on biodiesel production using catalyzed transesterification. *Appl. Energy* **2010**, 87 (4), 1083 – 1095.

[15] Demirbas, A. Progress and recent trends in biodiesel fuels. *Energy Convers. Manag.* **2009**, 50 (1), 14 – 34.

[16] Craig, W. K.; Soveran, D. W. Production of Hydrocarbons with a Relatively High Cetane Rating. US Patent No. 4992605, 1991.

[17] Huber, G. W.; O'Connor, P.; Corma A. Processing biomass in conventional oil refineries: Production of high quality diesel by hydrotreating vegetable oils in heavy vacuum oil mixtures. *Appl. Catal. A: Gen.* **2007**, 329 (1), 120 – 129.

[18] Donnis, B.; Egeberg, R. G.; Blom, P.; Knudsen, K. G. Hydroprocessing of bio-oils and oxygenates to hydrocarbons. Understanding the reaction routes. *Top. Catal.* **2009**, 52 (3), 229 – 240.

[19] Kubicka, D.; Kaluza, L. Deoxygenation of vegetable oils over sulfide Ni, Mo and NiMo catalysts. *Appl. Catal. A: Gen.* **2010**, 372 (2), 199 – 208.

[20] Sousa, L. A.; Zotin, J. L.; Teixeira da Silva, V. Hydrotreatment of sunflower oil using supported molybdenum carbide. *Appl. Catal. A: Gen.* **2012**, 449 (27), 105 – 111.

[21] Gao, D.; Schweitzer, C.; Hwang, H. T.; Varma. A. Conversion of guaiacol on noble metal catalysts: Reaction performance and deactivation studies. *Ind. Eng. Chem. Res.* **2014**, 53 (49), 18658 – 18667.
[22] Simakova, I.; Simakova, O.; Mäki-Arvela, P.; Simakov, A.; Estrada, M.; Murzin, D. Yu. Deoxygenation of palmitic and stearic acid over supported Pd catalysts: Effect of metal dispersion. *Appli. Catal. A: Gen.* **2009**, 355 (1 – 2), 100 – 108.
[23] Zeng, Y.; Wang, Z.; Lin, W.; Song, W. In situ hydrodeoxygenation of phenol with liquid hydrogen donor over three supported noble-metal catalysts. *Chem. Eng. J.*, **2017**, 320 (15), 55 – 62.
[24] Robinson, A.; Ferguson, G. A.; Gallagher, J. R.; Cheah, S.; Beckham, G. T.; Schaidle, J. A.; Hensley, J. E.; Medlin, J. W. Enhanced hydrodeoxygenation of m-cresol over bimetallic Pt-Mo catalysts through an oxophilic metal-induced tautomerization pathway. *ACS Catal.* **2016**, 6 (7), 4356 – 4368.
[25] Mu, W.; Ben, H.; Du, X.; Zhang, X.; Hu, F.; Liu, W.; Ragauskas, A. J. Noble metal catalyzed aqueous phase hydrogenation and hydrodeoxygenation of lignin-derived pyrolysis oil and related model compounds. *Biotech. Technol.* **2014**, 173, 6 – 10.
[26] Newman, C.; Zhou, X.; Goundie, B.; Ghampson, I. T.; Pollock, R. A.; Ross, Z.; Wheeler, M. C.; Meulenberg, R. W.; Austin, R. N.; Frederick, B. G. Effects of support identity and metal dispersion in supported ruthenium hydrodeoxygenation catalysts. *Appl. Catal. A: Gen.* **2014**, 477 (5), 64 – 74.
[27] Oyama, S. T. Preparation and catalytic properties of transition metal carbides and nitrides. *Catal. Today* **1992**, 15 (2), 179 – 200.
[28] Levy, R. B.; Boudart, M. Platinum-like behavior of tungsten carbide in surface catalysis. *Science* **1973**, 181 (4099), 547–549.
[29] Claridge, J. B.; York, A. P. E.; Brungs, A. J.; -Alvarez, C. M.; Sloan, J.; Tsang, S. C.; Green, M. L. H. New catalysts for the conversion of methane to synthesis gas: molybdenum and tungsten carbide. *J. Catal.* **1998**, 180 (1), 85 – 100.
[30] Alexander, A. -M.; Hargreaves, J. S. J. Alternative catalytic materials: carbides, nitrides, phosphides and amorphous boron alloys. *Chem. Soc. Rev.* **2010**, 39 (11), 4388 – 4401.
[31] Li, C.; Zheng, M.; Wang, A.; Zhang, T. One-pot catalytic hydrocracking of raw woody biomass into chemicals over supported carbide catalysts: simultaneous conversion of cellulose, hemicellulose and lignin. *Energ. Environ. Sci.* **2012**, 5 (4), 6383 – 6390.
[32] Hollak, S. A. W.; Gosselink, R. W.; van Es, D. S.; Bitter, J. H. Comparison of tungsten and molybdenum carbide catalysts for the hydrodeoxygenation of oleic acid. *ACS Catal.* **2013**, 3 (12), 2837 – 2844.
[33] Qin, Y.; He, L.; Duan, J.; Chen, P.; Lou, H.; Zheng, X.; Hong, H. Carbon-supported molybdenum-based catalysts for the hydrodeoxygenation of maize oil. *ChemCatChem* **2014**, 6 (10), 2698 – 2705.
[34] Sullivan, M. M.; Bhan, A. Acetone hydrodeoxygenation over bifunctional metallic-acidic molybdenum carbide catalysts. *ACS Catal.* **2016**, 6 (2), 1145 – 1152.
[35] Ren, H.; Yu, W.; Salciccioli, M.; Chen, Y.; Huang, Y.; Xiong, K.; Vlachos, D. G.; Chen, J. G. Selective hydrodeoxygenation of biomass-derived oxygenates to unsaturated hydrocarbons using molybdenum carbide catalysts. *ChemSusChem* **2013**, 6 (5), 798 – 801.
[36] Mojet, B. L.; Miller, J. T.; Ramaker, D. E.; Koningsberger, D. C. A new model describing the metal-support interaction in noble metal catalysts. *J. Catal.* **1999**, 186 (2), 373 – 386.
[37] Ramaker, D. E.; de Graaf, J.; van Veen, J. A. R.; Koningsberger, D. C. Nature of the metal-support interaction in supported Pt catalysts: Shift in Pt valence orbital energy and

charge rearrangement. *J. Catal.* **2001**, 203 (1), 7 – 17.
[38] Koningsberger, D. C.; Oudenhuijzen, M. K.; de Graaf, J.; van Bokhoven, J. A.; Ramaker, D. E. In situ X-ray absorption spectroscopy as a unique tool for obtaining information on hydrogen binding sites and electronic structure of supported Pt catalysts: towards an understanding of the compensation relation in alkane hydrogenolysis. *J. Catal.* **2003**, 216 (1 – 2), 178 – 191.
[39] Toebes, M. L.; Zhang, Y.; Hájek, J.; Nijhuis, T. A.; Bitter, J. H.; van Dillen, A. J.; Murzin, D. Y.; Koningsberger, D. C.; de Jong, K. P. Support effects in the hydrogenation of cinnamaldehyde over carbon nanofiber-supported platinum catalysts: characterization and catalysis. *J. Catal.* **2004**, 226 (1), 215 – 225.
[40] Kubicka, D.; Horácek, J.; Setnicka, M.; Bulánek, R.; Zukal, A.; Kubicková, I. Effect of support-active phase interactions on the catalyst activity and selectivity in deoxygenation of triglycerides. *Appl. Catal. B: Environm.* **2014**, 145, 101 – 107.
[41] Arend, M.; Nonnen, T.; Hoelderich, W. F.; Fischer, J.; Groos, J. Catalytic deoxygenation of oleic acid in continuous gas flow for the production of diesel-like hydrocarbons. *Appl. Catal. A: Gen.* **2011**, 399 (1 – 2), 198 – 204.
[42] Ford, J. P.; Immer, J. G.; Lamb, H. H. Palladium catalysts for fatty acid deoxygenation: Influence of the support and fatty acid chain length on decarboxylation kinetics. *Top. Catal.* **2012**, 55 (3 – 4), 175 – 184.
[43] Sari, E.; Kim, M.; Salley, S. O.; Ng, K. Y. S. A highly active nanocomposite silica-carbon supported palladium catalyst for decarboxylation of free fatty acids for green diesel production: Correlation of activity and catalyst properties. *Appl. Catal. A: Gen.* **2013**, 467, 261 – 269.
[44] Boehm, H. P. Some aspects of the surface chemistry of carbon blacks and other carbons. *Carbon* **1994**, 32 (5), 759 – 769.
[45] Vissers, J. P. R.; Mercx, F. P. M.; Bouwens, S. M. A. M.; de Beer, V. H. J.; Prins, R. Carbon-covered alumina as a support for sulfide catalysts. *J. Catal.* **1988**, 114 (2), 291 – 302.
[46] Bitter, J. H. Nanostructured carbons in catalysis a Janus material – industrial applicability and fundamental insights. *J. Mater. Chem.* **2010**, 20 (35), 7312 – 7321.
[47] Plomp, A. J.; Vuori, H.; Krausse, A. O. I.; de Jong, K. P.; Bitter, J. H. Particle size effects for carbon nanofiber supported platinum and ruthenium catalysts for the selective hydrogenation of cinnamaldehyde. *Appl. Catal. A: Gen.* **2008**, 351 (1), 9 – 15.
[48] Gosselink, R. W.; Stellwagen, D. R.; Bitter, J. H. Tungsten-based catalysts for selective deoxygenation. *Angew. Chem. Int. Ed.* **2013**, 52 (19), 5089 – 5092.
[49] Stellwagen, D. R.; Bitter, J. H. Structure-performance relations of molybdenum and tungsten carbide catalysts for deoxygenation. *Green Chem. 2015*, 17 (1), 582 – 593.
[50] Gosselink, R. W.; Xia, W.; Muhler, M.; de Jong, K. P.; Bitter, J. H. Enhancing the activity of Pd on carbon nanofibers for deoxygenation of amphiphilic fatty acid molecules through support polarity. *ACS Catal.* **2013**, 3 (10), 2397 – 2402.
[51] Lin, L.; Lin, W.; Zhu, Y. X.; Zhao, B. Y.; Xie, Y. C.; Jia, G. Q.; Li, C. Uniformly carbon-covered alumina and its surface characteristics. *Langmuir* **2005**, 21 (11), 5040 – 5046.
[52] Toebes, M. L.; van der Lee, M. K.; Tang, L. M.; Huis in't Veld, M. H.; Bitter, J. H.; van Dillen, J.; de Jong, K. P. Preparation of carbon nanofiber supported platinum and ruthenium catalysts: comparison of ion adsorption and homogeneous deposition precipitation. *J. Phys. Chem. B* **2004**, 108 (31), 11611 – 11619.
[53] Lee, J. S.; Lee, K. H.; Lee, J. Y. Selective chemisorption of carbon monoxide and

hydrogen over supported molybdenum carbide catalysts. *J. Phys. Chem.* **1992**, 96 (1), 362 – 366.
[54] Schaidle, J. A.; Blackburn, J.; Farberow, C. A.; Nash, C.; Steirer, K. X.; Clark, J.; Robichaud, D. J.; Ruddy, D. A. Experimental and computational investigation of acetic acid deoxygenation over oxophilic molybdenum carbide: surface chemistry and active site identity. *ACS Catal.* **2016**, 6 (2), 1181 – 1197.
[55] Kim, S. K.; Yoon, D.; Lee, S-C.; Kim, J. Mo_2C/graphene nanocomposite as a hydrodeoxygenation catalyst for the production of diesel range hydrocarbons. *ACS Catal.* **2015**, 5 (6), 3292 – 3303.

Chapter 4

On the pathways of hydrodeoxygenation over supported Mo-carbide and Ni-phosphide

Co-authors of this chapter are R. R. de Oliveira Jr, V. Teixeira da Silva and H. Bitter (manuscript in preparation).

Abstract

For the first time a direct comparison of the performance of Mo_2C/CNF and Ni_2P/CNF for the deoxygenation of stearic acid at identical conditions (350 °C and 30 bar H_2) was performed. Ni_2P/CNF (TOF 179 s^{-1}) is intrinsically more active than Mo_2C/CNF (TOF 1 s^{-1}). In addition, the use of Ni_2P/CNF resulted in heptadecane as the main final product while the use of Mo_2C/CNF resulted in octadecane as the predominant product. Those findings suggest that Ni_2P/CNF favors either the decarbonylation/decarboxylation (DCO) or the hydrogenation followed by decarbonylation (HDCO) pathway while Mo_2C/CNF favors the hydrodeoxygenation (HDO) pathway. DFT studies indicated that the activation energy for the (O)C-OH bond cleavage over Ni_2P and butyric acid is 12.9 kcal mol^{-1} while the activation energy for C-COOH bond cleavage is 39.7 kcal mol^{-1}. This indicates that the HDO or HDCO pathway is more favored over Ni_2P/CNF than the DCO pathway. Since heptadecane was the main product over Ni_2P/CNF, it was concluded that HDCO is the predominant pathway over Ni_2P/CNF during stearic acid deoxygenation.

1. Introduction

When using biomass as renewable feedstock and when aiming for drop-in molecules from that biomass, deoxygenation is an essential reaction. Here we studied the deoxygenation of stearic acid as model reaction for the deoxygenation of vegetable oil based triglycerides. The products from that deoxygenation are relevant as chemical building blocks or fuels [1]. Stearic acid deoxygenation mainly occurs via three pathways: i. Decarbonylation – removal of the oxygen as CO and H_2O and producing an unsaturated hydrocarbon; ii. Decarboxylation – removal of oxygen as CO_2 with the production of a saturated hydrocarbon; and iii. Hydrodeoxygenation – removal of oxygen as water via the hydrogenation of the carboxylic group with the formation of a saturated hydrocarbon [1]. The predominant reaction pathway depends on both reaction conditions and catalyst used.

Conventional hydrotreating catalysts, such as alumina supported NiMo and CoMo sulfides hold a great potential as deoxygenation catalysts [2 – 6]. Although they are active and promote all reaction pathways decarbonylation/decarboxylation (DCO) and hydrodeoxygenation (HDO) [7], they deactivate due to sulfur loss, as H_2S, from the active sites. The catalytic activity can be maintained by the addition of small amounts of sulfur-containing compounds to the feed. However, the presence of H_2S in the reaction mixture promotes the DCO pathway at the expense of the HDO pathway. Moreover, the presence of sulfur in the product stream is undesired [8].

Noble metal based catalysts are also active for hydrogenation [9 – 12] and deoxygenation reactions [13 – 17]. However, their limited availability and high price are incentives to look for alternative catalysts. Moreover, the similarities in electronic properties between noble metals, Mo-carbides and Ni-phosphides [18] and the higher availability of the latter two make Mo-carbides and Ni-phosphides potential catalysts for deoxygenation reactions [19 – 25].

Although Mo-carbides and Ni-phosphides share similar electronic properties, they have structural differences. In Mo-carbides, the Mo atoms are ordered in a face centered cubic (fcc) form, a hexagonal closed packed (hcp) form or in simple hexagonal (hex) form [19]. In the metal phosphides, the metal atoms form a triangular prism around the large phosphorus atoms [20].

The differences in crystalline structures between Mo-carbides and Ni-phosphides might be responsible for the differences in their catalytic performance and it has been claimed that metal (W, Mo) carbides favor hydrodeoxygenation pathway in several deoxygenation reactions like in the stearic acid deoxygenation at 350 °C and 30 bar H_2 [26] and in the acetone deoxygenation at 96 °C and 0.54 bar H_2 [27]. On the other hand, metal (Ni, Co, Fe) phosphides favor decarbonylation/decarboxylation, e. g. in palmitic acid deoxygenation at 270 °C and 12 bar H_2 [28]

and in methyl laurate deoxygenation at 300 °C and 20 bar H_2 [29] which indicates a difference in the predominant path for Mo/W-carbides and Ni/Co/Fe-phosphides

Although these results indicate a difference in the predominant path for Mo/W-carbides and Ni/Co/Fe-phosphides, it is difficult to compare the performance of those materials directly because of the different reaction conditions used. Therefore, the goal of the present work is to evaluate, for the first time, the catalytic performance (activity and selectivity) of carbon nanofibers supported Mo-carbide and Ni-phosphide in the stearic acid deoxygenation at same reaction conditions (350 °C and 30 bar H_2).

2. Experimental

Catalyst synthesis

Carbon nanofibers (CNF) were synthesized using a reduced 5 wt% Ni/SiO_2 catalyst (5 g) and a mixture of hydrogen (102 mL min^{-1}), nitrogen (450 mL min^{-1}) and carbon monoxide (266 mL min^{-1}) at 550 °C and 3.8 bar for 24 hours, as previously reported [26]. The obtained CNF were refluxed in 400 mL 1M KOH for 1 hour to remove the SiO_2, followed by decanting and washing of the residue with 200 mL 1M KOH. This treatment was repeated three times. After the final reflux, the material was washed with demi water. Subsequently, the solid was treated by refluxing it in 400 mL 65% HNO_3 for 1.5 hours to remove exposed Ni and to add O_2-containing groups to the surface of the CNF. Finally, the CNF were washed with demi water to a neutral pH (measured with pH testing strips) of the washing water.

Supported molybdenum oxide was prepared by impregnating 5 g of the oxidized CNF for four times with in total 7 mL of a 0.63 M solution of $(NH_4)_2MoO_4$ (Sigma-Aldrich, 99.98% trace metals basis) using incipient wetness impregnation. Between impregnations, the impregnated material was dried in static air at 120 °C for 1 hour. The pore volume of CNF is 0.43 mL g^{-1} (BET analysis). This procedure resulted in a catalyst 7.5 wt% Mo.

The supported oxide (0.4 g) was transformed to carbide via the carbothermal method. The oxide precursor was heated from 20 °C to 800 °C (β=5 °C min^{-1}) and kept at that temperature for 6 hours under an argon flow of 100 mL min^{-1}.

Supported nickel-phosphorus oxide were prepared by impregnating 5 g of oxidized CNF in four times with in total 5 ml of a aqueous solution containing 2 mL (3.75 M) of $Ni(NO_3)_2.6H_2O$ (Sigma-Aldrich, 99.999% trace metals basis), 2 mL (3.04 M) of $(NH_4)_2HPO_4$ (Sigma-Aldrich, ACS reagent, ≥98%) and 1 mL concentrated HNO_3 (VWR Chemicals, 68%) using incipient wetness impregnation. Between impregnations, the impregnated material was dried in static air at 120 °C for 1 hour. The pore volume of CNF is 0.43 mL g^{-1} (BET analysis). This procedure resulted in 10

wt% Ni_2P.

The supported oxide (0.4 g) was transformed to phosphide via the TPR method. The oxide precursor was heated from 20 °C to 650 °C (β=1 °C min^{-1}) under an H_2 flow of 100 mL min^{-1}.

Catalysts characterization

X-Ray diffraction (XRD) of the supported Mo_2C catalyst was performed using a Rigaku Miniflex with a copper radiation (CuK_α). X-Ray diffraction (XRD) of supported Ni_2P catalyst was performed with a D2 Phaser diffractometer (Bruker) with Kα radiation of cobalt (CoKα). Diffraction patterns were measured from 2θ = 20° to 2θ = 80° with a scan rate of 2° min^{-1}. The crystalline phases were identified with the aid of the Powder Diffraction File, a database of X-ray powder diffraction patterns maintained by the International Center for Diffraction Data (ICDD). This database is part of the used JADE 5.0 software.

Nitrogen physisorption (BET) was used to assess the textural properties of the samples. Nitrogen adsorption/desorption isotherms were recorded at liquid nitrogen temperature using a Micromeritics TriStar. Before measurement the samples were pretreated in a vacuum at 400 °C for 20 hours.

Chemisorbed CO was used to quantify potential active sites. After synthesis, the samples were flushed with 50 mL min^{-1} helium at 30 ºC for 30 minutes. CO-pulse chemisorption measurements were performed using a custom-made multipurpose machine by pulsing calibrated volumes of a 20% (v/v) CO/He gas mixture over the catalyst. Mass spectrometry (Pfeiffer Vacuum, model D-35614 Asslar) was used to assess the CO uptake.

The turnover frequency (TOF) was calculated by:

$TOF(s^{-1}) = \frac{-r_A}{co_{uptake}}, -r_A = \frac{N_{A0} \times {dx_A}/{dt}}{W}$, in which $-r_A$ is the initial reaction rate (mmol g^{-1} s^{-1}), N_{A0} is the initial amount of stearic acid (mmol), ${dx_A}/{dt}$ is the derivative of stearic acid conversion at time zero (s^{-1}) and W is the amount of catalyst (g).

Transmission electron microscopy (TEM) was used to analyze particle size and size distribution. The sample was mounted on a 200-mesh copper grid covered with a pure carbon film. Samples were dusted onto the surface of the grid and any excess was removed. Analysis was performed in a JEOL JEM2100 transmission electron microscope operated at 200 kV. Images were taken (4k x 4k) with a Gatan US4000 camera. Average particle sizes were established using the ImageJ software by counting 250 to 350 particles.

Hydrodeoxygenation reaction

Hydrodeoxygenation (HDO) reactions were performed in a 100-mL stainless steel Parr autoclave reactor (4590 Micro Reactor). The reactor was filled with 2 g of stearic acid (Sigma-Aldrich, ≥ 95%, FCC, FG), 1 g of tetradecane (internal standard, Aldrich Chemistry, ≥ 99%), 0.25 g of catalyst and 50 mL of dodecane as solvent (Sigma-Aldrich, ReagentPlus ®, ≥ 99%). After purging with argon, stirring at 800 rpm was started and the reactor was heated to 350 °C. At this temperature, the total pressure was 10 bar. Subsequently, 30 bar H_2 was added to the system, resulting in a final pressure of 40 bar. Samples of 1 mL were taken during the 6-hour reaction after 0, 20, 40, 60, 120, 180, 240, 300 and 360 minutes.

Gas chromatography (GC) was used to analyze the reaction mixture (Shimadzu 2014, equipped with CP-FFAP column and photoionization detector). We used the following column temperature program: 50 °C for 1 minute, heating to 170 °C (β=7 °C min^{-1}), dwell time 1 minute, ramp to 240 °C (β=4 °C min^{-1}), dwell time 15 minutes. Prior to GC, we diluted the samples in CH_3Cl:MeOH (2:1 v/v). Trimethylsulphonium hydroxide (Sigma-Aldrich, ~ 0.25 M in methanol, for GC derivatization) was added to methylate free acids. The injected volume was 1μL for all analyses.

Theoretical calculations

Density functional theory (DFT) calculations were performed with PBE exchange-correlation functional [30], periodic boundary condition (PBC) and plane waves basis set (energy cutoff for Ni_2P = 440 eV). Integration in the first Brillouin zone was performed using Monkhorst-Pack method [31] with several different k-points mesh. Projector augmented wave approximation [32] was employed and occupation was treated by Methfessel-Paxton cold smearing technique [33] with 0.02 Ry smearing parameter. All calculations were performed in Vienna Ab Initio Simulation Package (VASP) [34].

According to Moon *et al.* [35] and to Suetin *et al.* [36], the most stable phase of Ni_2P is the hexagonal one. Super cells were constructed for modeling the principal crystallographic plane (001). A vacuum layer of about 20 Å was inserted for all super cells. After that, geometry optimizations were done with fixed cell parameters for surface relaxation. For hexagonal Ni_2P structure, the (001) crystallographic plane was considered [35] and the surface was considered by expanding (2 x 2 x 2) the unitary cell with vacuum layer in the (001) direction.

Activation energies for (O)C-OH and C-COOH bonds cleavage for butyric acid over the (001) Ni_2P surface were obtained with the climbing-image Nudged Elastic Band method [37, 38] with one image between reactants and products structures.

This choice was made because the aim is to obtain only the transition state and the activation energy for comparison between the reaction paths.

3. Results and Discussion

Figure 1 displays XRD diffractograms of CNF, Mo_2C/CNF and Ni_2P/CNF. The diffraction lines representing the CNF are indicated by blue circles. The diffractions at about 2θ = 28° and 2θ = 43° represent the (002) and (101) reflections of the CNF [39]. The diffraction lines representing Mo_2C (PDF#35-0708) (red squares) indicate the formation of the hexagonal phase of molybdenum carbide (β-Mo_2C). The diffraction lines representing nickel phosphide (PDF#03-0653) (green triangles) indicate the formation of the Ni_2P phase.

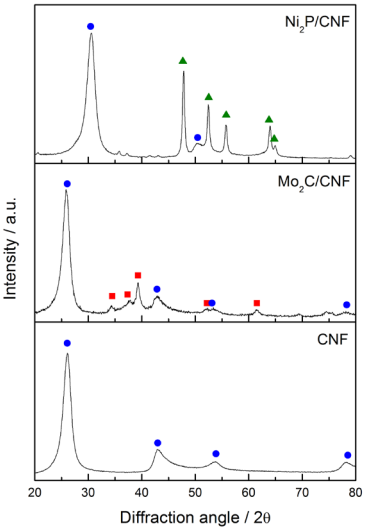

Figure 1. XRD diffractogram for ● CNF (using copper radiation), ■ Mo_2C/CNF (using copper radiation) and ▲ Ni_2P/CNF (using cobalt radiation). Due to the use of different sources the peaks appear at different positions for the same phase (most clearly seen for CNF).

Table 1 lists the textural properties of CNF, Mo_2C/CNF and Ni_2P/CNF. The parent CNF had a surface area of 180 $m^2\ g^{-1}$, which is comparable to the values reported in the literature for CNF made via the same synthesis protocol [40, 41].

Table 1. Textural properties of CNF, Mo_2C/CNF and Ni_2P/CNF.

	Surface area $m^2\ g^{-1}$	Micropore volume $cm^3\ g^{-1}$	Total pores volume $cm^3\ g^{-1}$	Pores average size nm
CNF	180	0.009	0.43	13.6
Mo_2C/CNF	130	0.001	0.40	15.5
Ni_2P/CNF	205	0.0	0.34	6.7

Mo_2C/CNF had a lower surface area (130 $m^2\ g^{-1}$) than the parent CNF (180 $m^2\ g^{-1}$). Since the molybdenum carbide precursor (MoO_3) is non-porous [42], the lower surface area of Mo_2C/CNF can be partially explained by loading of the support with the non-porous carbide.

Ni_2P/CNF displayed lower total pore volume (0.34 $cm^3\ g^{-1}$) than the parent CNF (0.43 $cm^3\ g^{-1}$), suggesting that CNF pores were partially blocked during Ni_2P/CNF synthesis. However, contrary to Mo_2C/CNF, Ni_2P/CNF showed a higher surface area (205 $m^2\ g^{-1}$) than the parent CNF (180 $m^2\ g^{-1}$). We suggest that part of the Ni-phosphide was not in contact with the support but rather had formed isolated Ni_2P particles, which are porous.

Figure 2 displays representative HR-TEM images of Mo_2C/CNF and Ni_2P/CNF catalysts. The black spots (indicated with an arrow) are most likely the active phase while the dark grey area is the CNF. Figure 3 presents histograms of the particle size distribution of the Mo_2C/CNF and Ni_2P/CNF catalysts. We found an average particle size of 6 nm (s = 9 nm) for the Mo_2C/CNF and of 9 nm (s = 7 nm) for the Ni_2P/CNF. Both samples have next to small particles also a number of large particles. For the Mo-carbide this is a clear bimodal distribution while for the Ni-phosphide the particles tail more towards larger particles. In any case this results in a large standard deviation.

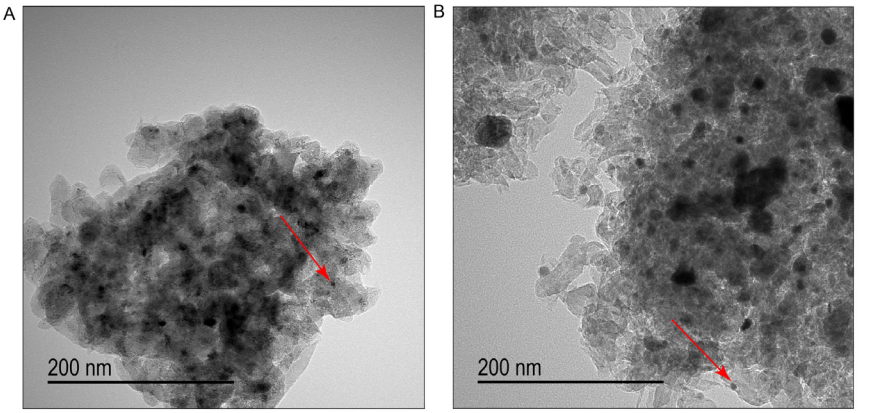

Figure 2. HR-TEM images of A) Mo_2C/CNF and B) Ni_2P/CNF.

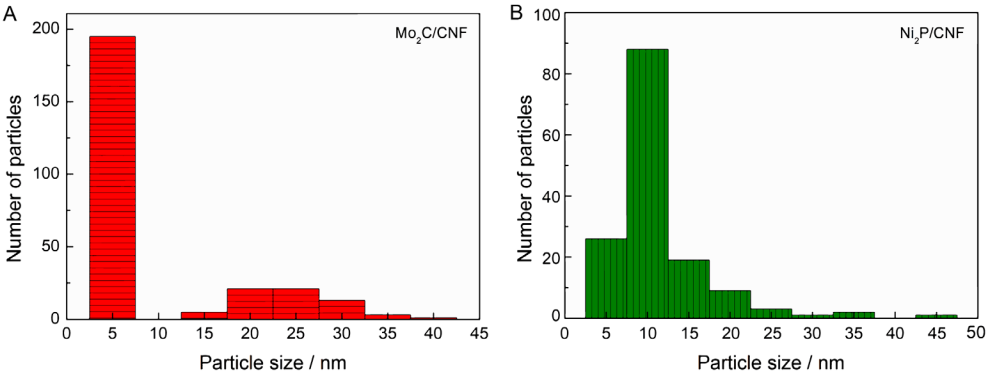

Figure 3. Particle size distribution of A) Mo_2C/CNF and B) Ni_2P/CNF.

To determine the number of potential active sites, pulse CO chemisorption was used. Table 2 displays the CO uptake of CNF, Mo_2C/CNF and Ni_2P/CNF. The uptake by Mo_2C/CNF (56 μmol g_{cat}^{-1}) was higher than the uptake by Ni_2P/CNF (5 μmol g_{cat}^{-1}), meaning that Mo_2C/CNF has more sites accessible for CO than Ni_2P/CNF. The CO chemisorption capacity of the CNF was negligible (1 μmol g_{cat}^{-1}).

Table 2. CO chemisorption uptake for CNF, Mo_2C/CNF and Ni_2P/CNF.

Sample	**CO uptake (μmol g_{cat}^{-1})**
CNF	1
Mo_2C/CNF	56
Ni_2P/CNF	5

Figure 4 shows the catalytic activity (stearic acid conversion) of Mo_2C/CNF and Ni_2P/CNF during 6 hours of reaction. Ni_2P/CNF reached 90% conversion at 180

minutes of reaction while Mo_2C/CNF only reached that conversion level after 360 minutes. Since the same amount of catalyst was employed during reaction, we conclude that, on a weight basis, the Ni_2P/CNF catalyst is more active than the Mo_2C/CNF catalyst. In fact, when the activity is normalized to the total number of binding sites (Table 2) as determined by CO uptake, the TOF for Ni_2P/CNF is 179 s^{-1} and 1 s^{-1} for Mo_2C/CNF. This indicates that Ni_2P/CNF is intrinsically more active than Mo_2C/CNF.

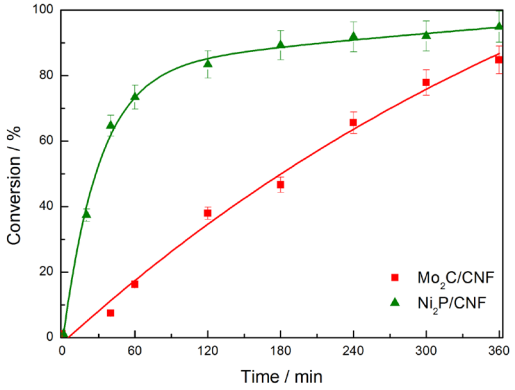

Figure 4. Stearic acid conversion over Mo_2C/CNF and Ni_2P/CNF (250 mg catalyst, 2 g stearic acid, 50 mL solvent, 30 bar H_2, T = 350 °C).

Figure 5 depicts the product distribution over time using the Mo_2C/CNF and Ni_2P/CNF for 360 minutes of reaction. For Mo_2C/CNF the major product was octadecane over irrespective of the conversion while heptadecane was the major product over Ni_2P/CNF. This result suggests that Mo_2C/CNF and Ni_2P/CNF conducted the stearic acid deoxygenation via different reaction pathways.

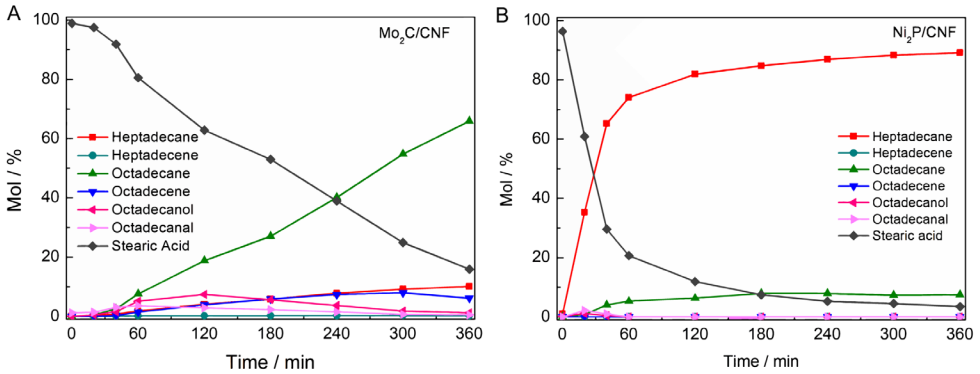

Figure 5. Stearic acid and products concentration (%mol) over time for A) Mo_2C/CNF and B) Ni_2P/CNF for stearic acid HDO (250 mg catalyst, 2 g stearic acid, 50 mL solvent, 30 bar H_2, T = 350 °C).

Figure 6 summarizes the potential pathways for stearic acid deoxygenation [40, 43]. In the DCO pathway, oxygen is removed as CO_2 (decarboxylation) or as CO and H_2O (decarbonylation) followed by hydrogenation resulting in heptadecane as final product. In the HDO pathway, oxygen is removed as H_2O producing aldehyde as the first intermediate. The aldehyde is further dehydrated and hydrogenated resulting in octadecane as final product [1]. A third reaction pathway, called HDCO, can be considered when the aldehyde (formed via hydrogenation of stearic acid) is decarbonylated, resulting in heptadecane as final product.

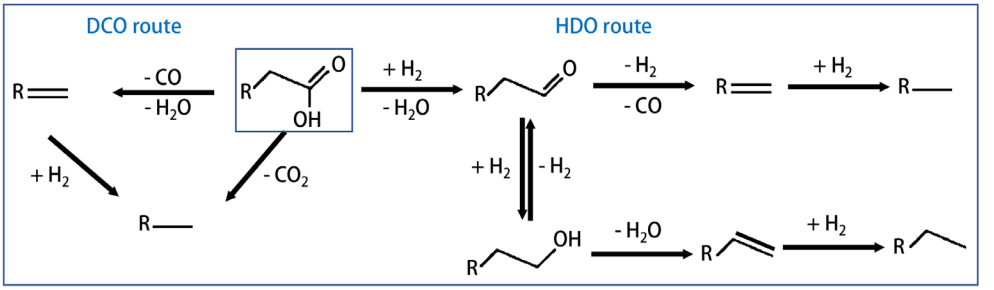

Figure 6. Pathways for deoxygenation of fatty acids.

From the catalytic data represented in Figure 5, we suggest that Mo_2C/CNF favors the HDO pathway – octadecane as the main final product – and Ni_2P/CNF favors DCO or HDCO pathway – heptadecane as the main final product. This is in accordance with literature [44, 45]. Although heptadecane is the main final product over Ni_2P/CNF, oxygenates (octadecanal and octadecanol) were formed as intermediate products suggesting that the stearic acid was first hydrogenated forming aldehyde over this catalyst. Therefore, we suggest that HDCO is the predominant pathway over nickel phosphide: first, stearic acid is hydrogenated producing aldehyde (octadecanal) and then, the aldehyde is decarbonylated producing heptadecane. In accordance, recent studies have reported that nickel phosphide conducted the palmitic acid deoxygenation via hydrogenation followed by decarbonylation, when the reaction was carried out at 240 °C and 40 bar H_2 over bulk catalyst [46].

To investigate whether indeed the HDCO pathways is easier over Ni_2P than the decarboxylation (DCO) pathway (both pathways form the same final product), DFT calculations were used to establish the activation energy of the first steps in both paths *i.e.* the activation energies for (O)C-OH splitting was compared to the C-COOH splitting. For simplicity, butyric acid was used as model compound here.

Figure 7 and Table 4 display the activation energy of (O)C-OH and C-COOH bond cleavage of butyric acid over Ni_2P/CNF catalyst. The activation energy of C-OH bond cleavage of butyric acid (12.9 kcal mol^{-1}) is significantly lower than that of

C-COOH (39.7 kcal mol^{-1}), suggesting that hydrogenation of fatty acid is the first step in the deoxygenation of stearic acid. Consequently, HDO (or HDCO) pathway is indeed more favorable to occur over Ni-phosphide catalysts in the stearic acid deoxygenation than the DCO pathway. Note that to assess which pathway HDO or HDCO is predominant over Ni-phosphide, the activation energy of C-OH and C-COH bonds cleavage of aldehyde (butanal) should also be calculated (ongoing). However, since heptadecane is the main final product over Ni-phosphide and it cannot be produced via HDO pathway, we hypothesize that stearic acid deoxygenation occurs mainly via HDCO pathway over Ni-phosphide.

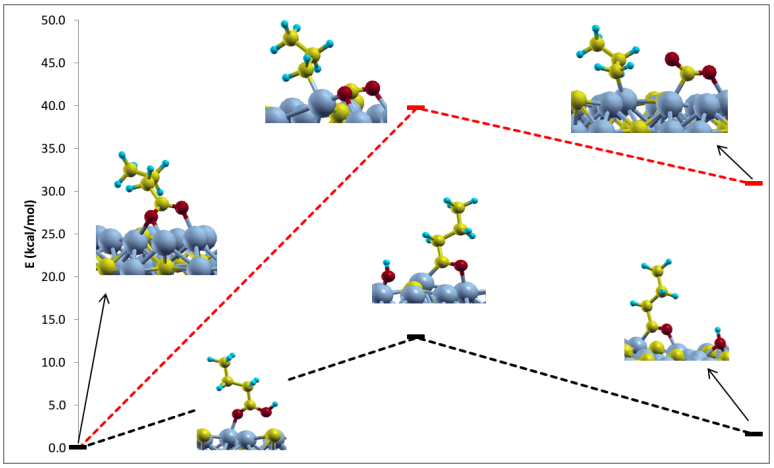

Figure 7. Activation energy and transition states during C-OH (black dashed lines) and C-COOH (red dashed lines) bonds cleavage of butyric acid over Ni_2P.

Table 4. Activation energy of C-OH and C-COO bonds cleavage for butyric acid over Ni_2P.

	Butyric acid	
	E_a (kcal mol^{-1})	**E_a (kcal mol^{-1})**
	C-OH	**C-COOH**
Ni_2P	12.9	39.7

4. Conclusion

In the present work we compared, for the first time, the catalytic performance of Mo_2C/CNF and Ni_2P/CNF in the stearic acid deoxygenation under identical conditions. Ni_2P/CNF is intrinsically more active than Mo_2C/CNF and the reaction pathways are different. Mo_2C/CNF conducts the reaction mainly via HDO, resulting in octadecane as the main product while Ni_2P/CNF conducts the reaction mainly

via HDCO pathway, resulting in heptadecane as the main product. Preliminary DFT calculations in combination with selectivity data indicate that the HDCO pathway is indeed favored over Ni-phosphide catalysts.

References

[1] R. W. Gosselink, S. A. W. Hollak, S.-W. Chang, J. van Haveren, K. P. de Jong, J. H. Bitter, D. S. van Es, ChemSusChem (2013), 6, 1576 – 1594.
[2] A. E. Coumans, E. J. M. Hensen, Appl. Catal. B: Environm. (2017), 201, 290 – 301.
[3] A. M. Robinson, J. E. Hensley, J. W. Medlin, ACS Catal. (2016), 6, 5026 – 5043.
[4] M. Grilc, B. Likozar, J. Levec, ChemCatChem (2016), 8, 180 – 191.
[5] T. Rodseanglung, T. Ratana, M. Phongaksorn, S. Tungkamania, Energy Procedia (2015), 79, 378 – 384.
[6] M. Grilc, B. Likozar, J. Levec, Appl. Catal. B: Environm. (2014), 150 – 151, 275 – 287.
[7] D. Kubicka, L. Kaluza, Appl. Catal. A: Gen. (2010), 372, 199 – 208.
[8] D. Kubicka, J. Horácek, Appl. Catal. A: Gen. (2011), 394, 9 – 17.
[9] F. Solymosi, A. Erdöhelyi, J. Mol. Catal. B – Enzym. (1980), 8, 471 – 474.
[10] R. S. Suppino, R. Landers, A. J. G. Cobo, Appl. Catal. A: Gen. (2016), 525, 41 – 49.
[11] Y. L. Louie, J. Tang, A. M. L. Hell, A. T. Bell, Appl. Catal. B: Environm. (2017), 202, 557 – 568.
[12] V. A. Vallés, B. C. Ledesma, G. A. Pecchi, O. A. Anunziata, A. R. Beltramone, Catal. Today (2017), 282, 111 – 122.
[13] I. Hachemi, K. Jenistová, P. Mäki-Arvela, N. Kumar, K. Eränen, J. Hemming, D. Yu. Murzin, Catal. Sci. Technol. (2016), 6, 1476 – 1487.
[14] Y. Nakagawa, S. Liu, M. Tamura, K. Tomishige, ChemSusChem (2015), 8, 1114 – 1132.
[15] S. Oh, H. Hwang, H. S. Choi, J. W. Choi, Fuel (2015), 153, 535 – 543.
[16] D. Gao, C. Schweitzer, H. T. Hwang, A. Varma, Ind. Eng. Chem. Res. (2014), 53, 18658 – 18667.
[17] A. Gutierrez, R. K. Kaila, M. L. Honkela, R. Slioor, A. O. I. Krause, Catal. Today (2009), 147, 239 – 246.
[18] A.-M. Alexander, J. S. J. Hargreaves, Chem. Soc. Rev. (2010), 39, 4388 – 4401.
[19] S. T. Oyama, Catal. Today (1992) 15, 179 – 200.
[20] R. Prins, M. E. Bussel, Catal. Lett. (2012) 142, 1413 – 1436.
[21] H. Ren, W. Yu, M. Salciccioli, Y. Chen, Y. Huang, K. Xiong, D. G. Vlachos, J. G. Chen, ChemSusChem (2013), 6, 798 – 801.
[22] J. Han, J. Duan, P. Chen, H. Lou, X. Zheng, H. Hong, ChemSusChem (2012), 5, 727 – 733.
[23] S. Boullosa-Eiras, R. Lodeng, H. Bergem, M. Stöcker, L. Hannevold, E. A. Blekkan, Catal. Today (2014), 223, 44 – 53.
[24] P. Bui, J. A. Cecilia, S. T. Oyama, A. Takagaki, A. H. Zhao, D. Li, E. Rodríguez-Castellón, A. J. López, J. Catal. (2012), 294, 184 – 198.
[25] K. Li, R. Wang, J. Chen, Energy Fuels (2011), 25, 854 – 863.
[26] D. R. Stellwagen, J. H. Bitter, Green Chem. (2015), 17, 582 – 593.
[27] M. M. Sullivan, A. Bhan, ACS Catal. (2016), 6, 1145 – 1152.
[28] W. Zhou, H. Xin, H. Yang, X. Du, R. Yang, D. Li, C. Hu, Catalysts (2018), 8, 153 – 173.
[29] J. Chen, H. Shi, K. Li, Appl. Catal. B: Environm. (2014), 144, 870 – 884.
[30] J. P. Perdew, K. Burke, M. Ernzerhof, Phys. Rev. Lett. (1996), 77, 3865 – 3868.
[31] H. J. Monkhorst, J. D. Pack, Phys. Rev. B (1976), 13, 5188–5192.
[32] P. E. Blöchl, Phys. Rev. B (1994), 50, 17953–17979.
[33] M. Methfessel, A. T. Paxton, Phys. Rev. B (1989), 40, 3616–3620.
[34] G. Kresse, J. Furthmüller, Phys. Rev. B (1996), 54, 11169–11186.
[35] J. -S. Moon, E. -G. Kim, Y. -K. Lee, J. Catal. (2014), 311, 144 – 152.
[36] D. V. Suetin, I. R. Shein, A. L. Ivanovskii, J. Phys. Chem. Solids (2009), 70, 64 – 71.
[37] G. Henkelman, B. P. Uberuaga, H. Jónsson, J. Chem. Phys. (2000), 113, 9901 – 9904.
[38] K. J. Caspersen, E. A. Carter, Proc. Natl. Acad. Sci. U S A (2005), 102, 6738 – 6743.
[39] ICDD PDF-2 database package http://www.icdd.com/products/pdf2.htm, accessed on DATE.
[40] R. W. Gosselink, D. R. Stellwagen, J. H. Bitter, Angew. Chem. Int. Ed., (2013), 52, 5089 – 5092.
[41] J. H. Bitter, J. Mater. Chem. 20 (2010) 7312 – 7321.
[42] L. A. Sousa, J. L. Zotin, V. Teixeira da Silva, Appl. Catal. A: Gen. (2012), 449, 105 – 111.
[43] S. A. W. Hollak, R. W. Gosselink, D. S. van Es, J. H. Bitter, ACS Catal. (2013), 3, 2837 – 2844.

[44] A. S. Rocha, L. A. Souza, R. R. Oliveira Jr., A. B. Rocha, V. Teixeira da Silva, Appl. Catal. A: Gen (2017), 531, 69 – 78.
[45] Q. Guan, F. Wan, F. Han, Z. Liu, W. Li, Catal. Today (2016), 467 – 473.
[46] M. Peroni, I. Lee, X. Huang, E. Baráth, O. Y. Gutiérrez, J. A. Lercher, ACS Catal. (2017), 7, 6331 – 6341.

Chapter 5

Influence of synthesis method on molybdenum carbide crystal structure and catalytic performance in stearic acid hydrodeoxygenation

This chapter was published in adapted form as:
L. Souza Macedo, R. R. Oliveira Jr., T. van Haasterecht, V. Teixeira da Silva, H. Bitter, Influence of synthesis method on molybdenum carbide crystal structure and catalytic performance in stearic acid hydrodeoxygenation, ***Applied Catalysis B: Environmental***, 241, **2019**, 81 – 88.

Abstract

The role of the synthesis method of molybdenum carbide nanoparticle catalysts supported on carbon nanofibers on crystal structure and on catalytic performance in hydrodeoxygenation of stearic acid was investigated. We obtained the cubic phase of molybdenum carbide (α-MoC_{1-x}) by impregnating carbon nanofibers with a solution of $(NH_4)_2MoO_4$, then exposing them to 20% CH_4/H_2 at 650 °C for 2 hours. When increasing the Mo loading from 7.5 wt% to 20 wt% or using the carbothermal reduction method, *i.e.* using carbon from the support to reduce the $(NH_4)_2MoO_4$ precursor at 800 °C for 6 hours, the hexagonal phase (β-Mo_2C) resulted.

Experiments with stearic acid hydrodeoxygenation showed that both phases (7.5 wt% Mo) displayed similar intrinsic activities. However, α-MoC_{1-x}/CNF reached 80% stearic acid conversion after 240 minutes while the β-Mo_2C/CNF catalyst attained the same conversion after 360 minutes. CO chemisorption results showed that α-MoC_{1-x}/CNF and β-Mo_2C/CNF have a similar number of potential active sites (66 and 56 μmol g^{-1}, respectively). We attribute the difference in catalytic performance between α-MoC_{1-x}/CNF and β-Mo_2C/CNF to differences in the catalyst's crystal structure, more specifically, the associated site density. The face-centered cubic α-MoC_{1-x}/CNF has a lower site density (0.1096 Mo atoms $Å^{-2}$) than the hexagonal close-packed β-Mo_2C/CNF (0.1402 Mo atoms $Å^{-2}$), making the Mo atoms at the surface of the α-MoC_{1-x} phase more accessible for large reactant molecules such as stearic acid thus allowing its conversion in shorter times.

1. Introduction

Noble metals are widely used in catalysis, amongst others, for reactions such as (de)hydrogenation, hydrogenolysis and Fischer-Tropsch synthesis [1]. However, noble metals are scarce, hence expensive, which makes it desirable to find more abundant alternatives.

Since the seminal work of Levy and Boudart [2], it has become clear that transition metal carbides are efficient catalysts for reactions that involve the transfer of hydrogen, such as ammonia synthesis, hydrogenation, hydrogenolysis, isomerization, methanation and hydroprocessing [3]. Lately, W and C carbides have gained interest as active catalysts for biomass conversion, e.g. in the conversion of lignin, hemicellulose and cellulose [4 – 7] or in the conversion of triglycerides [8, 9]. Recently, we showed that Mo and W carbide catalysts are also active for biomass-related conversions such as deoxygenation stearic and oleic acids [10 – 12] and gamma-valerolactone production via levulinic acid hydrogenation [13].

For a number of reactions, transition metal carbides display similar or even better catalytic performance than noble metal catalysts. For example, Dhandapani *et al.* [14] found that Mo_2C is more active than Pt/γ-Al_2O_3 for cumene hydrogenation and Li *et al.* [15], Claridge *et al.* [16] and Choi *et al.* [17] reported that the catalytic activity of the transition metal carbides Ni-W_2C, Mo_2C and W_2C can compete with that of noble metal catalysts in wood lignin degradation, conversion of methane to synthesis gas and benzene hydrogenation, respectively.

A typical method to synthesize transition metal carbides, especially molybdenum and tungsten carbides, is the temperature-programmed reaction (TPR) method [3]. First, a support is impregnated with a soluble oxidic precursor and then the sample is calcined forming a supported oxide. In the next step, the oxide is heated in a carbon-containing atmosphere such as methane or butane ([10, 18]), which converts the oxide into the carbide. Depending on the carburizing gas composition during TPR, different crystallographic structures of the final catalyst result. For example, Xiao *et al.* [18] produced the face-centered-cubic form of molybdenum carbide after synthesis with 5% C_4H_{10} and 95% H_2 as carburizing gas, while Sousa *et al.* [10] created hexagonal molybdenum carbide after synthesis with 20 % CH_4 and 80% H_2 as carburizing gas, both at 650 °C for 2 hours and using supported molybdenum trioxide as precursor.

Another method used to synthesize transition metal carbides is carbothermal reduction [19]. A carbon-based support impregnated with an oxidic precursor is heated in a carbon-free atmosphere. The carbide forms by reaction of the oxide with carbon from the support [11, 12, 19 – 23]. This method has the advantage of avoiding carbon deposition on the catalyst surface, which commonly occurs with the

TPR method due to methane (or hydrocarbon) decomposition [3].

Despite the increasing number of reports that show the potential of transition metal carbides as catalysts for various reactions, they are not widely used in commercial applications. Here, we try to understand the property-performance relationship for the carbides to advance that field [3, 24 – 26].

Controlling the crystal structure of the carbides is important because it can have a significant influence on catalytic performance, although there are cases in which crystal structure does not influence catalytic performance. For example, α-MoC_{1-x} and β-Mo_2C phases displayed a similar catalytic activity for isopropanol dehydration at 140 °C in an inert He/Ar atmosphere as well as in 13 kPa O_2 [27]. On the other hand, for dehydrogenation of benzyl alcohol [28], steam reforming of methanol [29] and hydrogenation of toluene [30], β-Mo_2C was more active than α-MoC_{1-x} while α-MoC_{1-x} was more active than β-Mo_2C for CO hydrogenation to produce methane [31].

Various ways exist to control the crystal structure of the carbide, such as by temperature, nature of the oxidic precursor, percentage of weight-loading and carburizing atmosphere composition [27 – 29, 31 – 34]. For example, the combination of a low temperature (250 to 400 °C) with an H_2 atmosphere seems to favor the formation of a molybdenum bronze phase (H_xMoO_3, [35]) which is then topotactically transformed into the cubic molybdenum carbide phase, even in the case of a low carbon content (supplied C/Mo molar ratio = 0.6) [30]. The cubic phase also forms in the absence of H_2 at a high temperature (800 °C) and a supplied C/Mo ratio of 6.3 [30]. However, using a supplied C/Mo ratio of 2, no H_2 and a high temperature (800 °C) yields the hexagonal phase form [30]. Frank *et al.* [29] compared the TPR and carbothermal reduction methods for carbon-nanotube-supported molybdenum carbides and found that TPR of $(NH_4)_6Mo_7O_{24}.4H_2O$ in 20% CH_4/H_2 results in 2-nm crystallites of cubic α-MoC_{1-x} whereas TPR in pure H_2 and using the carbothermal method with He yields larger (8 to 10 nm) particles of hexagonal β-Mo_2C. Li *et al.* [28] showed that carburization of a bulk α-MoO_3 precursor in 20% CH_4/H_2 at 850 °C for 4 hours results in the hexagonal β-Mo_2C phase, while α-MoC_{1-x} phase forms during TPR with 5% n-C_4H_{10}/H_2 at 700 °C for 4 hours.

Though a consistent picture of the role of crystal structure on catalytic performance is still lacking, explanations have been put forward for the differences in the catalytic properties of these two molybdenum carbide forms, including differences in the reactant's adsorption energy [31] and differences in the (inadvertent) coverage of Mo atoms by carbon as occurs with the TPR method [28, 30].

Comparisons of the catalytic performance of both forms in reactions involving lipid-based biomass, such as used in the production of olefins and paraffins, are

still lacking. In this paper, we report on an investigation into the influence that the synthesis history of α-MoC_{1-x} or β-Mo_2C supported on carbon nanofibers has on their characteristics and performance as catalysts for the hydrodeoxygenation of stearic acid. We tested the catalysts under identical conditions to gain insight in the structure-performance relationship.

2. Experimental

Synthesis

Carbon nanofibers (CNF) were synthesized from a reduced 5 wt% Ni/SiO_2 catalyst (5 g) and a mixture of hydrogen (102 mL min^{-1}), nitrogen (450 mL min^{-1}) and carbon monoxide (266 mL min^{-1}) at 550 °C and 3.8 bar for 24 hours, as previously reported [12]. Next, the CNF were refluxed in 400 mL 1M KOH for 1 hour to remove the SiO_2, followed by decanting and washing of the residue with 200 mL 1M KOH. This treatment was repeated three times. After the final reflux, the material was washed with demi water. Subsequently, the solid was treated by refluxing it in 400 mL 65% HNO_3 for 1.5 hours to remove exposed Ni and to add O_2-containing groups to the surface of the CNF. Finally, the CNF were washed with demi water to a neutral pH (measured with pH testing strips) of the washing water.

Supported oxides were prepared by impregnating 5 g of CNF four times with 7 mL of a 0.63 M solution of $(NH_4)_2MoO_4$ (Sigma-Aldrich, 99.98% trace metals basis) using incipient wetness impregnation. Between impregnations, the impregnated materials were dried in static air at 120 °C for 1 hour. The pore volume of CNF is 0.43 mL g^{-1} (B.E.T analysis). This procedure resulted in a catalyst loading of 7.5 wt% Mo. For a Mo loading of 20 wt%, 5 g of CNF were impregnated ten times with in total 20 mL of a 1.86 M solution of $(NH_4)_2MoO_4$.

The supported oxides (0.4 g) were transformed to carbides in two different ways, namely via the TPR method and via the carbothermal reduction method. In the TPR method, the precursor was exposed to 20% CH_4/H_2 (CH_4 = 20 mL min^{-1} and H_2 = 80 mL min^{-1}). The temperature was increased from room temperature (20 °C) to 650 °C (β=2.5 °C min^{-1}) and maintained at that temperature for 2 hours. For carbothermal reduction, the precursor was heated from 20 °C to 800 °C (β=5 °C min^{-1}) and kept at that temperature for 6 hours under an argon flow of 100 mL min^{-1}.

Characterization

In-situ X-ray diffraction (XRD) was performed with a Rigaku DMax 2200 equipped with an Anton Paar XRK-900 reaction chamber, a Cu K_α tube and a graphite monochromator. Diffraction patterns were measured from 2θ = 20° to 2θ = 80° with a scan rate of 2° min^{-1}.

Samples were carburized in situ by using either 100 mL min^{-1} 20% CH_4/H_2 (TPR method) or argon (carbothermal reduction). The phase changes were followed by recording diffractograms at different temperatures. Between measurements, the sample was heated to the next temperature at 2.5 and 5 °C min^{-1} for TPR and carbothermal reduction, respectively.

The crystalline phase was identified with the aid of the Powder Diffraction File, a database of X-ray powder diffraction patterns maintained by the International Center for Diffraction Data (ICDD). This database is part of the JADE 5.0 software.

Nitrogen physisorption was used to assess the textural properties of the samples. Nitrogen adsorption/desorption isotherms were recorded at liquid nitrogen temperature using a Micromeritics TriStar. Before measurement the samples were pretreated in a vacuum at 400 °C for 20 hours.

To assess the number of (potentially) active sites, we used CO chemisorption. Supported oxides (0.1 g) were first pretreated with 50 mL min^{-1} He at 500 °C for 30 minutes. Then the temperature was lowered and the catalyst was activated via carburization (20 mL min^{-1} CH_4 and 80 mL min^{-1} H_2) or carbothermal reduction (100 mL min^{-1} He). Samples were cooled down to 30 °C and flushed with He (50 mL min^{-1}) for 30 minutes. CO-pulse chemisorption measurements were performed using a custom-made multipurpose instrument by pulsing calibrated volumes of a 20% (v/v) CO/He gas mixture over the catalyst. Mass spectrometry (Prisma, equipped with a Pfeiffer vacuum pump, model D-35614) was used to assess the CO uptake.

As shown in the Suplementary Information, we calculated turnover frequency (TOF) with the equation:

$$TOF(s^{-1}) = \frac{-r_A}{co_{uptake}}, -r_A = \frac{N_{A0} \times {dx_A}/{dt}}{W}$$

, in which $-r_A$ is the initial reaction rate (mmol g^{-1} s^{-1}), N_{A0} is the initial amount of stearic acid (mmol), ${dx_A}/{dt}$ is the derivative of stearic acid conversion at time zero (s^{-1}) and W is the amount of catalyst (g).

Temperature-programmed desorption (TPD) of CO was carried out after CO chemisorption. Samples were heated from 20 °C to 1000 °C under He flow (100 mL min^{-1} and β = 15 °C min^{-1}) and the signal of ion m/z = 28 was followed in the mass spectrometer.

Transmission electron microscopy (TEM) was used to analyze particle size and size distribution. We mounted the samples on a 200-mesh copper grid covered with a pure carbon film. Samples were dusted onto the surface of the grid and any excess was removed. Analysis was performed in a JEOL JEM2100 transmission electron microscope operated at 200 kV. We took images (4k x 4k) with a Gatan US4000 camera. We calculated average particle sizes with ImageJ software, on the

basis of 250 to 350 particles.

Hydrodeoxygenation

Hydrodeoxygenation (HDO) reactions were performed in a 100-mL stainless steel Parr autoclave reactor (4590 Micro Reactor). The reactor was filled with 2 g of stearic acid (Sigma-Aldrich, ≥ 95%, FCC, FG), 1 g of tetradecane (internal standard, Aldrich Chemistry, ≥ 99%), 0.25 g of catalyst (they were transferred directly from the synthesis equipment to the reactor by exposing them shortly to air) and 50 mL of dodecane as solvent (Sigma-Aldrich, ReagentPlus ®, ≥ 99%). After purging with argon, stirring at 800 rpm was started and the reactor was heated to 350 °C. At this temperature, the total pressure was 10 bar. Subsequently, 30 bar H_2 was added to the system, resulting in a final pressure of 40 bar. Samples of 1 mL were taken during the 6-hour reaction after 0, 20, 40, 60, 120, 180, 240, 300 and 360 minutes.

Gas chromatography (GC) was used to analyze the reaction mixture (Shimadzu 2014, equipped with CP-FFAP column and photoionization detector). We used the following column temperature program: 50 °C for 1 minute, heating to 170 °C (β=7 °C min^{-1}), dwell time 1 minute, ramp to 240 °C (β=4 °C min^{-1}), dwell time 15 minutes. Prior to GC, we diluted the samples in CH_3Cl:MeOH (2:1 v/v). Trimethylsulphonium hydroxide (Sigma-Aldrich, ~ 0.25 M in methanol, for GC derivatization) was added to methylate free acids. The injected volume was 1μL for all analyses.

3. Results and discussion

3.1 *Synthesis*

Figure 1 displays the in-situ XRD diffractograms of an impregnated, supported 7.5 wt% Mo precursor during its transformation via the carbothermal reduction method. The relevant phases are the MoO_2 phase (indicated by the purple triangles) and the hexagonal β-Mo_2C phase (indicated by the red squares).

The diffractions at about 2θ = 28° and 2θ = 43° represent the (002) and (101) reflections of the CNF [36]. Up to 500 °C, no other reflections were visible, indicating that the impregnated oxidic phase either consisted of very small crystallites or was amorphous. In the temperature range of 500 to 700 °C, diffraction lines representing MoO_2 (PDF# 32-0671) became visible. At 800 °C, these reflections started to disappear again and the reflection representing β-Mo_2C (PDF#35-0708) appeared. The β-Mo_2C reflections sharpened when the catalyst was held at 800 °C for a prolonged time (up to 6 hours). Please note that the intensity of the CNF peak decreased during the experiment. We tentatively attribute this to the absorption of the X-rays by the large molybdenum carbide particles formed during the synthesis,

as has previously been shown for Mo/ZSM-5 [37].

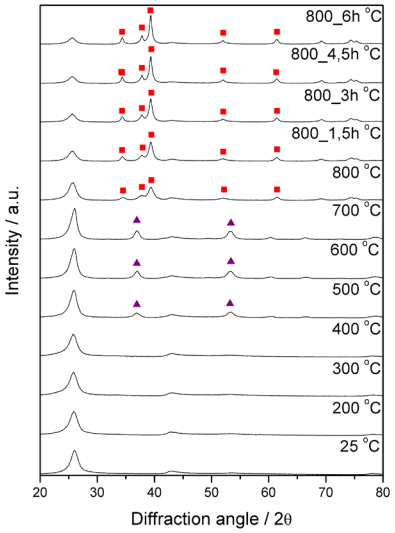

Figure 1. In-situ XRD diffractogram for 7.5 wt% Mo_2C/CNF synthesized via carbothermal reduction with argon (with ■ indicating hexagonal β-Mo_2C and ▲ MoO_2).

Figure 2 displays the diffractograms of an impregnated, supported 7.5 wt% Mo precursor during its transformation when using the TPR method with 20% CH_4/H_2 as carburization gas mixture. The blue rhombi indicate the reflections representing the cubic α-MoC_{1-x} phase.

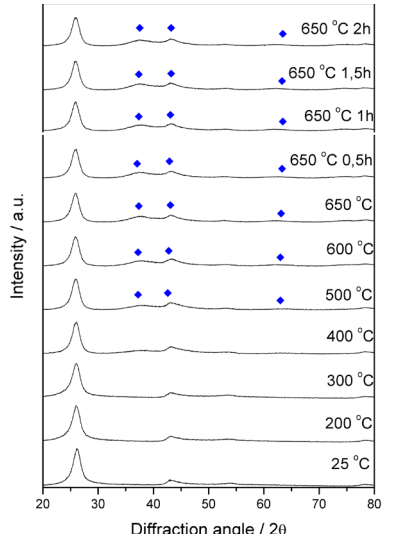

Figure. 2. In-situ XRD diffractogram for 7.5 wt% Mo_2C/CNF synthesized via carburization with 20% CH_4/H_2 gas mixture (◆ indicates cubic α-MoC_{1-x}).

The signals at about 2θ = 28° and 2θ = 43° represent the (002) and (101) reflections of the CNF [36]. Up to 500 °C, no other reflections were visible, which indicates that the impregnated oxidic phase either consisted of very small crystallites or was amorphous. In the temperature range of 500 °C to 650 °C, diffraction lines (blue rhombus) representing the α-MoC_{1-x} phase (PDF#15-0457) became visible. The diffraction lines of α-MoC_{1-x} were too broad and their intensity was too low to allow calculation of the crystallite size. In fact, Sebakhy *et al.* [38] found similar results when synthesizing cubic and hexagonal molybdenum carbides. The bulk β-Mo_2C (hexagonal) presented a defined XRD diffractogram with narrow signals and average particle size of 37 nm and, on the other hand, the bulk α-MoC_{1-x} (cubic) presented broad signal on the XRD diffractogram and an average particle size of 2 nm.

To summarize, synthesis via carbothermal reduction resulted in the hexagonal β-Mo_2C phase while synthesis via TPR method in 20% CH_4/H_2 produced cubic α-MoC_{1-x}.

Previous research has shown that the α-MoC_{1-x} phase forms at higher C/Mo ratios and the β-Mo_2C phase at lower C/Mo ratios [28, 30]. Therefore, we also prepared a 20 wt% Mo sample (C/Mo molar ratio = 746, see Appendix B) under the same synthesis conditions as for the 7.5 wt% Mo (C/Mo molar ratio = 1989). XRD patterns of 20 wt% Mo supported molybdenum carbide synthesized via TPR with 20% CH_4/H_2 at 650 °C for 2 hours shows that using the lower C/Mo ratio resulted in β-Mo_2C (Figure B2), in line with what others have reported.

3.2 Characterization

From now on, we will only consider the 7.5 wt% Mo samples because we are interested in comparing the α-MoC_{1-x}/CNF and β-Mo_2C/CNF catalysts on a weight basis. Table 1 lists the textural properties of CNF, α-MoC_{1-x}/CNF and β-Mo_2C/CNF. The parent CNF had a surface area of 180 $m^2\ g^{-1}$, which is comparable to the values reported in the literature for CNF made via the same synthesis protocol [11, 39]. Cubic α-MoC_{1-x}/CNF and hexagonal β-Mo_2C/CNF showed a similar surface area, of 140 $m^2\ g^{-1}$ and 130 $m^2\ g^{-1}$, respectively, which is lower than that of the parent CNF. Since molybdenum carbide precursor (MoO_3) is non-porous [10], the lower surface area of the supported catalysts can be partially explained by loading of the support with the carbides. However, this cannot fully explain the decrease in surface area, since only 7.5 wt% Mo was loaded. This suggests that part of the pores of the support were blocked by the carbides. This idea is supported by the significant decrease (higher than the 7.5% from the added MoO_3) we found in the micropore area of the catalysts (from 20 $m^2\ g^{-1}$ to 2 and 4 $m^2\ g^{-1}$ for α-MoC_{1-x}/CNF and β-Mo_2C/CNF, respectively) and the micropore volume (from 0.009 $cm^3\ g^{-1}$ to 0 and 0.001 $cm^3\ g^{-1}$ for α-MoC_{1-x}/

CNF and β-Mo_2C/CNF, respectively) relative to the pure CNF. We tentatively explain the smaller pore area of α-MoC_{1-x}/CNF by the presence of carbonaceous deposits on that sample formed due to methane decomposition. Since that sample was prepared by the TPR method, deposits could have formed from decomposition of the carbon source (CH_4) during synthesis [3].

Table 1. Textural properties of CNF, α-MoC_{1-x}/CNF and β-Mo_2C/CNF (7.5 wt% Mo).

	Surface Area ($m^2\ g^{-1}$)	**Micropore Area ($m^2\ g^{-1}$)**	**Micropore Volume ($cm^3\ g^{-1}$)**	**Pore volume ($cm^3\ g^{-1}$)**	**Pores average size (Ă)**
CNF	180	20	0.009	0.43	136
α-MoC_{1-x}/CNF	140	2	0	0.31	100
β-Mo_2C/CNF	130	4	0.001	0.40	155

Figure 3 displays representative HR-TEM images of α-MoC_{1-x}/CNF and β-Mo_2C/CNF. Black spots indicate the presence of the carbide or partly oxidized carbide (indicated with the red arrows) and the dark grey area is the CNF. Figure 4 presents histograms of the particle size distribution of the α-MoC_{1-x}/CNF and β-Mo_2C/CNF catalysts. We found an average particle size of 2 nm (s = 1.4 nm) for the α-MoC_{1-x}/CNF and of 6 nm (s = 9 nm) for the β-Mo_2C/CNF. The latter sample has a bimodal distribution with a few very large particles, resulting in a large standard deviation. The smaller particle size node appears similar to that of α-MoC_{1-x}/CNF particles (Figure 4A), what can implicate that the smaller particles in Figure 4B begin as α-MoC_{1-x} and larger particles convert into the β-Mo_2C. XRD diffractograms in Figure 2 show that the formation of α-MoC_{1-x} phase is connected to the peaks at 2θ = 37.8° and 43°, but the peak at 2θ = 43° is also connected to the CNF support. Thus, we only can associate the formation of α-MoC_{1-x} phase to the diffractogram peak at 2θ = 37.8°. Since we cannot clearly see a shoulder/peak at 2θ = 37.8° in Figure 1 (β-Mo_2C/CNF), we cannot exclude that some α-MoC_{1-x} is present in the β-Mo_2C/CNF catalyst. Note that the comparison of catalytic performance between α-MoC_{1-x}/CNF and β-Mo_2C/CNF catalysts will not be compromised even if some α-MoC_{1-x} is present in the β-Mo_2C/CNF catalyst because the performance of the pure α-MoC_{1-x} phase is obtained by α-MoC_{1-x}/CNF catalyst. Therefore, any difference in the performance of β-Mo_2C/CNF catalyst must be attributed to the β-Mo_2C phase.

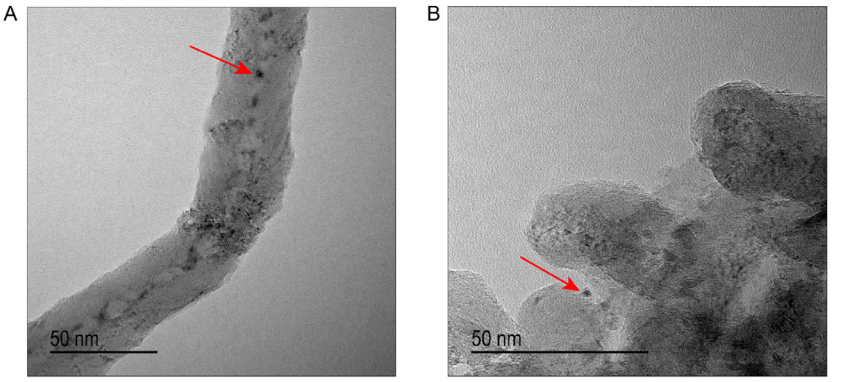

Figure 3. HR-TEM images of A) α-MoC_{1-x}/CNF and B) β-Mo_2C/CNF.

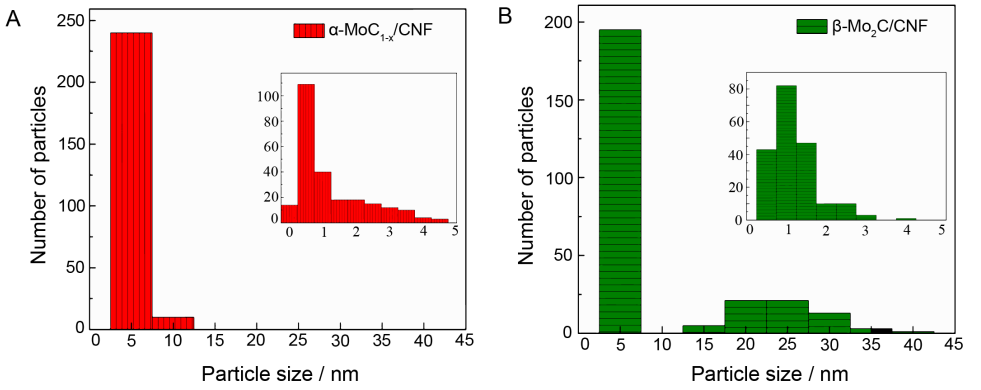

Figure 4. Particle size distribution of A) α-MoC_{1-x}/CNF and B) β-Mo_2C/CNF. Secondary graphs represents a detail up to 5 nm.

To determine the number of potential active sites, pulse CO chemisorption was used. Table 2 shows the CO chemisorption uptakes of CNF, α-MoC_{1-x}/CNF and β-Mo_2C/CNF. CO chemisorption uptake by α-MoC_{1-x}/CNF (66 μmol g_{cat}^{-1}) was slightly higher than CO chemisorption uptake by β-Mo_2C/CNF (56 μmol g_{cat}^{-1}), meaning that α-MoC_{1-x}/CNF has more sites accessible for CO than β-Mo_2C/CNF. The CO chemisorption capacity of the CNF was negligible (1 μmol g_{cat}^{-1}).

In line with other studies [17, 40 – 42], we used the CO chemisorption uptake to determine the number of potential active sites. However, this is not undisputed. For example, Clair *et al.* [43] argued that only 14% of the total number of surface Mo atoms is titrated via CO chemisorption over hexagonal molybdenum carbide (0001). For the sake of completeness and comparison, we therefore also report the particles size as calculated via TEM and XRD analysis (Table B1).

Table 2. CO chemisorption uptake for CNF, α-MoC_{1-x}/CNF and β-Mo_2C/CNF.

	CO uptake (μmol g^{-1})
CNF	1
α-MoC_{1-x}/CNF	66 ± 3.3
β-Mo_2C/CNF	56 ± 2.8

Though pulse chemisorption provides information on the number of available sites, it does not reveal anything about the nature of the sites (CO binding strength). We assessed the latter by performing CO temperature-programmed desorption (TPD) after the chemisorption experiment. Figure 5 displays the CO TPD trace for α-MoC_{1-x}/CNF and β-Mo_2C/CNF. α-MoC_{1-x}/CNF presented a defined CO desorption peak in the temperature region of 50 °C to 200 °C with a maximum at 85 °C and β-Mo_2C/CNF presented a clear CO desorption peak at 90 °C and a second peak at 150 °C. Frank *et al.* [29], Nagai *et al.* [44] and Shi *et al.* [45] have attributed these different binding strengths to CO bonds at the Mo sites (desorption at 85 °C to 90 °C) and at the C sites (desorption at 150 °C).

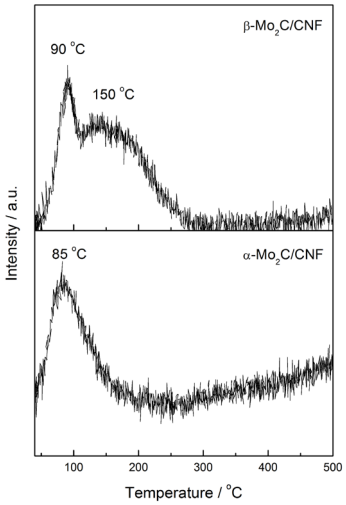

Figure 5. Temperature-programmed desorption of CO for α-MoC_{1-x}/CNF and β-Mo_2C/CNF.

3.3 Catalytic activity

Figure 6 shows the catalytic activity (stearic acid conversion) of α-MoC_{1-x}/CNF and β-Mo_2C/CNF during 6 hours of reaction. Since both catalysts contain the same amount of carbide, the conclusion is that on a weight basis, the catalyst containing the α-MoC_{1-x} phase is more active than the catalyst with the β-Mo_2C

phase. However, when the activity is normalized to the total number of binding sites (Table 2) as determined by CO uptake, the TOF is 3 s^{-1} for α-MoC_{1-x} and 1s^{-1} for β-Mo_2C. This indicates that both catalysts have a similar intrinsic activity. We also carried out a reaction in which we used the pure CNF support. As Figure 6 shows, the activity of CNF alone was an order of magnitude lower than that of the catalysts.

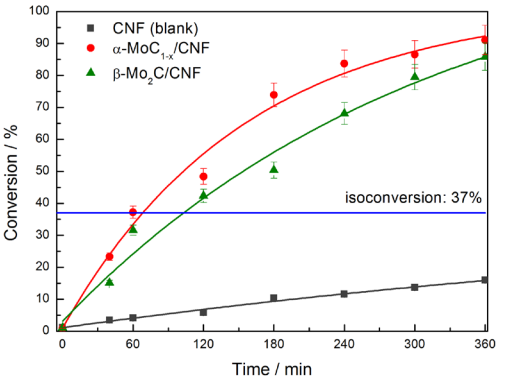

Figure 6. Stearic acid conversion over α-MoC_{1-x}/CNF and β-Mo_2C/CNF (250 mg catalyst, 2 g stearic acid, 50 mL solvent, 30 bar H_2, T = 350 °C). The lines are added to guide the eyes.

Figure 7 depicts the product distribution of α-MoC_{1-x}/CNF (7A) and β-Mo_2C/CNF (7B) for 360 minutes of reaction. Both catalysts yielded heptadecane, heptadecene, octadecane, octadecene, octadecanol and octadecanal as intermediates or final products, indicating that the reaction pathway is probably the same for both catalysts. However, the intermediate compounds were produced and consumed at different times.

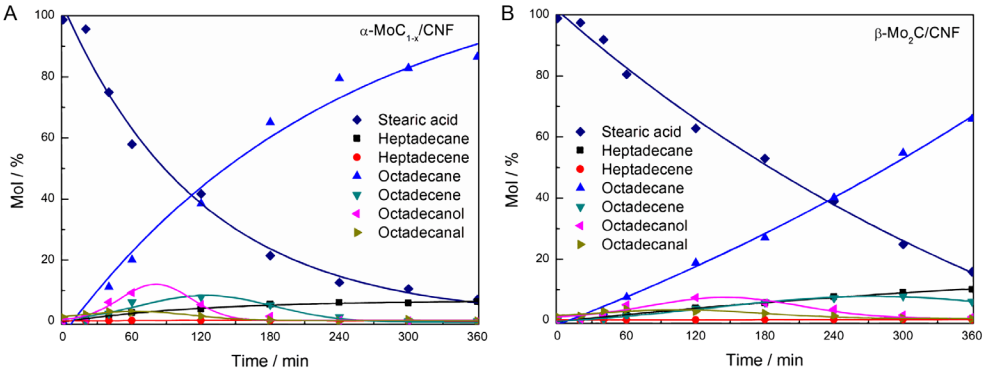

Figure 7. Product concentration (%mol) over time for A) α-MoC_{1-x}/CNF and B) β-Mo_2C/CNF for stearic acid HDO (250 mg catalyst, 2 g stearic acid, 50 mL solvent, 30 bar H_2, T = 350 °C). The lines are added to guide the eyes.

To analyze the production and consumption of intermediate compounds over the α-MoC_{1-x}/CNF and β-Mo_2C/CNF catalysts, we looked at the evolution of heptadecene, octadecene, octadecanal and octadecanol over time (Figure 8). Octadecanal and octadecanol were formed and consumed at different rates over the two catalysts. Over α-MoC_{1-x}/CNF, the intermediates were completely consumed after 240 minutes, while they were not fully consumed yet after 300 minutes over β-Mo_2C/CNF. Moreover, octadecene reached a maximum concentration at 120 minutes over the α-MoC_{1-x}/CNF catalyst while that point was only reached after 300 minutes for β-Mo_2C/CNF. This confirms in greater detail that although the reaction pathway is the same and the same intermediates (heptadecene, octadecene, octadecanal and octadecanol) were present during stearic acid HDO over α-MoC_{1-x}/CNF and β-Mo_2C/CNF, they were produced and consumed at different times.

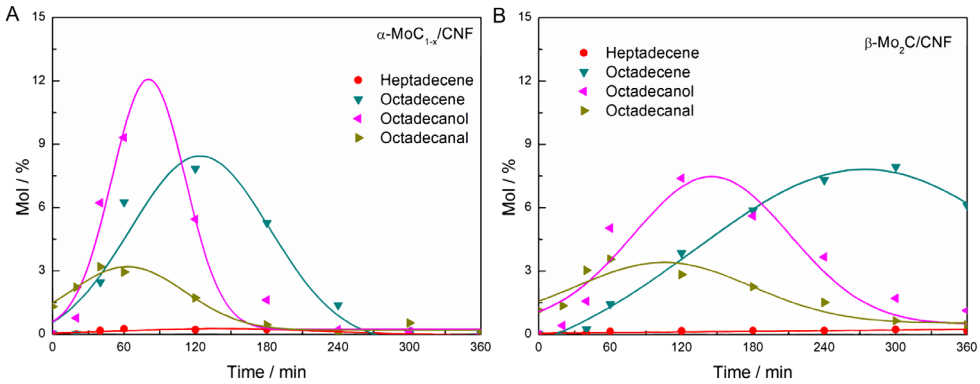

Figure 8. Detail of intermediate product concentration (%mol) over time for A) α-MoC_{1-x}/CNF and B) β-Mo_2C/CNF during stearic acid HDO (250 mg catalyst, 2 g stearic acid, 50 mL solvent, 30 bar H_2, T = 350 °C). The lines are added to guide the eyes.

Figure 9 presents the selectivities of both catalysts at the same conversion of 3.5 % (Figure 9A) and 37% (Figure 9B), to enable a fair comparison. Clearly, both phases resulted in similar product distributions at those conversion. While oxygenates (octadecanal + octadecanol) are the main product at 3.5% conversion octadecane is the main product at 37% conversion. This indicates that the hydrodeoxygenation (HDO) pathway, although not exclusive, is dominant over both catalysts.

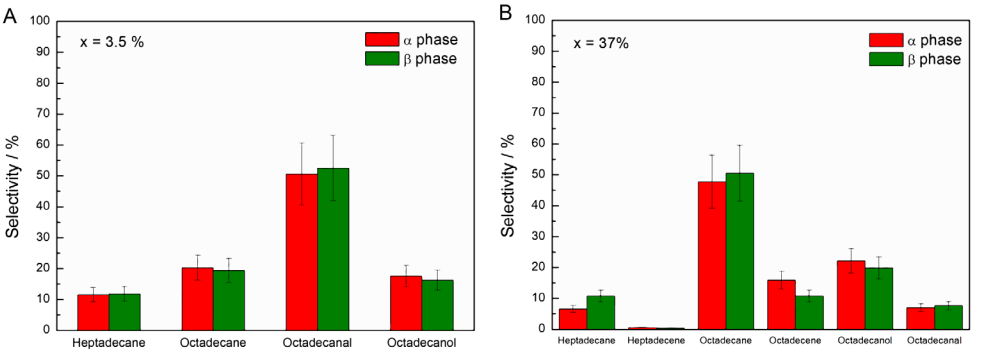

Figure 9. Product distribution of α-MoC_{1-x}/CNF and β-Mo_2C/CNF catalysts for stearic acid HDO (250 mg catalyst, 2 g stearic acid, 50 mL solvent, 30 bar H_2, T = 350 °C) at isoconversion of A) 3.5% and B) 37%.

During HDO, stearic acid is first hydrogenated to form octadecanal. Octadecanal can be either dehydrogenated and decarbonylated to form heptadecane or hydrogenated to form octadecanol. Octadecanol is dehydrated to form octadecene, which is hydrogenated to octadecane [10 – 12, 46]. Though HDO is the major pathway some heptadecane is formed which indicates that also decarbonylation/ hydrogenation and/or decarboxylation (DCO) plays a small role as shown before [11, 12]. Figure 10 illustrates the reaction pathways in stearic acid deoxygenation. The predominant pathway over the Mo carbides (HDO) is indicated by red arrows.

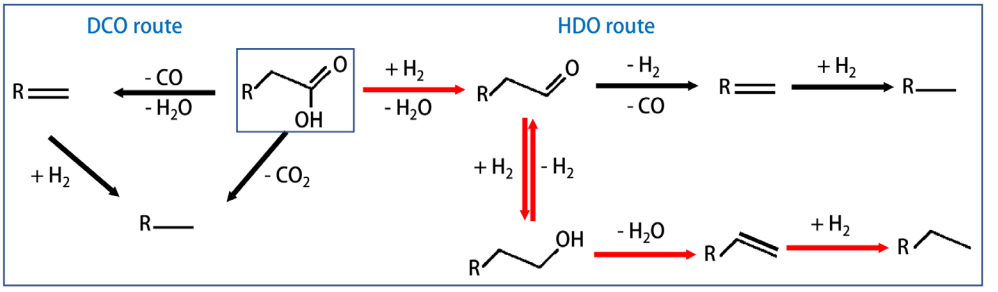

Figure 10. Scheme of reaction pathways in deoxygenation of stearic acid, red arrow indicate the dominant pathway over Mo-carbides.

Since we found similar TOF values and selectivities for α-MoC_{1-x}/CNF and β-Mo_2C/CNF in the stearic acid HDO, we concluded that the same catalytic sites were involved in this reaction. However, α-MoC_{1-x}/CNF provided faster hydrodeoxygenation (on a weight basis) than β-Mo_2C/CNF, which may be attributed to either carbide particle size or active site density. However, we showed before [12] by comparing beta Mo_2C/CNF with small (2 nm) and large carbide particles (11 nm) that the

smaller particles were less active. In contrast, here the catalyst with the smaller particle size (α-MoC_{1-x}/CNF) is more active than the catalyst with larger particle size (β-Mo_2C/CNF). Therefore, we attribute the difference in activity to difference in the crystal phase of the carbide. To gain some insight in the influence of site density on HDO, we calculated (Table 3) the site density for α-MoC_{1-x}/CNF and β-Mo_2C/CNF based on their crystallographic structures. Figure 11 shows the unit cells and the atom configuration of specific planes for the face-centered cubic (fcc) and hexagonal close-packed (hcp) molybdenum carbide structures.

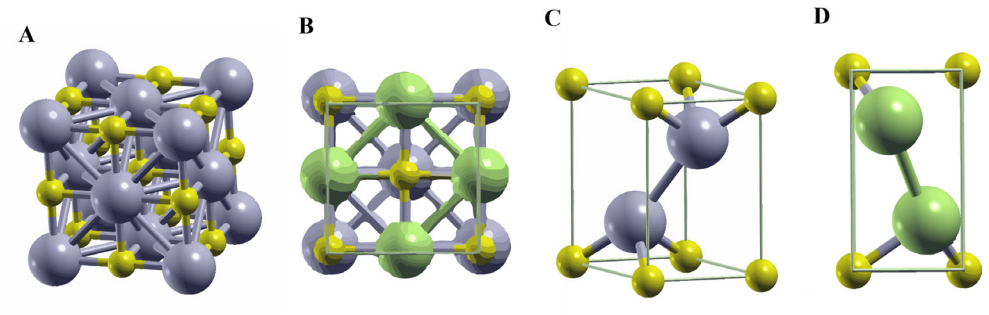

Figure 11. A) Unit cell of fcc structure; B) Atomic configuration for (001) plane of fcc structure; C) Unit cell of hcp structure and D) Atomic configuration for (100) plane of hcp structure. Blue atoms are Mo, yellow atoms are C and green atoms are exposed Mo.

Table 3 contains the lattice parameters (a, b and c) and site densities for cubic α-MoC_{1-x} and hexagonal β-Mo_2C based on literature data [47]. The α-MoC_{1-x} catalyst has a site density of 0.1096 Mo atoms $Å^{-2}$ and β-Mo_2C has a site density of 0.1402 Mo atoms $Å^{-2}$. Although higher site density is usually linked to better catalytic performance for several reactions [17, 48], we observed that the catalyst with the lowest site density (α-MoC_{1-x}/CNF) provided faster hydrodeoxygenation (on a weight basis) than the catalyst with the higher site density (β-Mo_2C/CNF). We suggest that the lower site density of α-MoC_{1-x}/CNF resulted in more space around the Mo atoms in the α-MoC_{1-x} phase, making the Mo atoms more accessible for the large reactant molecule in our experiments (stearic acid).

Table 3. Lattice parameters and site density of bulk cubic (fcc) α-MoC_{1-x} and the hexagonal (hcp) β-Mo_2C based on literature data [47].

	Lattice parameters			Site density (Mo atoms $Å^{-1}$)
	a/pm	b/pm	c/pm	
α-MoC_{1-x}	––	437.3*	––	0.1096
β-Mo_2C	––	582.7*	283.8*	0.1402

*ref [47]

4. Conclusions

In our experiments, we first created 7.5 wt% molybdenum carbide catalysts on carbon nanofiber supports. Carbothermal reduction synthesis in an inert atmosphere resulted in hexagonal β-Mo_2C/CNF, while TPR synthesis in a 20% CH_4/H_2 atmosphere yielded cubic α-MoC_{1-x}/CNF. When we increased Mo loading from 7.5 to 20 wt% and performed TPR in the same CH_4/H_2 atmosphere, hexagonal β-Mo_2C/CNF formed. We conclude that the proportion of carbon/molybdenum available during synthesis appears to influence which crystalline phase forms.

Furthermore, although both catalysts displayed similar intrinsic activities (a TOF of 3 s^{-1} and 1 s^{-1} for α-MoC_{1-x}/CNF and β-Mo_2C/CNF, respectively), the 7.5 wt% α-MoC_{1-x}/CNF catalyst had a better weight-based catalytic performance than 7.5 wt% β-Mo_2C/CNF. We attribute this difference in catalytic performance to the difference in the crystal structure and suggest that the lower site density makes the Mo atoms more accessible for large reactant molecules.

To confirm this hypothesis, further experiments should be performed applying reactants with different carbon chain size (e.g. C3 to C20 carboxylic acids) and using 7.5 wt% α-MoC_{1-x}/CNF and 7.5 wt% β-Mo_2C/CNF as catalysts. In that way, we will be able to identify the role of site density in reactions with small and large reactant molecules.

References

[1] S. T. Oyama in *Handbook of Heterogeneous Catalysis* (Eds.: G. Ertl, H. Knözinger, F. Schüth, J. Weitkamp), Wiley-VCH, Weinheim, 2008, pp. 342 – 256.
[2] R. B. Levy, M. Boudart, Science 181 (1973) 547 – 549.
[3] S. T. Oyama, Catal. Today 15 (1992), 179 – 200.
[4] Z. Lin, W. Wan, S. Yao, J. G. Chen, Appl. Catal. B 233 (2018) 160 – 166.
[5] M. Grilc, G. Veryasov, B. Likozar, A. Jesih, J. Levec, Appl. Catal. B 163 (2015) 467 – 477.
[6] K. Xiong, W.-S. Lee, A. Bhan, J. G. Chen, ChemSusChem 7 (2014) 2146 – 2151.
[7] Y.-B. Huang, M.-Y. Chen, L. Yan, Q.-X. Guo, Y. Fu, ChemSusChem 7 (2014) 1068 – 1070.
[8] H. Ren, W. Yu, M. Salciccioli, Y. Chen, Y. Huang, K. Xiong, D. G. Vlachos, J. G. Chen, ChemSusChem 6 (2013) 798 – 801.
[9] J. A. Schaidle, J. Blackburn, C. A. Farberow, C. Nash, K. X. Steirer, J. Clark, D. J. Robichaud, D. A. Ruddy, ACS Catal. 6 (2016) 1181 – 1197.
[10] L. A. Sousa, J. L. Zotin, V. Teixeira da Silva, Appl. Catal. A 449 (2012) 105−111.
[11] R. W. Gosselink, D. R Stellwagen, J. H. Bitter, Angew. Chem. Int. Ed. 52 (2013) 5089 – 5092.
[12] D. R. Stellwagen, J. H. Bitter, Green Chem. 17 (2015) 582 – 593.
[13] E. F. Mai, M. A. Machado, T. E. Davies, J. A. L.-Sanchez, V. Teixeira da Silva, Green Chem. 16 (2014) 4092 – 4097.
[14] B. Dhandapani, T. St. Clair, S. T. Oyama, Appl. Catal. A 168 (1998) 219 – 228.
[15] C. Li, M. Zheng, A. Wang, T. Zhang, Energy Environ. Sci. 5 (2012) 6383 – 6390.
[16] J. B. Claridge, A. P. E. York, A. J. Brungs, C. M.-Alvarez, J. Sloan, S. C. Tsang, M. L. H. Green, J. Catal. 180 (1998) 85 – 100.
[17] J.-S. Choi, G. Bugli, G. D.-Mariadassou, J. Catal. 193 (2000) 238 – 247.
[18] T.-cun Xiao, A. P. E. York, V. C. Williams, H. A.-Megren, A.Hanif, X.-ya Zhou, M. L. H. Green, Chem. Mater. 12 (2000) 3896 – 3905.
[19] X. Li, D. Ma, L.Chen, X. Bao, Catal. Lett. 116 (2007) 63 – 69.
[20] W. Gruner, S. Stolle, K. Wetzig, Int. J. Ref. Mater. Hard Mater. 18 (2000) 137 – 145.
[21] A. L. Jongerius, R. W. Gosselink, J. Dijkstra, J. H. Bitter, P. C. A. Bruijnincx, B. M. Weckhuysen, ChemCatChem 5 (2013) 2964 – 2972.
[22] Y. Qin, L. He, J. Duan, P. Chen, H. Lou, X. Zheng, H. Hong, ChemCatChem 6 (2014) 2698 – 2705.
[23] E. Puello-Polo, J. L. Brito, J. Mol. Catal. A: Chem. 281 (2008) 85 – 92.
[24] Kh. V. Manukyan, A. R. Zurnachyan, S. L. Kharatyan, R. A. Mnatsakanyan, Int. J. Self-Propag. High-Temp. Synth. 20 (2011) 1 – 5.
[25] C. L. Roe, K. H. Schulz, Stud. Surf. Sci. Catal. 127 (1999) 121 – 128.
[26] H. H. Hwu, J. G. Chen, Chem. Rev. 105 (2005) 185 – 212.
[27] M. M. Sullivan, A. Bhan, J. Catal. 344 (2016) 53 – 58.
[28] Z. Li, C. Chen, E. Zhan, N. Ta, Y. Li, W. Shen, Chem. Commun. 50 (2014) 4469 – 4471.
[29] B. Frank, K. Friedel, F. Girgsdies, X. Huang, R. Schlögl, A. Trunschke, ChemCatChem 5 (2013) 2296 – 2305.
[30] G. Vitale, H. Guzmán, M. L. Frauwallner, C. E. Scott, P. P.-Almao, Catal. Today 250 (2015) 123 – 133.
[31] K.-Z. Qi, G.-C. Wang, W.-J. Zheng, Surf. Sci. 614 (2013) 53 – 63.
[32] A. Lofberg, A. Frennet, G. Leclercq, L. Leclercq, J. M. Giraudon, J. Catal. 189 (2000) 170 – 183.
[33] J. Zou, M. Xiang, B. Hou, D. Wu, Y. Sun, J. Nat. Gas Chem. 20 (2011) 271 – 280.
[34] J. Gao, Y. Wu, C. Jia, Z. Zhong, F. Gao, Y. Yang, B. Liu, Catal. Commun. 84 (2016) 147 – 150.
[35] T. Matsuda, Y. Hirata, H. Itoh, H. Sakagami, N. Takahashi, Micropor Mesopor Mat 42 (2001) 337 – 344.
[36] ICDD PDF-2 database package http://www.icdd.com/products/pdf2.htm, accessed on DATE.
[37] C. H. L. Tempelman, E. J. M. Hensen, Appl. Catal. B 176 – 177 (2015) 731 – 739.
[38] K. O. Sebakhy, G. Vitale, A. Hassan, P. Pereira-Almao, Catal. Lett. 148 (2018) 904 – 923.
[39] J. H. Bitter, J. Mater. Chem. 20 (2010) 7312 – 7321.
[40] W.-S. Lee, A. Kumar, Z. Wang, A. Bhan, ACS Catal. 5 (2015) 4104 – 4114.

[41] H. Wang, S. Liu, K. J. Smith, Energy Fuels 30 (2016) 6039 – 6049.
[42] W.-S. Lee, Z. Wang, R. J. Wu, A. Bhan, J. Catal. 319 (2014) 44 – 53.
[43] T. P. St. Clair, S. T. Oyama, D. F. Cox, Surf. Sci. 468 (2000) 62 – 76.
[44] M. Nagai, H. Tominaga, S. Omi, Langmuir 16 (2000) 10215 – 10220.
[45] X. -R. Shi, J. Wang, K. Hermann, J. Phys. Chem. C 114 (2010) 13630 – 13641.
[46] J. Han, J. Duan, P. Chen, H. Lou, X. Zheng, Adv. Synth. Catal. 353 (2011) 2577 – 2583.
[47] J. R. dos S. Politi, F. Viñes, J. A. Rodriguez, F. Illas, Phys. Chem. Phys. 15 (2013) 12617 – 12625.
[48] K. R. McCrea, J. W. Logan, T. L. Tarbuck, J. L. Heiser, M. E. Bussel, J. Catal. 171 (1997) 255 – 267.

Chapter 6

Particle size effects in nickel phosphide supported on activated carbon as catalyst for stearic acid deoxygenation

Co-authors of this chapter are M. A. S. Baldanza, V. Teixeira da Silva and H. Bitter (manuscript in preparation).

Abstract

We evaluated the influence of particle size of Ni_2P supported on activated carbon on activity and product distribution during stearic acid hydrodeoxygenation at 350 °C and 30 bar H_2. Catalysts with loadings of 10, 20 and 30 wt% Ni_2P were synthesized by incipient wetness impregnation leading to average particle sizes of around 8, 12 and greater than 30 nm, respectively. The particle size had no influence on intrinsic catalytic activity (turn over frequency), but did influence product distribution. Heptadecane was the main final product over all catalysts at higher conversions, but the pathway of heptadecane formation depended on catalyst particle size. At conversion levels below 10%, oxygenates (octadecanal and/or octadecanol) formed over 10 wt% Ni_2P/AC, while heptadecane and/or heptadecene were the major products over 20 and 30 wt% Ni_2P/AC. These results indicate that heptadecane formed by partial hydrogenation of stearic acid followed by decarbonylation of aldehyde over small phosphide particles (8 nm), while it formed by direct stearic acid decarbonylation/decarboxylation over larger phosphide particles (12 and > 30 nm). We suggest that the difference in product distribution (hence pathway) over different catalyst particle sizes is related to differences in the concentrations of Ni(1) and Ni(2) sites in the catalysts.

1. Introduction

Transition metal phosphides are potential catalysts for deoxygenation reactions as their high activity and stability are comparable to those of noble metal and sulfide catalysts [1 – 3]. Ni_2P is the most extensively studied transition metal phosphide in hydrodeoxygenation reactions [4 – 6]. Among various Co, Fe, W and Ni phosphides supported on silica, Ni_2P presented the best catalytic performance for the deoxygenation of methyl laurate at 300 ˚C and 2 MPa [4]. This reveals that the nature of the phosphide plays a fundamental role in the activity in deoxygenation reactions.

Chen *et al.* [4] have shown that the nature of the phosphide also influences the pathway of the deoxygenation reaction. For example, while Ni_2P, Co_2P and Fe_2P-FeP favor the decarboxylation pathway, MoP and WP favor the hydrodeoxygenation pathway, which is attributed to the difference in electron density of the catalysts' metal sites. Besides the nature of the phosphide itself, various physical chemistry properties may also influence activity and selectivity in deoxygenation reactions, such as the nature of the support [7, 8] and the catalyst's particle size [9, 10].

Over the years, several studies have suggested that particle size directly affects the electronic structure and/or geometry of the active phase [9 – 13]. In several reactions, catalytic performance is influenced by particle size [9], although other reactions have revealed themselves as structure-insensitive [14].

Although sensitivity to structure usually is related to particles smaller than 5 nm, several researchers have observed particle size effects with larger particles (up to 25 nm) [9, 15 – 19]. For example, da Silva *et al.* [19] studied the influence of the particle size of cobalt supported on carbon nanofibers on ethanol steam reforming, by using catalysts with particle sizes ranging from 2.6 to 16 nm, and observed that catalytic activity increases with decreasing particle size. Fang *et al.* [15] used Ni/CNT catalysts with particle sizes from 9 to 16 nm on guaiacol hydrodeoxygenation and observed that catalytic activity increases with the decrease of metal particle size.

As reported in the literature, particle size influences the activity for CO hydrogenation [20] as well as for reactions involving either C – C bond breaking or formation [21]. Therefore, studying the effect of the particle size of nickel phosphide catalysts on the activity or selectivity for deoxygenation reactions is important because breaking C – C and/or C – O bonds is crucial in this type of reaction. Although deoxygenation of fatty acids has gained attention in recent years because of their potential to be converted into long-chain, diesel-like hydrocarbons, the effect of the catalyst's particle size on these reactions has not been properly studied yet, to our knowledge [22].

Depending on the feed, the nature of the support, the reaction conditions

and especially the catalyst, deoxygenation reactions are either dependent on the catalyst's particle size or not. For example, the hydrodeoxygenation of 4-methylphenol carried out at 350 ˚C and 4 MPa of H_2 over a MoP catalyst is considered particle-size-independent [23] while the hydrodeoxygenation of phenol (275 ˚C and 10 MPa) [9] and of guaiacol (300 ˚C and 3 MPa) [15] with Ni/SiO_2 and Ni-Fe/CNT as catalysts, respectively, are particle-size-dependent. Thus, without a sufficient number of studies using many different catalysts, it is difficult to assess if a specific reaction is particle-size-dependent or not.

The few studies dealing with the effects of particle size, active phase loading or dispersion in deoxygenation reaction mainly used noble or transition metals as catalysts [9, 10, 15, 25, 24 – 26]. Only a few researchers evaluated these effects with transition metal phosphide catalysts in their studies of deoxygenation [17, 23]. Whiffen *et al.* [23], for instance, investigated the influence of the particle size of MoP on the hydrodeoxygenation of 4-methylphenol at 350 ˚C and 4.4 MPa of H_2 and concluded that both the initial turnover frequency (TOF) and the ratio of hydrogenation to direct deoxygenation of 4-methylphenol were independent of MoP particle size. On the other hand, Zhang *et al.* [17] evaluated the influence of the particle size of nickel phosphides (Ni_3P, $Ni_{12}P_5$ and Ni_2P) on a γ-Al_2O_3 support in the deoxygenation of methyl laurate at 300 – 340 ˚C and 3 MPa H_2 and concluded that the TOF was influenced by the nickel phosphide phase, catalyst acidity and also the phosphide's particle size.

In the present paper, we report on a study of the influence of particle size on the activity and selectivity in the hydrodeoxygenation reaction of stearic acid, in which we varied the loading (10, 20 and 30 wt%) of nickel phosphide supported on activated carbon (Ni_2P/AC).

2. Experimental

Catalyst synthesis

Ni_2P/AC with different loadings (10, 20 and 30 wt%) were synthesized by incipient wetness impregnation as previously described in the literature [27]. Briefly, the appropriate amounts of $Ni(NO_3)_2.6H_2O$ (Sigma-Aldrich, 99.999% trace metals basis) and $(NH_4)_2HPO_4$ (Sigma-Aldrich, ACS reagent, ≥98%) solutions were mixed and HNO_3 (VWR Chemicals, 68%) was added to the final solution to dissolve the formed precipitate. Due to the fact that the volume of the final solution was higher than that of the activated carbon support (AC – Sigma-Aldrich Norit®), multiple impregnations had to be done, with intermediate drying steps at 120 ˚C for 1 hour. After the entire solution was incorporated into the support, the samples were calcined under argon flow at 500 ˚C for 6 hours (heating rate of 10 ˚C min^{-1}). Catalysts were

synthesized by temperature-programmed reduction (TPR) with pure hydrogen at a heating rate of 1 ˚C min^{-1} from 25 ˚C to 650 ˚C as described elsewhere [27].

Catalyst characterizations

X-ray diffraction (XRD) was performed with a D2 Phaser diffractometer from Bruker with K_α radiation of cobalt (CoK_α). The diffractograms were obtained with a continuous variation of the Bragg angle between 10˚ and 90˚, with steps of 1˚ min^{-1} and counting at 2 s $step^{-1}$. We identified the crystalline phase with the aid of the Powder Diffraction File, a database of X-ray powder diffraction patterns maintained by the International Center for Diffraction Data. This database is part of the JADE 5.0 software.

Nitrogen physisorption was used to assess the textural properties of the samples. Nitrogen adsorption/desorption isotherms were recorded at liquid nitrogen temperature by using a Micromeritics TriStar. Before analysis, samples were pre-treated under a vacuum at 400 ˚C for 20 h.

CO chemisorption was used to estimate the available number of active sites, and to calculate the turnover frequency values. CO-pulsed chemisorption measurements were performed using custom-made multipurpose equipment by pulsing calibrated volumes of a 5% (v/v) CO/He gas mixture over the catalyst reduced in situ, as previously described in the literature [27]. Prior to the analysis, the samples (0.1 g) were pretreated with 50 mL min^{-1} helium at 500 ˚C for 30 min followed by in situ activation by TPR (100 mL min^{-1} H_2). After reduction, samples were cooled down to 30 ˚C and flushed with He (50 mL min^{-1}) for 30 min. Mass spectrometry (Pfeiffer Vacuum, model D-35614 Asslar) was used to assess the CO uptake.

We calculated the TOF by using the following equation:

$$TOF(s^{-1}) = \frac{-r_A}{co_{uptake}}, -r_A = \frac{N_{A0} \times {dx_A}/{dt}}{W}$$

in which $-r_A$ is the initial reaction rate (mmol g^{-1} s^{-1}), N_{A0} is the initial amount of stearic acid (mmol), ${dx_A}/{dt}$ is the derivative of stearic acid conversion at time zero (s^{-1}) and W is the amount of catalyst (g).

Temperature-programmed desorption (TPD) of CO was carried out after CO chemisorption. Samples were heated from 20 ˚C to 1000 ˚C under He flow (100 mL min^{-1} and β = 15 ˚C min^{-1}) and the signal of ion m/z = 28 was followed in the mass spectrometer.

Transmission electron microscopy (TEM) was performed in a JEOL JEM2100 transmission electron microscope operated at 200 kV to analyze particle size and size distribution. We dusted the samples onto a 200-mesh copper grid covered with

a pure carbon film and removed any excess. We took images (4k x 4k) with a Gatan US4000 camera and calculated average particle sizes with ImageJ software, on the basis of 250 to 350 particles.

Stearic acid hydrodeoxygenation

Hydrodeoxygenation (HDO) reactions were performed in a 100-mL stainless steel Parr autoclave reactor (4590 Micro Bench Top Reactors). The reactor was filled with 2 g of stearic acid (Sigma-Aldrich, ≥ 95%, FCC, FG), 1 g of tetradecane (internal standard, Sigma-Aldrich, ≥ 99%), 0.25 g of catalyst and 50 mL of dodecane as solvent (Sigma-Aldrich, ReagentPlus ®, ≥ 99%). After purging with argon, stirring at 800 rpm was started and the reactor was heated to 350 ˚C. At this temperature, the total pressure was 10 bar. Subsequently, 30 bar H_2 was added to the system, resulting in a final pressure of 40 bar. Samples of 1 mL were taken during the 6-hour reaction after 0, 20, 40, 60, 120, 180, 240, 300 and 360 minutes.

Gas chromatography (GC) was used to analyze the reaction mixture (Shimadzu 2014, equipped with CP-FFAP column and photoionization detector). We used the following column temperature program: 50 ˚C for 1 minute, heating to 170 ˚C (β=7 ˚C min^{-1}), dwell time 1 minute, ramp to 240 ˚C (β=4 ˚C min^{-1}), dwell time 15 minutes. Prior to GC, we diluted the samples in CH_3Cl:MeOH (2:1 v/v). Trimethylsulphonium hydroxide (Sigma-Aldrich, ~ 0.25 M in methanol, for GC derivatization) was added to methylate free acids. The injected volume was 1μL for all analyses.

3. Results and discussion

Catalyst characterizations

Figure 1 shows the XRD diffractograms for 10, 20 and 30 wt% Ni_2P/AC catalysts. For all samples, it is possible to identify the characteristic diffractions of the Ni_2P phase (PDF#03-0953) located at 2θ values of 47.8, 52.3, 55.5, 63.9, 64.8, 78.7 and 86.9˚, indicated by squares. As in other work [18, 27 – 30], our TPR experiments (Figure C1, Appendix C) revealed the presence of a water formation peak between 300 ˚C and 550 ˚C, which is in accordance with pure Ni_2P formation.

Nitrogen physisorption was performed to obtain information about the catalysts' textural properties. Figure 2 shows the isotherms of pure AC and 10, 20 and 30 wt% Ni_2P/AC catalysts. All samples present a combination of type I and IV isotherms with H4 type hysteresis. For low P/P_0 values, the isotherms are typically type I which is characteristic for microporous solids. For higher values of P/P_0, the isotherms present characteristics of type IV isotherm represented by a hysteresis loop, what is associated with capillary condensation in a mesoporous material. The

hysteresis loop is of an H4 type indicating the presence of narrow slit-like pores [31]. Thus, Ni_2P/AC catalysts with different loading have a combination of micropores and mesopores with a narrow slit-like shape, which is also the case for the pure AC support.

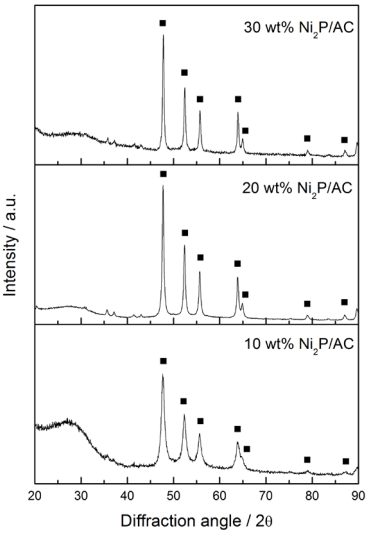

Figure 1. X-ray diffractograms of 10, 20 and 30 wt% Ni_2P/AC.

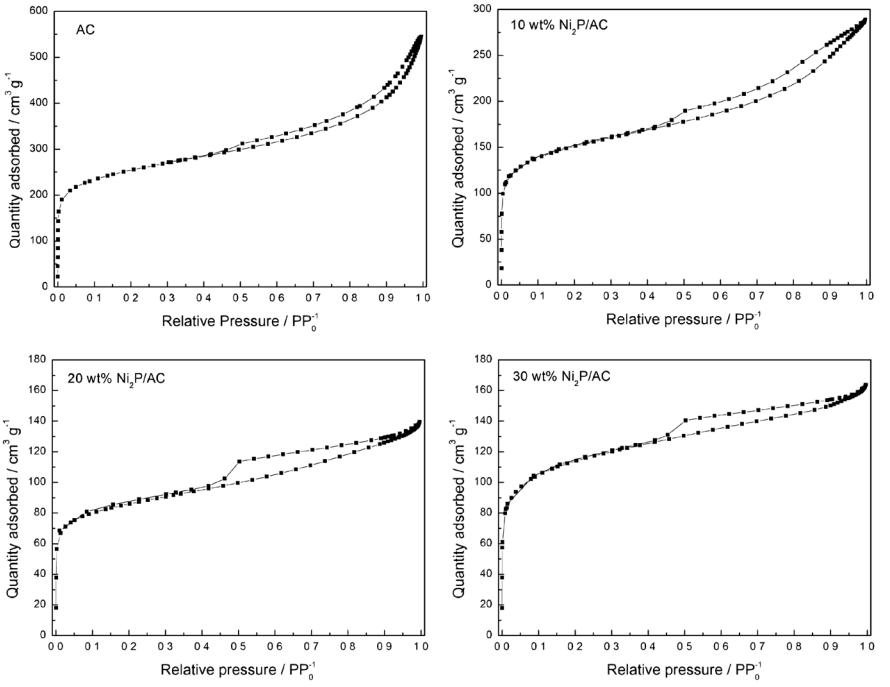

Figure 2. Isotherms of pure AC and 10, 20 and 30 wt% Ni_2P/AC.

Table 1 lists some of the textural properties of the support (AC) and the 10, 20 and 30 wt% Ni_2P/AC catalysts. The pure support had a specific surface area of 823 $m^2\ g^{-1}$. When nickel phosphide was incorporated to the support, the specific surface area decreased which was most likely due to the partial blockage of the pores of the support by the phosphide. Surprisingly, the specific surface area of the 30 wt% Ni_2P/AC (388 $m^2\ g^{-1}$) catalyst was higher than the specific surface area of the 20 wt% Ni_2P/AC (291 $m^2\ g^{-1}$). This can be explained when the total pore volume of these two catalysts are analyzed. 20 wt% Ni_2P/AC and 30 wt% Ni_2P/AC had the same total pore volume (0.2 $m^3\ g^{-1}$), which is not surprisingly lower than that of the pure support (0.5 $m^3\ g^{-1}$) and of the 10 wt% Ni_2P/AC (0.4 $m^3\ g^{-1}$). The higher specific surface area of 30 wt% Ni_2P relative to 20 wt% Ni_2P in combination with the similar pore volume suggests that part of the 30 wt% phosphide was not in contact with the support but rather had formed isolated Ni_2P particles.

Table 1. Textural properties of pure AC support and of the 10, 20 and 30 wt% Ni_2P/AC catalysts.

	Specific surface area	**Total pore volume**	**Average pore size**
	($m^2\ g^{-1}$)	**($m^3\ g^{-1}$)**	**(nm)**
AC	823	0.5	8.7
10 wt% Ni_2P/AC	493	0.4	6.0
20 wt% Ni_2P/AC	291	0.2	4.4
30 wt% Ni_2P/AC	388	0.2	4.1

To determine particle size, all samples were analyzed by TEM. Figure 3 presents representative TEM images of the 10, 20 and 30 wt% Ni_2P/AC catalysts, in which the black spots indicated by arrows are the active phase and the grey blurry areas are the support. The 10, 20 and 30 wt% Ni_2P/AC catalysts had an average particle size of 8 nm (s = 4 nm), 12 nm (s = 6 nm) and greater than 30 nm, respectively (Table 2). While the Ni_2P particles were small and well-dispersed over the support for the 10% Ni_2P/AC, the catalyst particle size increased and consequently the dispersion decreased for the 20 wt% and 30 wt% Ni_2P/AC. It is likely that some Ni_2P particles formed outside the pores of the support which is in line with the explanation of the total pore volume of samples 20 wt% and 30 wt% Ni_2P/AC. Note that in the TEM image of 30 wt% Ni_2P/AC, it is difficult to differentiate between AC-supported nickel phosphide particles and Ni_2P particles that were not in contact with the support. Nevertheless, the TEM images enable us to confirm that

the particles of 30 wt% Ni_2P/AC were much larger than the particles of the 10 and 20 wt% Ni_2P/AC catalysts.

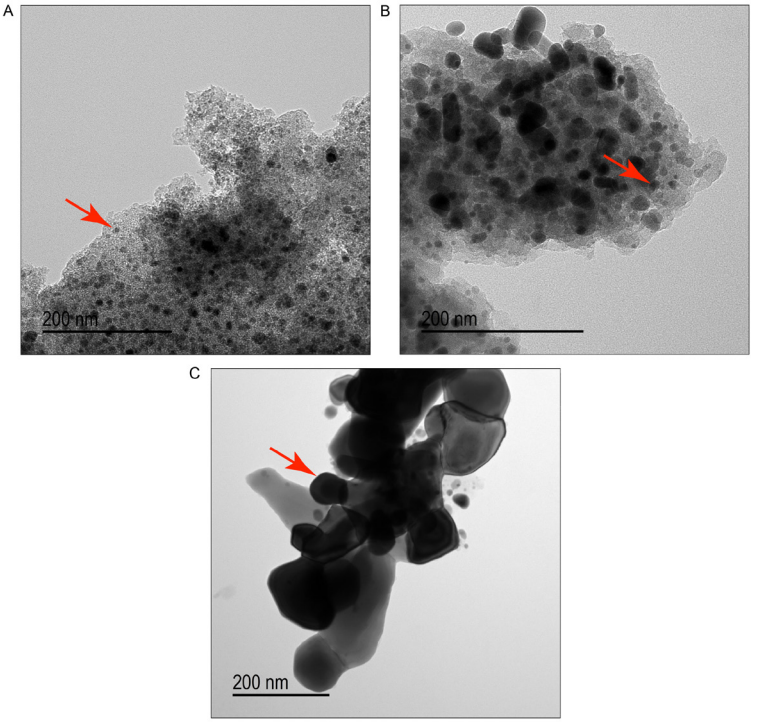

Figure 3. TEM images of A) 10 wt% Ni_2P/AC B) 20 wt% Ni_2P/AC and C) 30 wt% Ni_2P/AC; black spots indicated by arrows are the active phase and the grey blurry areas are the activated carbon support.

Table 2. Average particle size calculated from TEM analysis for the 10, 20 and 30 wt% Ni_2P/AC catalysts.

	10 wt% Ni_2P/AC	**20 wt% Ni_2P/AC**	**30 wt% Ni_2P/AC**
Average particle size	8 nm	12 nm	> 30 nm
Standard deviation	4 nm	6 nm	-

Figure 4 shows the particle size distribution for the 10, 20 and 30 wt% Ni_2P/AC catalysts. The presence of few large particles on the 10 and 20 wt% Ni_2P /AC catalysts and few smaller particles on 30 wt% Ni_2P/AC explains the high standard deviation for all samples.

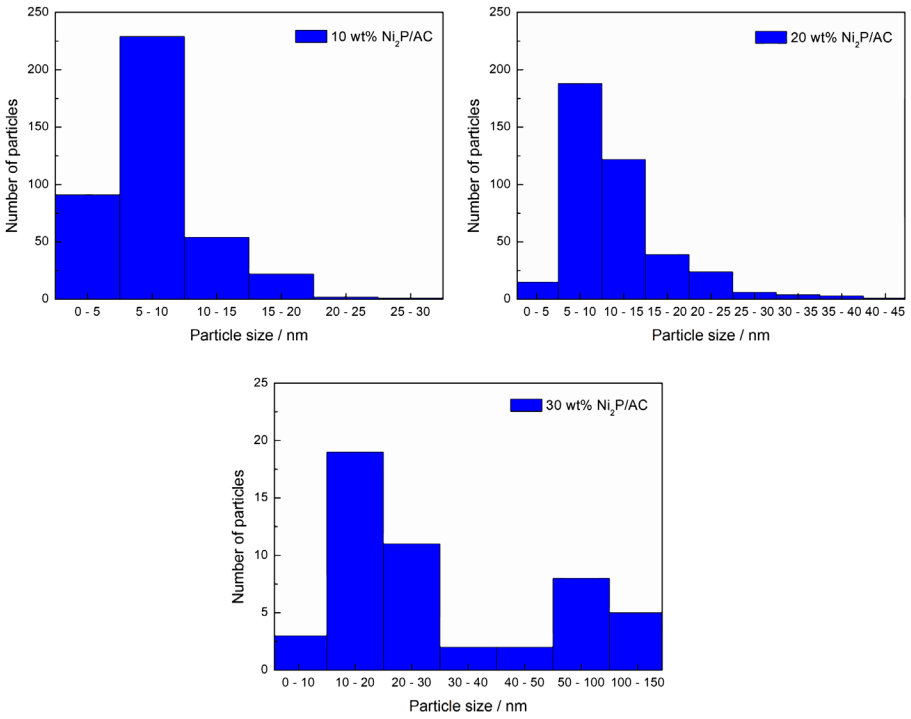

Figure 4. Particle size distribution of 10, 20 and 30 wt% Ni_2P/AC.

Stearic acid HDO

The catalysts were tested in stearic acid HDO at 350 ˚C and 30 bar H_2 for 6 hours. Figure 5 displays the kinetic curves for the 10, 20 and 30 wt% Ni_2P/AC catalysts. The activity (per weight of catalyst) increased in the order 30 wt% Ni_2P/AC > 20 wt% Ni_2P/AC > 10 wt% Ni_2P/AC.

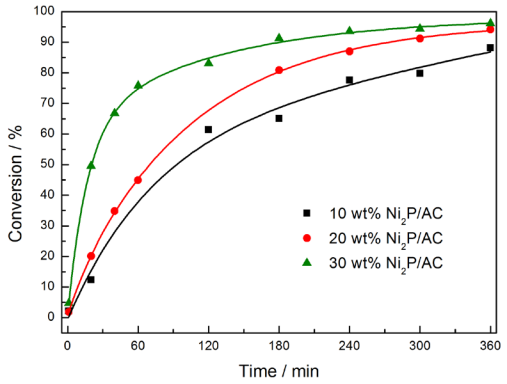

Figure 5. Conversion over time for 10, 20 and 30 wt% Ni_2P/AC catalysts in stearic acid HDO at 350 ˚C and 30 bar H_2, 2g stearic acid, 50 mL dodecane and 0.25 g catalyst.

To obtain information on the potential active sites on the catalysts, CO chemisorption and TPD were performed. Table 3 presents the CO chemisorption uptake values, the initial specific reaction rates and the TOF for the 10, 20 and 30 wt% Ni_2P/AC catalysts. Independent of the nickel phosphide loading, the CO uptake values were practically the same, varying between 8 and 12 μmol g^{-1}. The initial specific reaction rates of 10, 20 and 30 wt% Ni_2P/AC are 1117, 1477 and 3175 mmol g^{-1} h^{-1}, which translates in TOF values of 4.0 x 10^1, 4.7 x 10^1 and 7.5 x 10^1 s^{-1}, respectively. Though these TOF values are different, they are in the same order of magnitude. In other words, all catalysts demonstrated similar intrinsic activities despite the differences in particle size.

Table 3. CO uptake, initial specific reaction rate and TOF of the 10, 20 and 30 wt% Ni_2P/AC catalysts for stearic acid HDO at 350 °C and 30 bar H_2.

	CO uptake (μmol g^{-1})	**Initial specific reaction rate (mmol g^{-1} h^{-1})**	**TOF (s^{-1})**
10 wt% Ni_2P/AC	8	1117	4.0 x 10^1
20 wt% Ni_2P/AC	9	1477	4.7 x 10^1
30 wt% Ni_2P/AC	12	3175	7.5 x 10^1

Since there is no significant difference in the TOF values, we conclude that the higher conversion of 30 wt% Ni_2P/AC catalyst was due to the higher loading of the active phase and that the catalyst's particle size had no influence on catalytic activity for stearic acid HDO. Whiffen *et al.* [23] obtained a similar result, namely that MoP with different particle sizes had the same TOF for hydrodeoxygenation of 4-methylphenol, and the authors concluded that the reaction was structure-insensitive.

While CO chemisorption (Table 3) provides information on the concentration of the catalysts' potential active sites, CO TPD (Figure 6) informs about the nature of these sites. Although the CO TPD profiles for all samples is noisy due to the low CO uptake values, we observed subtle differences which can be translated into variations of the nature of the predominant active sites in the catalysts. Although the CO TPD profile of 10 wt% Ni_2P/AC presented a peak with a maximum at 146 °C, the CO TPD profiles of both 20 and 30 wt% Ni_2P/AC catalysts presented peaks with the maximum located at lower temperatures, namely around 107 to 110 °C.

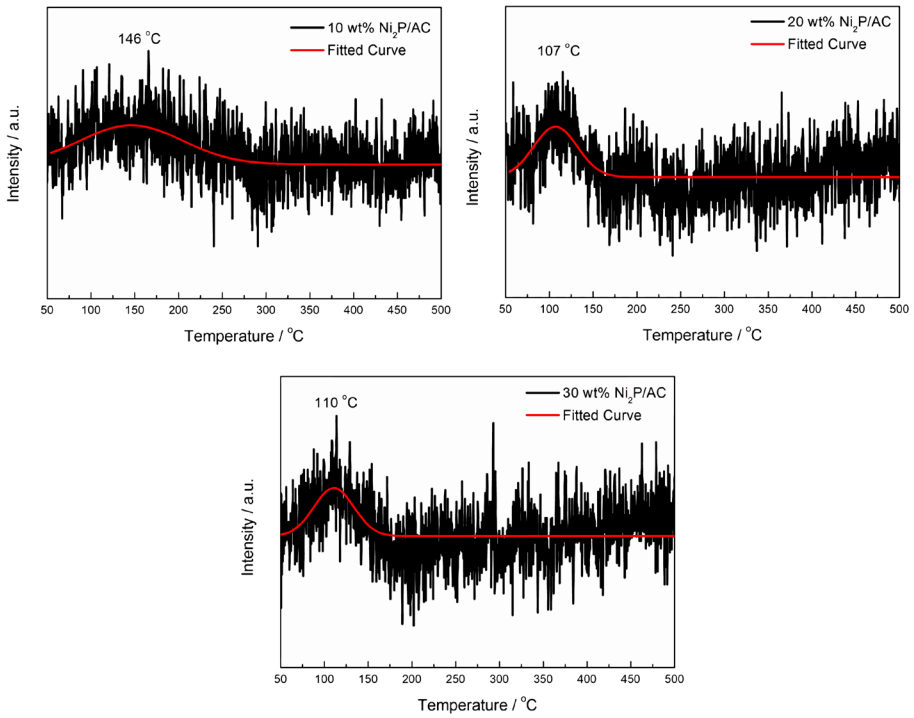

Figure 6. CO TPD profiles for the 10, 20 and 30 wt% Ni_2P/AC catalysts.

It is known that Ni_2P adopts a hexagonal structure, in which Ni atoms form two types of 9-fold arrangements around each P atom [32 – 34]. As shown in Figure 7, the Ni(1) site is quasi-tetrahedral surrounded by 4 nearest-neighbor P atoms and 8 second-nearest neighbor Ni atoms, while the Ni(2) site is square pyramidal surrounded by 5 nearest-neighbor P atoms and 6 next nearest-neighbor Ni atoms [18]. According to Feitosa *et al.* [27], the peak with the maximum at about 107 ˚C is related to Ni(1) sites and the maximum at 146 ˚C is related to Ni(2) sites. Thus, the CO TPD results indicate that 10 wt% Ni_2P/AC had predominantly Ni(2) sites and 20 and 30 wt% Ni_2P/AC had predominantly Ni(1) sites.

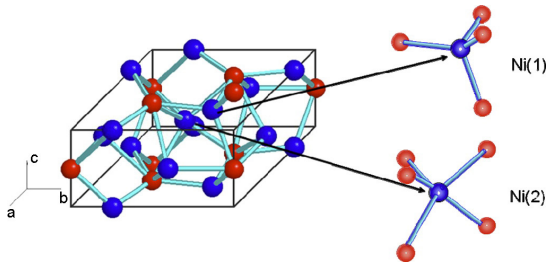

Figure 7. Ni(1) and Ni(2) sites in Ni_2P [18].

To investigate the influence of nickel phosphide particle size (*i.e.*, active phase loading) on product selectivity in stearic acid HDO, we analyzed the product distribution at various conversion values for all catalysts (Figure 8). All samples produced heptadecene and/or oxygenates (octadecanol and octadecanal) as intermediates and heptadecane and octadecane as final products. At high conversion values (> 75%), heptadecane and octadecane represented 80% and 20% of the products for all catalysts. However, at low conversions (< 10%), we observed different product distributions over catalysts with different particle sizes. Over 10 wt% Ni_2P/AC, oxygenates were the major products (about 60 to 70%), followed by heptadecane (around 30%). Over 20 and 30 wt% Ni_2P/AC, on the other hand, C17 (heptadecane and heptadecene) were the main products, followed by oxygenates.

Note that over the 10 wt% Ni_2P/AC catalyst, oxygenates were converted into both C17 and octadecane products while over the 20 and 30 wt% Ni_2P/AC catalysts, oxygenates were fully converted into octadecane.

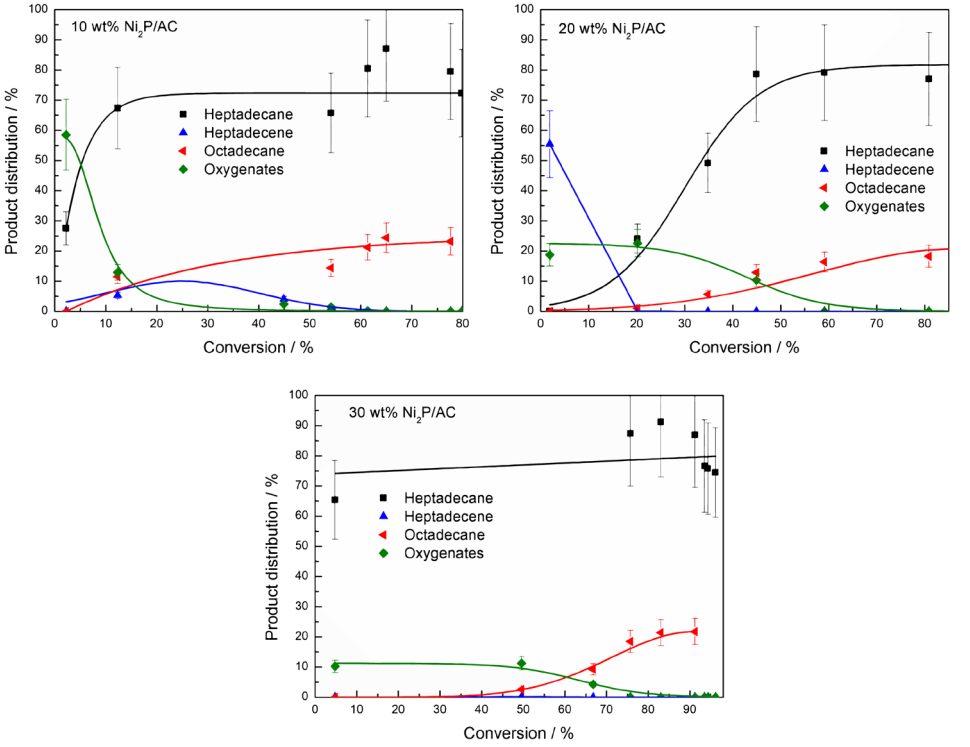

Figure 8. Product distribution as a function of conversion for stearic acid HDO at 350 ˚C and 30 bar H_2 over the 10, 20 and 30 wt% Ni_2P/AC catalysts.

Deoxygenation of stearic acid proceeds mainly by two possible routes, namely decarbonylation/decarboxylation (DCO) or hydrodeoxygenation (HDO),

as shown in Figure 9 [35, 36]. In the DCO route, the C – C bond of carboxyl/carbonyl group is broken to form C17 hydrocarbons, while two different pathways are possible in the HDO route. In the first pathway, the C – O bond is hydrogenated twice to form first an aldehyde and then an alcohol. Subsequently, the alcohol is dehydrated to form C18 hydrocarbons, which we call the HDO route in this paper. In the second pathway, the C – O bond is hydrogenated once to form an aldehyde, which is decarbonylated to form C17 hydrocarbons, and we call this the HDCO route in this paper.

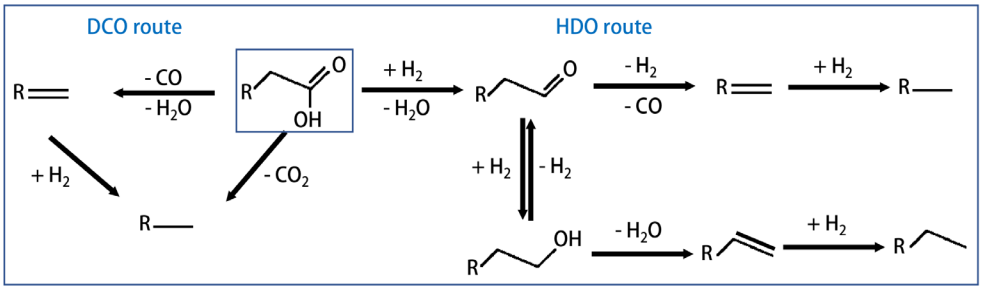

Figure 9. Scheme of possible reaction pathways for stearic acid hydrodeoxygenation over nickel phosphide catalysts, adapted from [35, 36].

Although the phosphide particle size had no influence on catalytic activity in our study, the results presented in Figure 8 suggest that particle size did influence product selectivity. Over small Ni_2P/AC particles, the HDCO route was favored since we observed oxygenates as the main products, at low conversion rates and heptadecane as the main product at high conversion rates. We attributed this to the higher number of Ni(2) sites on small particles. In nickel phosphides, the Ni sites bear small positive charges (δ^+) due to the charge transfer from nickel to phosphorus [37].

In recent work, Oyama *et al.* [18] synthesized supported Ni_2P with different particle sizes (3.8 to 10.1 nm) and used EXAFS and elemental analysis to study the type of sites and the amount of P in the catalysts. The elemental analysis results showed that catalysts with smaller particle sizes contained higher amounts of P in the structure. EXAFS results, in turn, revealed that catalysts with smaller particle sizes have more Ni(2) sites, which means that nickel has a more electrophilic character in smaller crystallites than in the larger particles' N(1) sites.

According to Yang *et al.* [16] and Zhang *et al.* [17], the electron density on a metal site plays an important role in selectivity during HDO reactions. A lower electron density (higher positive charge) increases the electrophilicity and therefore enhances the interaction with the free electron pairs of oxygen in the C – O bond. As

a consequence, the C – O bond weakens and dissociates resulting in a transformation through the HDO (or HDCO) route. On the other hand, a higher electron density on a metal site (smaller positive charge) is associated with less interaction between metal site and C – O bond, resulting in a preference for the DCO route.

When the information about the structure of supported Ni_2P and the relationship between a metal site's electronic density with product distribution in HDO is combined, we can positively conclude that smaller particles have more Ni(2) sites, which are more electrophilic. Consequently, catalysts with a smaller particle size favor the HDCO route, thus explaining the higher amount of oxygenates for the 10 wt% Ni_2P/AC catalyst at low conversions (< 10%). On the other hand, the HDO (or HDCO) route is less favored over bigger particles (20 and 30 wt% Ni_2P/AC) because they have predominantly Ni(1) sites on their structure, which are less electrophilic than Ni(2) sites. Therefore, instead of oxygenates, products with 17 carbon atoms are predominant over 20 and 30 wt% Ni_2P/AC catalysts even at low conversions.

Since we observed that smaller Ni_2P/AC particles favored the HDO route, controlling the Ni_2P/AC particle size during synthesis might be a promising strategy to control the predominant reaction pathway of stearic acid HDO.

4. Conclusions

In our study, Ni_2P/AC particle size had no influence on the intrinsic catalytic activity for stearic acid hydrodeoxygenation at 350 ˚C and 30 bar H_2 but it did influence product selectivity. Although both heptadecane and octadecane were the final products for all catalysts, the reaction pathway whereby heptadecane is formed differed for catalysts with different particle sizes. The HDCO route was favored over small Ni_2P/AC particles due to the higher concentration of Ni(2) sites in those catalysts, facilitating interaction with the C – O bond and its dissociation, producing oxygenates as the first intermediate. In contrast, the DCO route was favored over larger Ni_2P/AC particles due to the lower concentration of Ni(2) sites in those catalysts. Our findings suggest that controlling Ni_2P/AC particle size is a potential strategy to control the reaction pathway during stearic acid deoxygenation.

References

[1] V.M. Whiffen, K.J. Smith, Energy Fuels 24 (2010) 4728–4737.
[2] H.Y. Zhao, D. Li, P. Bui, S.T. Oyama, Appl. Catal. A 391 (2011) 305–310.
[3] R.H. Bowker, M.C. Smith, M.L. Pease, K.M. Slenkamp, L. Kovarik, M.E. Bussell, ACS Catal. 1 (2011) 917–922.
[4] J. Chen, H. Shi, L. Li, K. Li, Appl. Catal. B 144 (2014) 870–884.
[5] M. Peroni, G. Mancino, E. Baráth, O.Y. Gutiérrez, J.A. Lercher, Appl. Catal. B 180 (2016) 301–311.
[6] T.I. Korányi, Z. Vít, D.G. Poduval, R. Ryoo, H.S. Kim, E.J.M. Hensen, J. Catal. 253 (2008) 119–131.
[7] J.P. Ford, J.G. Immer, H.H. Lamb, Top. Catal. 55 (2012) 175–184.
[8] D. Kubicka, J. Horácek, M. Setnicka, R. Bulánek, A. Zukal, I. Kubicková, Appl. Catal. B 145 (2014) 101–107.
[9] P.M. Mortensen, J.-D. Grunwaldt, P.A. Jensen, A.D. Jensen, Catal. Today 259 (2016) 277–284.
[10] Y.K. Lugo-José, J.R. Monnier, A. Heyden, C.T. Williams, Catal. Sci. Technol. 4 (2014) 3909–3916.
[11] H. Zhang, M. Jin, Y. Xiong, B. Lim, Y. Xia, Acc. Chem. Res. 46 (2013) 1783–1794.
[12] M.S. Chen, D.W. Goodman, Catal. Today 111 (2006) 22–33.
[13] G.A. Somorjal, J. Carrazza, Ind. Eng. Chem. Fundam. 25 (1986) 63–69.
[14] M. Boudart, Chem. Rev. 95 (1995) 661–666.
[15] H. Fang, J. Zheng, X. Luo, J. Du, A. Roldan, S. Leoni, Y. Yuan, Appl. Catal. A 529 (2017) 20–31.
[16] Y. Yang, J. Chen, H. Shi, Energy Fuels 27 (2013) 3400–3409.
[17] Z. Zhang, M. Tang, J. Chen, Appl. Surf. Sci. 360 (2016) 353–364.
[18] S.T. Oyama, Y.-K. Lee, J. Catal. 258 (2008) 393–400.
[19] A.L.M. da Silva, J.P. Den Breejen, L.V. Mattos, J.H. Bitter, K.P. De Jong, F.B. Noronha, J. Catal. 318 (2014) 67–74.
[20] L. Guczi, Z. Schay, K. Matusek, I. Bogyay, Appl. Catal. 22 (1986) 289–309.
[21] K.J. Klabunde, Y.X. Li, A. Khaleel, in: G.C. Hadjipanayis, R.W. Siegel (Eds.), Nanophase Materials, Kluwer Academic Publishers, Dordrecht, 1994, pp. 757–769.
[22] I. Simakova, O. Simakova, P. Mäki-Arvela, A. Simakov, M. Estrada, D.Y. Murzin, Appl. Catal. A 355 (2009) 100–108.
[23] V.M.L. Whiffen, K.J. Smith, S.K. Straus, Appl. Catal. A 419 – 420 (2012) 111–125.
[24] R. Olcese, M.M. Bettahar, B. Malaman, J. Ghanbaja, L. Tibavizco, D. Petitjean, A. Dufour, Appl. Catal. B 129 (2013) 528–538.
[25] C. Newman, X. Zhou, B. Goundie, I.T. Ghampson, R.A. Pollock, Z. Ross, M.C. Wheeler, R.W. Meulenberg, R.N. Austin, B.G. Frederick, Appl. Catal. A 477 (2014) 64–74.
[26] I.T. Ghampson, C. Sepúlveda, R. García, J.L.G. Fierro, N. Escalona, Catal. Sci. Technol. 6 (2016) 4356–4369.
[27] L.F. Feitosa, G. Berhault, D. Laurenti, T.E. Davies, V. Teixeira da Silva, J. Catal. 340 (2016) 154–165.
[28] S.T. Oyama, X. Wang, Y.-K. Lee, K. Bando, F.G. Requejo, J. Catal. 210 (2002) 207–217.
[29] S.T. Oyama, X. Wang, Y.-K. Lee, W.-J. Chun, J. Catal. 221 (2004) 263–273.
[30] X. Wang, P. Clark, S.T. Oyama, J. Catal. 208 (2002) 321–331.
[31] K.S.W. Sing, D.H. Everett, R.A.W. Haul, L. Moscou, R.A. Pierotti, J. Rouquérol, T. Siemieniewska, Pure & Appl. Chem. 57 (1985) 603–619.

[32] Y.K. Lee, S.T. Oyama, J. Catal. 239(2) (2006) 376–389.
[33] S.T. Oyama, X. Wang, Y.-K. Lee, K. Bando, F.G. Requejo, J. Catal. 210 (2002) 207–217.
[34] S.T. Oyama, T. Gott, H. Zhao, Y.-K. Lee, Catal. Today 143 (2009) 94–107.
[35] R.W. Gosselink, D.R. Stellwagen, J.H. Bitter, Angew. Chem. Int. Ed. 52 (2013) 5089–5092.
[36] D.R. Stellwagen, J.H. Bitter, Green Chem. (2015), 17, 582–593.
[37] S.J. Sawhill, K.A. Layman, D.R. Van Wyk, M.H. Engelhard, C. Wang, M.E. Bussell, J. Catal. 231 (2005) 300–313.

Chapter 7

On the role of different noble metals in the synthesis of nickel phosphides and their use in thiophene hydrodesulfurization

Co-authors of this chapter are C. B. Rodella, G. S. A. Jorge, V. Teixeira da Silva and H. Bitter (manuscript in preparation)

Abstract

Adding small amounts (1 wt. %) of noble metals (palladium, rhodium and platinum) to a nickel phosphate catalyst precursor ($Ni_xP_yO_z/SiO_2$) resulted in a lowering of the synthesis temperature of nickel phosphide (Ni_2P/SiO_2) catalysts via phosphate reduction. Temperature-programmed reduction (TPR) showed that, for all three noble metals studied, the synthesis temperature decreased from 803 to 643 K, which is attributed to hydrogen activation and spillover. Additional TPR experiments using different bed configurations ($Ni_xP_yO_z/SiO_2$ on top of PdO/SiO_2, PdO/SiO_2 on top of $Ni_xP_yO_z/SiO_2$ or a physical mixture of $Ni_xP_yO_z/SiO_2$ and PdO/SiO_2) indicated that the noble metal has to be in close contact with the nickel phosphate to achieve a decrease in the synthesis temperature. The prepared catalysts were tested with hydrodesulphurization of thiophene at 593 K and 1 atm. Samples impregnated with noble metals (NM-Ni_2P/SiO_2) were 2 to 3 times more active than the non-promoted Ni_2P/SiO_2 sample. Low energy ion scattering revealed that the noble metal was not present on the surface of the catalyst and this observation led to the conclusion that the observed activity enhancement was associated with changes in the Ni-phosphide phase itself. It is important to notice that X-ray photoelectron spectroscopy did show some noble metal in the catalyst sub-surface. However, since the selectivity over all catalysts was the same irrespective of the addition of a noble metal, the noble metals did not appear to participate in the reaction.

1. Introduction

Transition metal phosphides are potential catalysts for hydrotreatment reactions [1 – 9]. Fang *et al.* [8] and Oyama [9] have shown that metal phosphides can have similar or even higher activities for hydrodesulphurization (HDS) and hydrodenitrogenation (HDN) reactions relative to commercial metal sulphide catalysts (NiMo and CoMo).

Of the studied bulk and silica-supported transition metal phosphides (Fe_2P, Ni_2P, CoP, MoP, WP), Ni_2P showed the highest intrinsic activity for simultaneous dibenzothiophene HDS and quinoline HDN at 3.1 MPa and 643 K [10, 11]. These promising results induced many follow-up studies focusing on the Ni/P ratio [12], comparison between bulk and supported Ni_2P [10], influence of the nature of support [13] and influence of the weight-loading of the active phase [14, 15] on a series of hydrotreatment processes. However, although nickel phosphide is a promising catalyst, its high synthesis temperature (around 923 K) is still an issue and lowering it would be beneficial.

Several synthesis methods for the preparation of nickel phosphide exist, such as organometallic synthesis and reduction of phosphine or (hypo)phosphite. However, reduction of phosphates to phosphides is the most used method [16]. During nickel phosphide synthesis via reduction of phosphates, the precursor (metal oxide + ammonium phosphate, metal salt + ammonium phosphate, or metal phosphate) is transformed into phosphide under hydrogen flow at high temperature [16], as Scheme 1 shows.

$$[Ni(NO_3)_2.6H_2O + (NH_4)_2HPO_4]/Support \xrightarrow[\text{calc } 773\text{ K}]{\text{dry}} [NiO + P_2O_5]/Support \xrightarrow{\text{TPR}} Ni_2P/Support$$

Scheme 1. Preparation of supported nickel phosphide via temperature-programmed reduction of a supported oxidic precursor prepared from nickel nitrate and ammonium phosphate with drying (393 K) and calcination (at 773 K) steps. Adapted from [16].

According to Prins and Bussell [16], the P-O bond in the phosphate (P_2O_5) is very strong and needs high temperatures to be broken. It is well accepted [16] that when the first metal particles are formed from oxide reduction, they are capable of dissociating dihydrogen into atomic hydrogen (activation of hydrogen), which reduces the phosphorus of phosphate into phosphine. The formed phosphine reacts with the metal to produce metal phosphide. Scheme 2 illustrates this process.

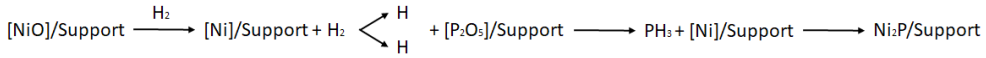

Scheme 2. Illustration of reduction mechanism during preparation of supported nickel phosphide via temperature-programmed reduction of a supported oxidic precursor prepared from nickel nitrate and ammonium phosphate.

Several studies have focused on methodologies to lower the Ni_2P synthesis temperature [17 – 23]. Teixeira da Silva *et al.* [18] proposed the incorporation of small amounts (0.1, 0.5 and 1 wt. %) of palladium oxide in the nickel phosphate to decrease the synthesis temperature of Ni_2P/SiO_2. The idea behind that proposal is that the noble metal (Pd) is able to promote hydrogen spillover [24] and that the palladium oxide is reduced at lower temperatures than the phosphate [18]. Thus, the formation of palladium metal at low temperature would activate hydrogen, facilitating nickel phosphate reduction by hydrogen spillover. The researchers showed that when 1% Pd is incorporated in nickel phosphate, the synthesis temperature of Ni_2P/SiO_2 can be reduced by 200 K. In the same work, the authors also evaluated the product distribution in HDS and observed that the butane selectivity of both non-promoted Ni_2P/SiO_2 and 1% Pd Ni_2P/SiO_2 was 2%, whereas it was 10% for 1% Pd/SiO_2. Based on these results, the authors suggested that palladium does not participate in the reaction and they speculated that during the reduction step, Pd is either covered by Ni_2P or migrates into the bulk of the phosphide [18].

The current paper expands on the idea of Teixeira da Silva *et al.* [18] by investigating how the addition of other noble metal oxides (Rh_2O_3 and PtO) to $Ni_xP_yO_z/SiO_2$ influences the Ni_2P/SiO_2 synthesis temperature.

2. Experimental

2.1 Synthesis of precursors

Hereafter, we will refer to the phosphate obtained after the calcination step as 'precursor'. Thus, the precursors of bulk Ni_2P, Ni_2P/SiO_2, Rh-Ni_2P/SiO_2, Pd-Ni_2P/SiO_2 and Pt-Ni_2P/SiO_2 are $Ni_xP_yO_z$, $Ni_xP_yO_z/SiO_2$, Rh_2O_3-$Ni_xP_yO_z/SiO_2$, PdO-$Ni_xP_yO_z/SiO_2$ and PtO-$Ni_xP_yO_z/SiO_2$, respectively.

Bulk $Ni_xP_yO_z$ was synthesized by mixing 7.13 g $(NH_4)_2HPO_4$ (Vetec Química Fina, 98%) in 20 mL water with a solution of 20.66 g $Ni(NO_3)_2.6H_2O$ (Vetec Química Fina, 97%) in 20 mL water, under agitation. This formed a light green precipitate. To that precipitate, 4.5 mL of HNO_3 (Vetec Química Fina, 65%) was added, which resulted in the dissolution of the precipitate. The final solution was put into a thermostatic bath at 363 K to evaporate the water. The obtained solid was dried under static air at 433 K for 12 hours followed by calcination step at 773 K in static air for 6 hours.

$Ni_xP_yO_z/SiO_2$ was synthesized via incipient wetness impregnation of a pre-prepared solution of Ni-nitrate and diammonium hydrogen phosphate to 4.9 g of the support (Silica Cab-O-Sil M-5, Cabot). This solution was prepared by mixing 3.04 g $(NH_4)_2HPO_4$ (Vetec Química Fina, 98%) in 9 mL water with a solution of 8.15 g $Ni(NO_3)_2.6H_2O$ (Vetec Química Fina, 97%) in 8 mL water under agitation. This formed a light green precipitate. To that precipitate, 2.9 mL of HNO_3 (Vetec Química Fina, 65%) was added, which resulted in the dissolution of the precipitate. The amounts of the reactants were calculated to produce 30 wt. % Ni_2P/SiO_2 with a molar Ni/P proportion of 2:1.6. Due to the fact that the volume of the final solution containing Ni and P was higher than the pore volume of the support, we carried out multiple impregnations, each time with an intermediate drying step at 393 K for 1 hour. After the final impregnation, the sample was calcined under static air at 773 K for 6 hours, yielding $Ni_xP_yO_z/SiO_2$.

PdO-$Ni_xP_yO_z/SiO_2$ was produced as follows. A palladium solution was prepared to be impregnated on $Ni_xP_yO_z/SiO_2$ as follows. 2.6 mL of HCl (Vetec Química Fina) was added to 0.0842 g of $PdCl_2$ (Sigma-Aldrich, 99,999%) and dried on a heating plate at 393 K two times (for the second time, 0.74 mL of HCl was added), followed by addition of 5 mL of deionized water and drying. Next, 8 mL of deionized water was added to the solid and the final solution was impregnated on the precursor $Ni_xP_yO_z/SiO_2$ (6.2 g) via incipient wetness impregnation. As the volume of the final solution containing Pd was higher than the pore volume of the support, we had to carry out multiple impregnations, with intermediate drying steps at 393 K for 1 hour. After the final impregnation, the sample was calcined under static air at 773 K for 2 hours, producing PdO-$Ni_xP_yO_z/SiO_2$.

Rh_2O_3-$Ni_xP_yO_z/SiO_2$ was created as follows. A rhodium solution was prepared via dissolution of 0.1027 g of $RhCl_3$ (Acros Organics) in 8 mL of deionized water. This solution was impregnated on $Ni_xP_yO_z/SiO_2$ via incipient wetness impregnation in the same way as described for palladium. The sample was calcined at 773 K for 2 hours, resulting in producing Rh_2O_3-$Ni_xP_yO_z/SiO_2$.

PtO-$Ni_xP_yO_z/SiO_2$ was produced as follows. A platinum solution was made via dissolution of 1 g of $H_2PtCl_6.6H_2O$ (Aldrich, 99,995%) in 25 mL of deionized water. After that, 8 mL of deionized water was added to 3.35 mL of the first solution. The final platinum solution was then impregnated on $Ni_xP_yO_z/SiO_2$ via incipient wetness impregnation in the same way as described in the previous paragraphs. As the volume of the final solution containing Pt was higher than the support pore volume, we had to carry out multiple impregnations, each with an intermediate drying step at 393 K for 1 hour. After the final impregnation, the sample was calcined under static air at 773 K for 2 hours, producing PtO-$Ni_xP_yO_z/SiO_2$.

In all cases, the amount of noble metal (NM) was such that 1 wt. % NM 30 wt. % Ni_2P/SiO_2 was obtained after the calcination step.

Precursor of 1 wt. % Pd_6P/SiO_2 ($Pd_xP_yO_z/SiO_2$) was synthesized via impregnation of a solution prepared by mixing 0.0113 g of $(NH_4)_2HPO_4$ in 4 mL of water with 4 mL of a solution containing 0.0834 g $PdCl_2$ prepared as previously described for the preparation of PdO-$Ni_xP_yO_z/SiO_2$ precursor. The resulting solution was impregnated on the silica support, and the sample was dried at 393 K for 1 hour between impregnations. After impregnation, the sample was calcined at 773 K for 4 hours. Note that this sample was synthesized only to prove that the Pd-P phase does not form during PdO-$Ni_xP_yO_z/SiO_2$ reduction via TPR.

2.2 Synthesis of catalysts

TPR was used to reduce the precursors to obtain the final phosphide catalysts. Before TPR, the samples (100 mg) were pre-treated under helium flow (50 mL min^{-1}) at 773 K (heating rate 10 K min^{-1}) for 30 minutes to remove water and other physisorbed species. After this step, the samples were cooled to room temperature and reheated to 1273 K under pure hydrogen flow (100 mL min^{-1}) at a heating rate of 1 K min^{-1}. The effluent gas was analyzed using an in-line mass spectrometer (Pfeiffer vacuum, model D-35614 Asslar). The water formation (m/z = 18) was measured to investigate the reduction process.

2.3 Characterizations

For ex-situ characterization (XRD and LEIS; see hereafter), the catalysts were passivated after their synthesis to avoid bulk oxidation. Passivation was done using a 0.5 % (v/v) O_2/N_2 gas mixture, which was fed through the reactor at room temperature (~298K) for 5 hours. When samples were characterized in situ (XPS and CO chemisorptions; see hereafter), the reactor temperature was decreased to 298 K before analysis.

X-ray diffraction (XRD) was performed with a Rigaku Miniflex diffractometer using CuK_a radiation and a nickel filter. The diffractograms were obtained by scanning over Bragg angles between 10° and 90°, with steps of 1° min^{-1} and a counting time of 2 s per step.

Low energy ion scattering (LEIS) was performed in a Qtac 100 instrument (IONTOF), with normal incidence of noble gas ions and ion scattering at angle 145°. The atomic oxygen treatment took place at room temperature and $1x10^{-5}$ mbar. We used a SPECS MPS-ECR source and an atomic oxygen flux of about $1x10^{15}$ atoms cm^{-2} s^{-1}.

X-ray photoelectron spectroscopy (XPS) was carried out using a SPECS,

model Phoibos 150 machine that uses a HSA 3500 power supply. Al Kα (1486.61 eV) radiation and a pass energy of 20 eV was used. Data was collected for 14 hours. After synthesis, catalysts were transferred without exposure to air into n-hexane, which had been degassed to avoid contamination with oxygen. Prior to analysis, samples were deposited on a carbon tape, dried under vacuum (10^{-9} mbar) at 298 K at the pre-chamber. After 48 hours at the pre-chamber, samples were transferred to the analysis chamber and XPS analysis was carried out under vacuum (pressure below 10^{-8} mbar).

The density of potential active sites of the catalysts was determined by pulse CO chemisorption. Known amounts of CO (2.4 mL of 20% (v/v) CO/He) were pulsed over the sample. The effluent was led into a mass spectrometer and the signal indicating CO (m/z = 28) was followed. The density of potential active sites (CO_{TOTAL} – mol g^{-1}) via CO chemisorption was calculated as follows:

$$CO_{TOTAL} = \frac{n_{CO_{Loop}}}{m} \times \sum_{i=1}^{N_{inj}} \left(1 - \frac{A_i}{A_{cte}}\right)$$

in which $n_{CO_{loop}}$ is the amount of CO in the loop (mol), m is the catalyst weight (g), N_{inj} is the number of pulse injections, A_i is the peak area "i" and A_{cte} is the average of constant area of peaks when saturation is achieved.

2.4 Catalytic bed configurations

To investigate the role of the noble metal in decreasing the nickel phosphide synthesis temperature, three bed configurations were prepared by using PdO/SiO_2 and $Ni_xP_yO_z/SiO_2$ samples. In all configurations, a downward H_2 flow was used. These configurations contained either a double bed in which $Ni_xP_yO_z/SiO_2$ was deposited above PdO/SiO_2 (Figure 1A) or PdO/SiO_2 over $Ni_xP_yO_z/SiO_2$ (Figure 1B) or a bed with a physical mixture of both materials (Figure 1C). In the configurations of Figures 1A and 1B, the reactor beds were separated by a thin quartz wool layer.

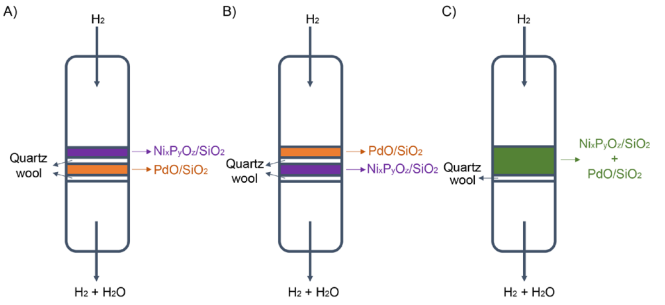

Figure 1. Schematic representation of reactor configurations used to study the role of noble metals on nickel phosphate reduction.

2.5 Catalytic evaluation

Prior to reaction, the catalysts (100 mg) were activated in situ via TPR under pure hydrogen flow (100 mL min^{-1}). While Ni_2P/SiO_2 was reduced at 923 K, as concluded from TPR, the samples containing noble metals were reduced at 723 K for 1 hour, and Pd_6P/SiO_2 was reduced at 773 K. In all cases, a heating rate of 1 K min^{-1} was used. After the reduction step, the samples were cooled to 593 K under He flow (100 mL min^{-1}). Next, the reactor was by-passed and hydrogen (30 mL min^{-1}) was fed through a saturator that was kept at 293 K and contained thiophene. The thiophene was saturated with hydrogen for 1 hour. After saturation, the total gas flow (hydrogen + thiophene) was adjusted to 30 mL min^{-1} and the feed composition (3.19% mol/mol C_4H_4S/H_2) was stabilized (1 hour). This mixture was led to the reactor and HDS was performed at 593 K for 50 hours. Samples were analyzed every 15 minutes using an in-line Shimadzu gas chromatograph (GC-2014).

Conversions were kept below 10% and the catalytic activity was expressed as turnover frequency (TOF) according to Equation (1) [25]:

$$TOF = \frac{F_{A0}}{W} \frac{X_A}{CO_{uptake}} \qquad \text{Equation (1)}$$

Here, F_{A0} is the molar rate of thiophene fed into the reactor (μmol s^{-1}), W is the catalyst weight (g), CO_{uptake} is the uptake of chemisorbed CO (μmol g^{-1}), and X_A is the thiophene conversion (%). Note that the reaction settings were chosen to obtain differential conditions and absence of mass transfer limitations (internal and external).

3. Results and discussion

3.1 Synthesis of catalysts

Figure 2 contains the TPR profiles of the precursors to Ni_2P/SiO_2 and NM-Ni_2P/SiO_2. The TPR profile of $Ni_xP_yO_z/SiO_2$ displays one peak at 802 K and the TPR profiles of NM-$Ni_xP_yO_z/SiO_2$ catalysts each show one peak between 633 and 640 K. Thus, most likely, phosphides formed from the phosphate precursor in one step, as claimed before [16]. Moreover, it is clear that adding 1 wt. % noble metal decreased the reduction temperature by about 160 K irrespective of the noble metal used. This suggests that hydrogen activation was enhanced over the noble metals and that in all materials, the rate-determining step was the same, most likely the activation of the P–O bond. These results can be explained by the hydrogen spillover mechanism [18, 24], i.e. hydrogen is activated (split into atomic hydrogen) at low temperature over the reduced noble metal and in a following step, facilitates the reduction of the phosphate.

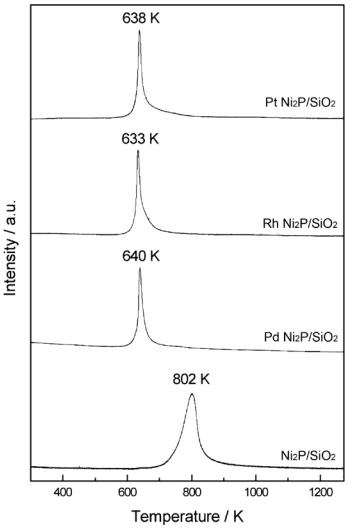

Figure 2. Water formation profiles during TPR of Ni_2P/SiO_2, Pd Ni_2P/SiO_2, Rh Ni_2P/SiO_2 and Pt Ni_2P/SiO_2.

To investigate to which extent close contact between the noble metal and phosphate is required for decreasing the reduction temperature of Ni_2P/SiO_2, we performed an experiment with three different bed configurations using $Ni_xP_yO_z/SiO_2$ on top of PdO/SiO_2, PdO/SiO_2 on top of $Ni_xP_yO_z/SiO_2$, and a mixture of $Ni_xP_yO_z/SiO_2$ and PdO/SiO_2 (Figure 1).

Figure 3 presents the TPR profiles of $Ni_xP_yO_z/SiO_2$ (or $PdO\text{-}Ni_xP_yO_z/SiO_2$) using the three different configurations. Figures 3A and 3B show the reduction profiles for the first two configurations, i.e. with $Ni_xP_yO_z/SiO_2$ on top and with PdO/SiO_2 on top. These reduction profiles are the same as for pure $Ni_xP_yO_z/SiO_2$ (Figure 2), i.e. the noble metal had no effect on the synthesis temperature of Ni_2P/SiO_2. On the other hand, when PdO/SiO_2 and $Ni_xP_yO_z/SiO_2$ were mixed (Figure 3C), the water formation profile presented two peaks with maxima at 681 K and 819 K indicating that when the noble metal is close to the phosphate phase, it facilitates phosphate reduction.

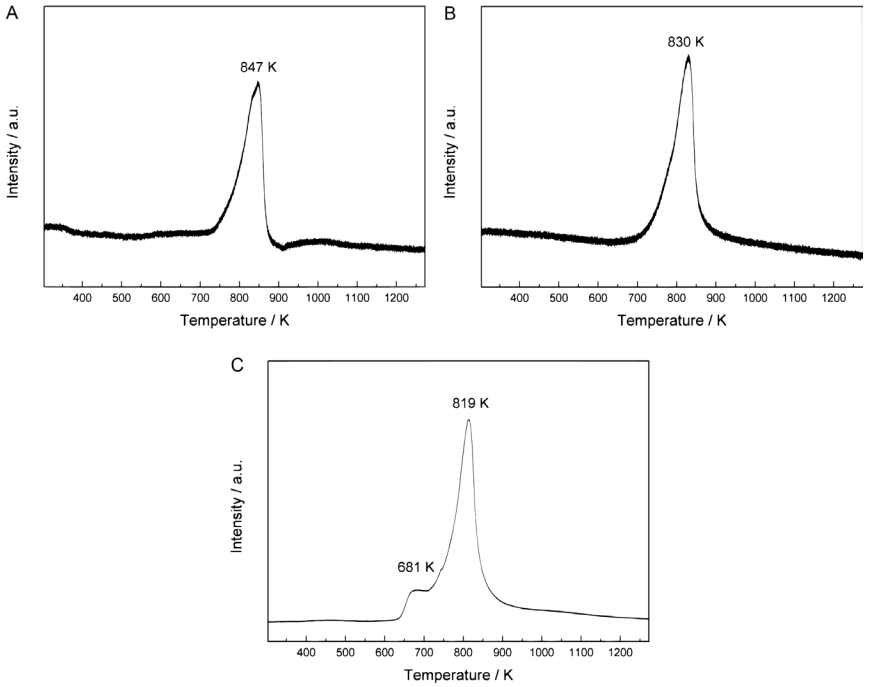

Figure 3. Water formation profiles during TPR of the samples in A) the configuration with $Ni_xP_yO_z/SiO_2$ on top of PdO/SiO_2, B) the configuration with PdO/SiO_2 on top of $Ni_xP_yO_z/SiO_2$ and C) the configuration containing a mixture of $Ni_xP_yO_z/SiO_2$ and PdO/SiO_2.

When comparing the TPR profiles of $PdO\text{-}Ni_xP_yO_z/SiO_2$ (Figure 2) and of the physical mixture of PdO/SiO_2 + $Ni_xP_yO_z/SiO_2$ (Figure 3C), it is clear that in the case of the physical mixture, the higher temperature reduction peak (819 K) is still present, i.e. this configuration was only partially successful. On the other hand, for the impregnated samples, only the low temperature reduction peak (640 K) is visible. Thus, the contact between the palladium and phosphate particles has to be close enough to enable the decrease of the synthesis temperature of Ni_2P/SiO_2 via hydrogen spillover, as shown in Scheme 3.

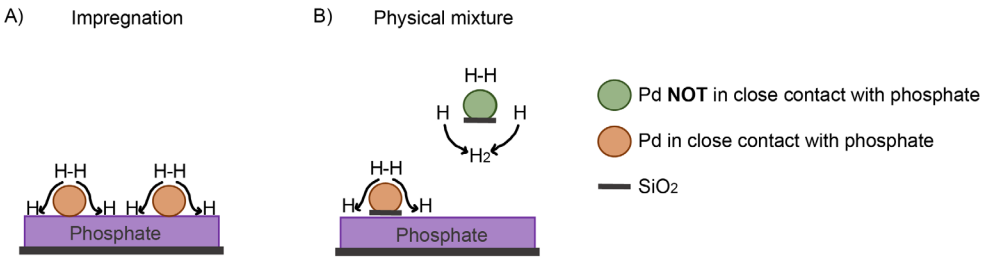

Scheme 3. Hydrogen spillover phenomena when a) PdO is impregnated on $Ni_xP_yO_z/SiO_2$ and b) PdO and $Ni_xP_yO_z/SiO_2$ are physically mixed.

Figure 4 displays the XRD diffractograms of Ni_2P/SiO_2 (after reduction of its precursor at 923 K) and NM-Ni_2P/SiO_2 (after reduction of its precursor at 723 K). All diffractograms show only peaks characteristic of the silica support (2θ = 22°) and of the Ni_2P phase (2θ = 40.8°, 44.8°, 47.6° and 54.4°; JCPDS no. 74-1385). This result reinforces the conclusion that the addition of small amounts of noble metal to Ni_2P/SiO_2 facilitated the reduction of the phosphate. When $Ni_xP_yO_z/SiO_2$ was reduced at 723 K, the Ni_2P phase did not form (Figure D1, Appendix D), which again is an indication that the noble metal facilitated the formation of the phosphide at lower temperatures.

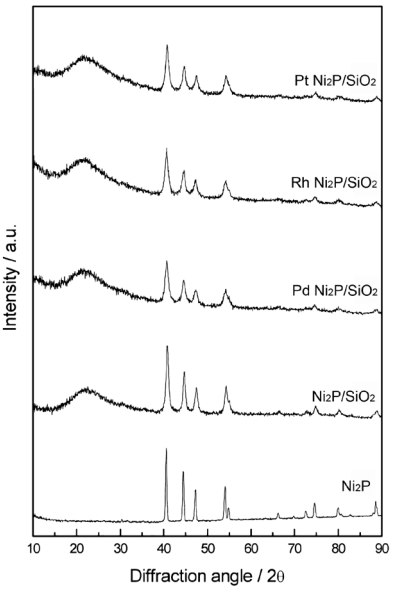

Figure 4. XRD diffractograms for Ni_2P, Ni_2P/SiO_2, Pd Ni_2P/SiO_2, Rh Ni_2P/SiO_2 and Pt Ni_2P/SiO_2.

To determine the density of potential active sites, we use pulse CO chemisorption. Table 1 shows the CO chemisorption uptakes of Ni_2P/SiO_2 and NM-Ni_2P/SiO_2. CO chemisorption uptake by Ni_2P/SiO_2 (47 μmol g_{cat}^{-1}) was higher than CO chemisorption uptake by Pd-Ni_2P/SiO_2, Rh-Ni_2P/SiO_2 and Pt-Ni_2P/SiO_2 (17, 18 and 16 μmol g_{cat}^{-1}, respectively), meaning that Ni_2P/SiO_2 had more sites accessible for CO than NM-Ni_2P/SiO_2.

Table 1. CO chemisorption uptake for Ni_2P/SiO_2, Pd Ni_2P/SiO_2, Rh Ni_2P/SiO_2 and Pt Ni_2P/SiO_2.

Sample	CO uptake (μmol g^{-1})
30% Ni_2P/SiO_2	47
1% Pd 30% Ni_2P/SiO_2	17
1% Rh 30% Ni_2P/SiO_2	18
1% Pt 30% Ni_2P/SiO_2	16

Teixeira da Silva *et al.* [18] have shown before, based on an XAS/XANES study, that even when TPR indicates that the reduction of a precursor appears to be completed at a given temperature, the samples may not be fully reduced. In analogy with that, we speculate that the higher CO uptake of the unpromoted sample was due to the higher Ni reduction degree of that sample.

3.2 Thiophene HDS

The Ni_2P/SiO_2 and NM-Ni_2P/SiO_2 catalysts were tested for thiophene HDS at 593 K and 1 atm for 50 hours. Figure 5 displays the intrinsic catalytic activity (TOF) of the catalysts over 50 hours of reaction. The TOF of Ni_2P/SiO_2 was around 2.5 times lower than the TOF of all NM-Ni_2P/SiO_2 catalysts. The difference in activity between non-promoted Ni_2P/SiO_2 and NM-Ni_2P/SiO_2 might be related to the ease with which the Ni_3PS phase, which is more active than Ni_2P, can be formed during reaction. During HDS reactions, phosphorus from Ni_2P is partially substituted by sulphur, resulting in the active Ni_3PS phase [12, 14, 26]. Some authors [15, 27] have shown that the incorporation of sulphur in the precursor ($Ni_xP_yO_z/SiO_2$) is easier than in the reduced phosphide (Ni_2P/SiO_2). Therefore, the formation of Ni_3PS was facilitated over the NM-Ni_2P/SiO_2 samples, which had a lower reduction degree than Ni_2P/SiO_2. Furthermore, all samples showed an increase in TOF in the first few hours of reaction and achieved a stable performance after 10 hours. This increase of the TOF value in the first hours of the reaction might be related to a restructuring of the samples by the incorporation of sulphur [15, 26, 28, 29]. According to Oyama *et al.* [12, 14], the phosphosulphide phase that forms via the incorporation of sulphur in the Ni_2P structure is the real active phase for HDS reactions. Nelson *et al.* [26] supported this hypothesis using density functional theory calculations.

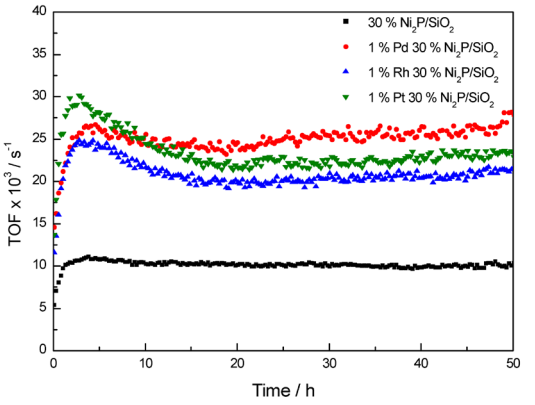

Figure 5. Catalytic activity of 30% Ni_2P/SiO_2 (■), 1% Pd 30% Ni_2P/SiO_2 (●), 1% Rh 30% Ni_2P/SiO_2 (▲) and 1% Pt 30% Ni_2P/SiO_2 (▼).

Figure 6 presents the product distributions for thiophene HDS over Ni_2P/SiO_2 and NM-Ni_2P/SiO_2. In general, the selectivity of the different catalysts was similar irrespective of the presence or absence of a noble metal. This indicates that the role of the noble metal during the reaction was insignificant and that the noble metal did not participate in the reaction. The fact that butane selectivity was very low (< 2%) suggests that Pd was not on the catalyst surface [28] and that no Pd_6P formed since those phases would have resulted in a greater butane selectivity, namely greater than 10% for Pd [28] as well as for Pd_6P (Figure 7).

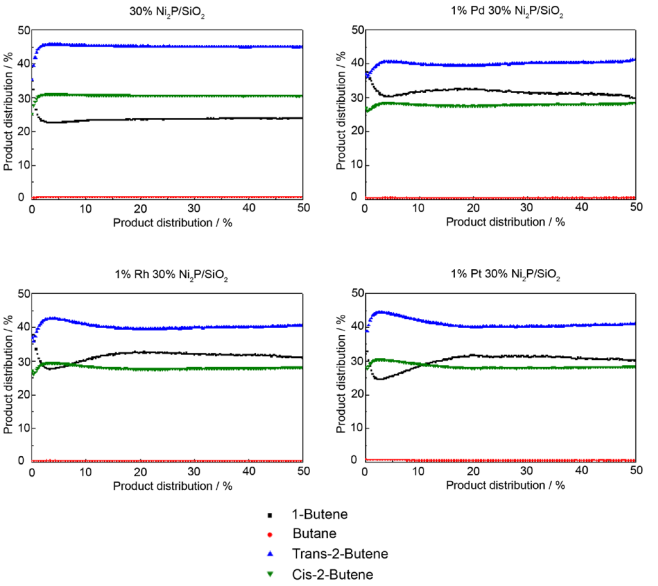

Figure 6. Selectivity for 30% Ni_2P/SiO_2, 1% Pd 30% Ni_2P/SiO_2, 1% Rh 30% Ni_2P/SiO_2 and 1% Pt 30% Ni_2P/SiO_2.

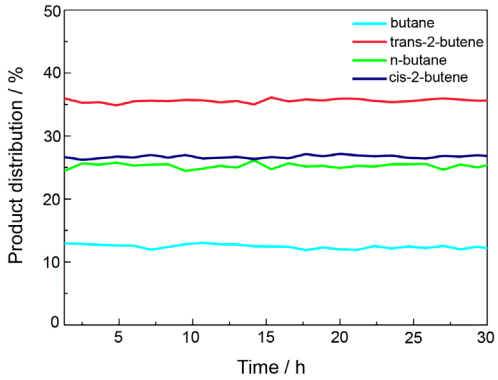

Figure 7. Product distribution for Pd_6P/SiO_2 in thiophene HDS at 593 K and 1 atm: Butane (light blue), 1-butene (green), trans-2-butene (red) and cis-2-butene (dark blue).

This 2% butane selectivity observed for NM-Ni_2P/SiO_2 catalysts raises the question about the location of the noble metal after the reduction process and during reaction. To investigate that, we carried out XPS and LEIS.

Figure 8A displays the XPS spectra and the peak deconvolutions of $Ni_xP_yO_z/SiO_2$ and of reduced Ni_2P/SiO_2. In the Ni 2p spectrum of $Ni_xP_yO_z/SiO_2$, nickel in the oxidic form (Ni^{2+}), presents peaks around 857, 862, 875 and 883 eV, characteristic for spin-orbit splitting related to Ni $2p_{3/2}$ and Ni $2p_{1/2}$ [30 – 32]. In the P 2p spectrum, in turn, oxidized phosphorus (P^{5+}) presents only one peak with a maximum at 133.3 eV [30].

For the reduced Ni_2P/SiO_2, in addition to the peaks related to oxidized nickel and phosphorus, the XPS spectrum for the Ni 2p region presents two new peaks at 853.1 and 870.2 eV, characteristic for nickel phosphide [31]. In the P 2p spectrum, a new peak is present at 129.5 eV, which is characteristic for the phosphorus in the nickel phosphide [32]. The presence of the peaks related to nickel and phosphorus oxides in the XPS spectra of Ni_2P/SiO_2 suggests that either catalyst reduction was not complete during synthesis or that the catalyst was partially oxidized during the protection process prior to XPS analysis.

Figures 8B, 8C and 8D display XPS spectra with deconvolution curves for precursor NM-$Ni_xP_yO_z/SiO_2$ and for reduced NM-Ni_2P/SiO_2. The XPS spectra in the Ni 2p and P 2p regions have already been discussed in the preceding paragraphs. In addition, all precursors and reduced samples display a similar XPS spectrum in the noble metal region (Pd 3d, Rh 3d and Pt 4d), suggesting that noble metal particles are located at the catalyst surface after reduction. However, since the product distribution results suggest that the noble metals did not participate in the HDS reaction, and it is known that XPS is able to identify compounds present in the upper

4 to 5 sub-layers of the catalyst, we conclude that after migration from the surface, the noble metals were located in the first sub-layers of the NM-Ni_2P/SiO_2 catalysts but not in the first layer.

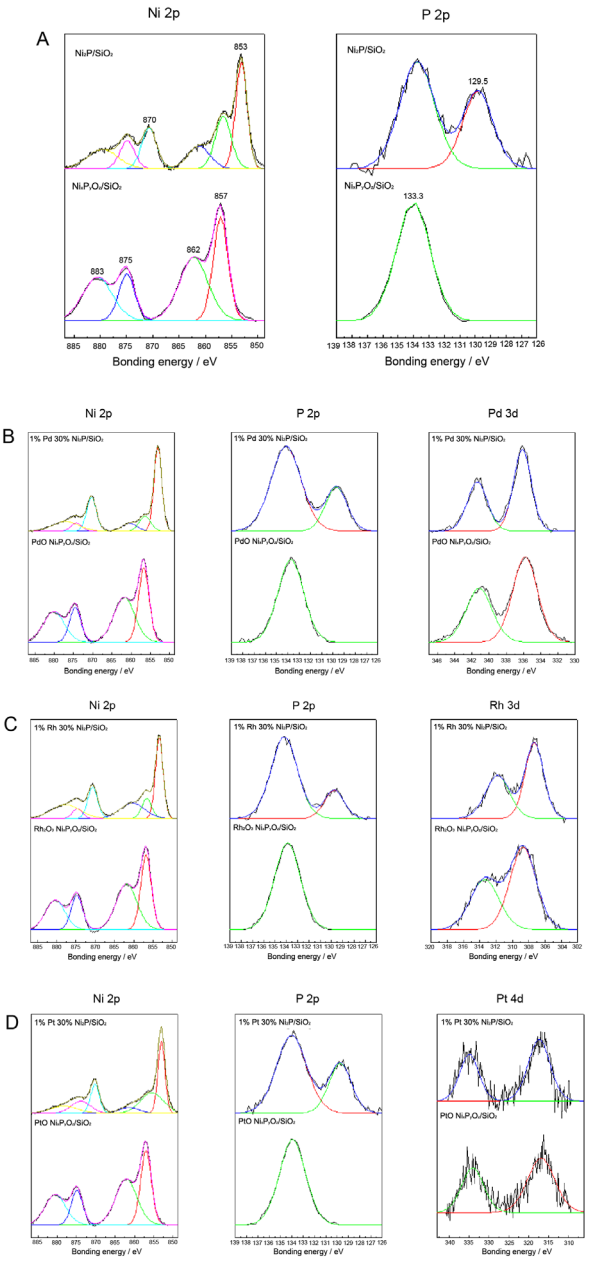

Figure 8. XPS spectra of A) Ni 2p and P 2p of 30% Ni_2P/SiO_2 (and $Ni_xP_yO_z/SiO_2$), B) Ni 2p, P 2p and Pd 3d of 1% Pd 30% Ni_2P/SiO_2 (and PdO $Ni_xP_yO_z/SiO_2$), C) Ni 2p, P 2p and Rh 3d of 1% Rh 30% Ni_2P/SiO_2 (and Rh_2O_3 $Ni_xP_yO_z/SiO_2$) and D) Ni 2p, P 2p and Pt 4d of 1% Pt 30% Ni_2P/SiO_2 (and PtO $Ni_xP_yO_z/SiO_2$).

To analyze the composition of the outermost layer of the nickel phosphide surface, we performed LEIS on the precursor and on reduced Pd-Ni_2P/SiO_2 (Figures 9 and 10).

Figure 9 shows that, while a peak related to palladium is visible for the precursor sample, it is absent for the reduced catalyst, indicating that palladium was not present in the outermost layer after reduction. This supports the suggestion that palladium is covered by Ni_2P or migrated into the catalyst bulk during Pd-Ni_2P/SiO_2 synthesis.

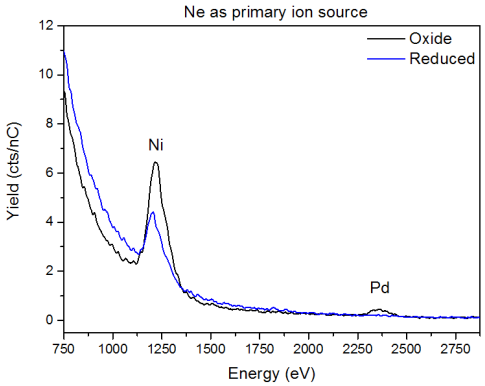

Figure 9. LEIS spectra of oxidized and reduced Pd-Ni_2P/SiO_2 using Ne as a primary ion source.

When the ion dose is increased during LEIS analysis, it is expected that more particles are released from the material. Figure 10 shows that, for Ni particles, the amount of ejected metal indeed increased for both precursor and reduced sample when we increased the He ion dose. Thus, we can conclude that Ni was present at the surface of Pd-Ni_2P/SiO_2. On the other hand, for Pd particles, the amount of ejected metal only increased for the precursor sample. For the reduced catalyst, the amount of ejected metal remained the same and close to zero even when the He ion dose was increased. This again confirms that palladium was not present at the surface of Pd-Ni_2P/SiO_2 and the combination of the LEIS and product distribution results suggests that the noble metals were indeed covered by nickel phosphide during the synthesis of NM-Ni_2P/SiO_2 catalyst and did not participate in the thiophene HDS reaction.

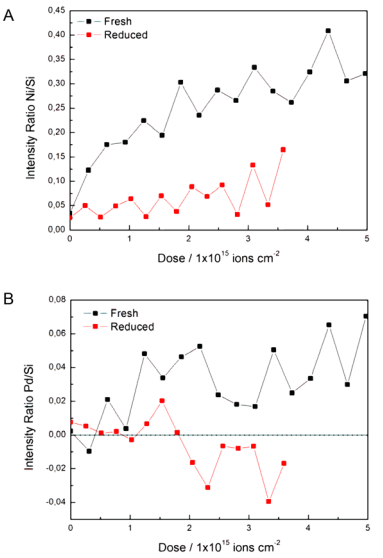

Figure 10. LEIS spectra of ratio of a) Ni/Si and b) Pd/Si versus dose of He ions for a fresh and reduced sample of Pd-Ni_2P/SiO_2.

4. Conclusions

When small amounts of noble metals (1 wt. % Pd, Rh and Pt) were added to $Ni_xP_yO_z/SiO_2$ via incipient wetness impregnation, this caused a decrease of 160 K in nickel phosphide's synthesis temperature. The most likely mechanism behind this is spillover of hydrogen atoms formed on the noble metal. We found that this only occurred when the noble metals and phosphate were in close contact, provided by the impregnation of noble metal on $Ni_xP_yO_z/SiO_2$. A physical mixture between noble metal and phosphate did not provide enough contact to achieve a decrease in synthesis temperature.

The NM-Ni_2P/SiO_2 catalysts showed a higher catalytic activity for thiophene HDS than the non-promoted Ni_2P/SiO_2 catalyst, which may be related to the ease of Ni_3PS formation during reaction due to the lower reduction degree of the NM-Ni_2P/SiO_2 catalysts. All materials showed the same selectivity irrespective of the presence of a noble metal indicating that the noble metal did not participate in the reaction. Finally, LEIS also indicated that the noble metal was not present in the outer layer of the catalyst, further confirming our findings.

References

[1] F. Sun, W. Wu, Z. Wu, J. Guo, Z. Wei, Y. Yang, Z. Jiang, F. Tian, C. Li, J. Catal. 2 (2004) 298—310.
[2] Y. Shu, Y.–K. Lee, S.T. Oyama, J. Catal. 236 (2005) 112—121.
[3] A. Wang, L. Ruan, Y. Teng, X. Li, M. Lu, J. Ren, Y. Wang, Y. Hu, J. Catal. 229 (2005) 314—321.
[4] S.J. Sawhill, K.A. Layman, D.R. Van Wyk, M.H. Engelhard, C. Wang, M.E. Bussel, J. Catal. 231 (2005) 300—313.
[5] A. Montesinos-Castellanos, T.A. Zepeda, B. Pawelec, E. Lima, J.L.G. Fierro, A. Olivas, J.A. de los Reyes H, Appl. Catal. A: Gen. 334 (2008) 330—338.
[6] A.W. Burns, A.F. Gaudette, M.E. Bussel, J. Catal. 260 (2008) 262—269.
[7] Y. Kanda, C. Temma, K. Nakata, T. Kobayashi, M. Sugioka, Y. Uemichi, Appl. Catal. A: Gen. 386 (2010) 171—178.
[8] M. Fang, W. Tang, C. Yu, L. Xia, Z. Xia, Q. Wang, Z. Luo, Fuel Processing Technology. 129 (2015) 236—244.
[9] S.T. Oyama, J. Catal. 216 (2003) 343—352.
[10] X. Wang, P. Clark, S.T. Oyama, J. Catal. 208 (2002) 321—331.
[11] P. Clark, X. Wang, S.T. Oyama, J. Catal. 207 (2002) 256—265.
[12] S.T. Oyama, X. Wang, Y.–K. Lee, K. Bando, F.G. Requejo, J. Catal. 210 (2002) 207—217.
[13] J.A. Cecilia, A. Infantes-Molina, E. Rodríguez-Castellón and A. Jiménez-López, J. Phys. Chem. C (2009), 113, 17032—17044.
[14] S.T. Oyama, X. Wang, Y.–K. Lee, W.–J. Chun, J. Catal. 221 (2004) 263—273.
[15] S.J. Sawhill, D.C. Phillips, M.E. Bussel, J. Catal. 215 (2003) 208—219.
[16] R. Prins, M.E. Bussel, Catal. Lett. 142 (2012) 1413—1436.
[17] Q. Guan, W. Li, M. Zhang, K. Tao, J. Catal. 263 (2009) 1—3.
[18] V. Teixeira da Silva, L.A. Sousa, R.M. Amorim, L. Andrini, S.J.A. Figueroa, F.G. Requejo, J. Catal. 279 (2011) 88—102.
[19] S. Yang, R. Prins, Chem. Commun. (2005), 4178—4180.
[20] S. Yang, C. Liang, R. Prins, J. Catal. (2006), 237, 118—130.
[21] S. Carenco, I. Resa, X. Le Goff, P. Le Floch, N. Mézailles, Chem. Commun. (2008), 2568—2570.
[22] J. Guan, Y. Wang, M. Qin, Y. Yang, X. Li, A. Wang, J. Solid State Chem. (2009), 182, 1550—1555.
[23] P. Bui, J.A. Cecilia, S.T. Oyama, A. Takagaki, A. Infantes-Molina, H. Zhao, D. Li, E. Rodríguez-Castellón, A.J. López, J. Catal. (2012), 294, 184—198.
[24] M. Boudart, Chem. Rev. 95 (1995) 661—666.
[25] J.S. Lee, S. Locatelli, S.T. Oyama, M. Boudart, J. Catal. 125 (1990) 157—170.
[26] A.E. Nelson, M. Sun, A.S.M. Junaid, J. Catal. (2006), 241, 180—188.
[27] Y. Teng, A. Wang, X. Li, J. Xie, Y. Wang, Y. Hu, J. Catal. (2009), 266, 369—379.
[28] J.A. Rodriguez, J.-Y. Kim, J.C. Hanson, S.J. Sawhill, M.E. Bussell, J. Phys. Chem. B (2003), 107, 6276—6285.
[29] T.I. Korányi, Z. Vít, D.G. Poduval, R. Ryoo, H.S. Kim, E.J.M. Hensen, J. Catal. (2008), 253, 119—131.
[30] C.D. Wagner, W.M. Riggs, L.E. Davis, J.F. Moulder, G.E. Muilenberg, Handbook of X-ray photoelectron spectroscopy, Perkin-Elmer Corp., Physical Electronics Division, Eden Prairie, Minnesota, USA, 1979.
[31] C.D. Wagnar, A. Naumkin, A.V. Kraut, NIST X-ray Photoelectron database. Accessed in

11 May 2012.

[32] I. Zafiropoulou, K. Papagelis, N. Boukos, J. Phys. Chem. C. 114 (2010) 7582—7585.

Chapter 8

General discussion

Over 400 billion metric tons of carbon have been released to (and remained in) the atmosphere from the consumption of fossil fuels and cement production since 1751 [1]. Half of these fossil-fuel CO_2 emissions occurred after the industrial revolution (Figure 1) and without any mitigation measures, a further increase of CO_2 emissions from 38 billion metric tons/year in 2015 to 75 billion metric tons/year by 2035 is expected [2].

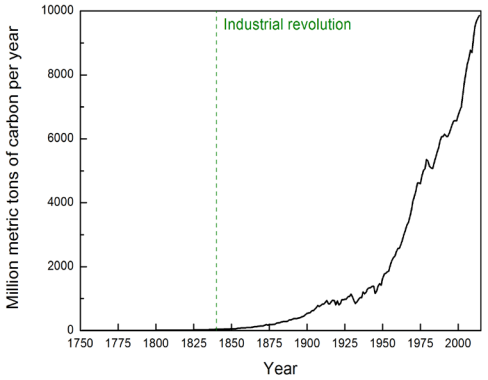

Figure 1. Annual global fossil-fuel carbon emission [Adapted from 1].

It is common knowledge that CO_2 is a greenhouse gas and there is piling evidence that its accumulation in the atmosphere is causing an increase in temperature on earth [3]. This temperature increase relates to changes in the climate and is seen as an urgent issue that needs to be solved. To battle this problem, 144 countries, in the so called Paris agreement, agreed to take measures to keep the global warming well-below 2°C. To address this challenge, energy efficiency measures and the use of renewable resources for energy and materials production is essential and several actions are already undertaken. China, for example, was the world's number one investor in renewable energy in 2014 [4] and committed itself to increase the share of non-fossil fuels used in its primary energy consumption to about 20% by 2030 [5]. In parallel, India has set several targets to increase its renewable energy capacity and, for example, India aims to increase the use of solar and wind power from 4 and 23.76 gigawatts to 100 and 60 gigawatts by 2022, respectively. In addition, India is also committed to increase the use of non-fossil fuel energy sources to 40% by 2030 [6]. In South America, Brazil aims to increase its share of renewables other than hydropower to 28 – 33% of its total energy matrix by 2030 [7, 8]. Furthermore, due to governmental actions, the rate of deforestation in the Brazilian Amazon forest has dropped by 70% compared to the previous decade, preventing 3.2 billion metric tons of CO_2 emissions to the atmosphere [9]. Finally, the European Union, which is leading the discourse on CO_2 emission reduction, aims to increase the share of

renewable energy in its energy consumption matrix to at least 27% and to increase its energy efficiency by 30% by 2030 [5].

Overall, to achieve the demands of the Paris Agreement, a number of countries is committed to revisit their energy matrix aiming at increasing the use of renewable sources like wind, solar, hydropower, geothermal or **biomass**. Amongst all these resources, biomass is the only one that is carbon based. Therefore, in addition to producing energy carriers (fuel), biomass can also be used to produce (bio)chemicals. To produce these (bio)chemicals, the implementation of efficient biorefineries is essential.

In a biorefinery, a biomass-based feedstock – which is derived from the reaction between CO_2, water, nutrients and sunlight, via photosynthesis, to produce the building blocks of biomass – is converted into a range of products (Figure 2) [10]. The processes that happen in a biorefinery are similar to the ones undertaken in a traditional oil refinery excepting that fossil-based feedstocks are used in oil refineries whereas biomass-based feedstocks are used in the biorefineries.

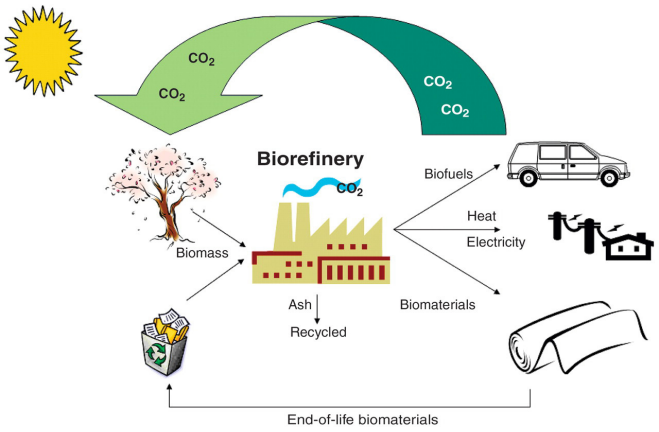

Figure 2. Concept of closed CO_2/materials cycles including the use of biorefinery [10]. Reprinted with permission from AAAS.

The research described in this thesis focuses on the use of vegetable oil based feedstocks to produce drop-in alkanes and alkenes, which is a relevant approach for biorefineries. In this thesis, stearic acid was used as bio-based feedstock since it is regarded as a model compound for studies related to vegetable oil deoxygenation [11 – 13].

Catalytic vegetable oil deoxygenation has been widely explored and the most employed catalysts on this reaction are (noble) metals [11, 12, 14 – 18] or metal-sulfides [19 – 23]. Though all these catalysts are applied with some success they also have their drawbacks. Sulfides need continuous sulfur addition during reaction

to avoid their deactivation [24, 25]. Consequently, undesirable traces of sulfur can be present in the product stream [24, 25]. Metals (noble and non-noble), on the other hand, do not need sulfur addition. However, non-noble metals, such as Ni, favor cracking during triglycerides deoxygenation due to their strong C – C hydrogenolysis ability [11, 16] and have lower activities as compared to noble metals [11]. Noble metals, on the other hand, are scarce, hence expensive. For instance, noble metals such as Ru, Rh, Pd and Pt are around 1,000 times less available than non-noble metals used in industry such as Ni and Mo [26]. Since Ni-phosphides and Mo-carbides have similar electronical properties as noble metals and are more available, Mo-carbides and Ni-phosphides are potential replacements of noble metals for deoxygenation reactions [27 – 32]. Therefore, the understanding of the property-performance relationships for stearic acid deoxygenation (decarboxylation, decarbonylation and hydrodeoxygenation) using metal-carbides and metal-phosphides catalysts is highly desired and was explored in this thesis.

In this chapter, we will argue why transition metal carbides (Mo/W-carbides) and phosphides (Ni-phosphide) should be considered as potential catalysts for deoxygenation processes. The reasons to be discussed are:

1. Mo/W-carbides and Ni-phosphide are active catalysts for deoxygenation reactions;
2. Mo/W-carbides and Ni-phosphide enable tunable product distribution;
3. α-MoC_{1-x}/CNF and β-Mo_2C/CNF are efficient catalysts for stearic acid deoxygenation: the crystal phase depends on the synthesis route of the carbide;
4. Transition metal carbides and phosphides are stable/potentially stable in deoxygenation process.

1. Mo/W-carbides and Ni-phosphide are active catalysts for deoxygenation reactions

One of the aspects to consider for a new catalyst is its activity compared to existing catalysts. Different ways of reporting activities are available such as turnover number (TON) – total number of feedstock molecules converted in the life time of the catalyst; turnover frequency (TOF) – moles of feedstock converted per accessible site per second; reaction rates – moles of feedstock converted per weight of catalyst (or volume of catalyst) per second; and feedstock conversion – percentage of feedstock converted. Though the latter is often used (and will also be used here), it is only meaningful when catalyst loading and reaction conditions (concentration, time) are given to allow a fair comparison between catalysts. Since

TOF gives information on the intrinsic activity of an accessible site, that unit will be used first to make an initial comparison between reported catalysts.

Many authors have used carbides and phosphides as catalysts for deoxygenation reactions (Table 1). Though table 1 gives an indication on the reported activities, it is difficult to compare the catalytic performances directly because the applied reaction conditions vary widely. Therefore, we performed deoxygenation studies over the carbide and phosphide based catalysts under identical reaction conditions. In chapter 4, a comparison of the performance of nickel phosphide and tungsten carbide is presented.

Table 1. Examples of literature using transition metal carbides and phosphides as catalysts for deoxygenation reactions.

Catalyst	**Feedstock**	**Reaction Conditions**	**Reference**
Ni_2P/AC Mo_2C/CNF W_2C/CNF	Stearic acid	350 °C and 3 MPa H_2	This thesis
Ni_2P/SiO_2	Anisole	300 °C and 1.5 MPa H_2	[33]
Mo_2C/TiO_2	Phenol	350 °C and 2.5 MPa H_2	[34]
Mo_2C/CNT	Guaiacol	300 °C and 4 MPa H_2	[35]
Mo_2C/ZrO_2	Phenol	300 °C and 10 MPa H_2	[36]
W_2C/CNF Mo_2C/CNF	Oleic acid	350 °C and 5 MPa H_2	[37]
Ni_2P/SiO_2	Methyl Palmitate	310 °C and 3 MPa H_2	[38]
Ni_2P/MCM-41	Gamma-valerolactone	350 °C and 0.5 MPa H_2	[39]
Ni_2P/MCM-41	Methyl Palmitate	350 °C and 3 MPa H_2	[40]
Mo_2C/MC	Methyl stearate	270 °C and 6 MPa H_2	[41]
Ni_2P/SiO_2	Soybean oil	370 °C and 3 MPa H_2	[42]
β-Mo_2C/Al_2O_3	Sunflower oil	360 °C and 5 MPa H_2	[43]
Ni_2P/SBA-15	Methyl oleate	340 °C and 3 MPa H_2	[44]
Ni_2P/SiO_2	Dibenzofuran	275 °C and 3 MPa H_2	[45]
α-MoC_{1-x}/AC	Guaiacol	340 °C and 0MPa N_2	[46]
Ru_2P/SiO_2	Furan	400 °C and 8.2 mol% furan/H_2 mixture	[47]

In chapter 4 we show that the deoxygenation of stearic acid over Mo-carbide supported on carbon nanofibers (in a batch reactor) predominantly followed the hydrodeoxygenation pathway which resulted in octadecane as main product. On the other hand, when the reaction was performed over the Ni-phosphide, hydrogenation of the fatty acid to the aldehyde/alcohol followed by the decarbonylation of that aldehyde/alcohol resulting in heptadecane was predominant. The latter pathway will be called here the hydrogenation/decarbonylation (HDCO) pathway.

Mo_2C/CNF and Ni_2P/CNF presented a turnover frequency (TOF) of 1 and 179 s^{-1}, respectively, while the TOF of noble metals and sulfides are up to three orders of magnitude lower compared to the phosphides [39, 47]. Thus by using the same reaction conditions to test the different catalysts we concluded that Ni_2P/CNF and Mo_2C/CNF are active catalysts for the deoxygenation of stearic acid and that they can compete, activity wise, with noble metals and metal-sulfides.

2. Mo/W-carbides and Ni-phosphide enable tunable product distribution

Traditionally, deoxygenation of fatty acids is said to occur through two pathways: decarbonylation/decarboxylation (DCO) and/or hydrodeoxygenation (HDO). DCO results in olefins and paraffins in which the product contains one carbon atom less than the starting reactant. HDO results in aldehydes as primary products which can be further converted to alcohols, olefins and paraffins with the same carbon number as the starting material (Figure 3 [37, 48]). When looking more closely into the HDO pathway, it becomes clear that, based on intermediates formed, the reaction route consists of two pathways *i.e.* the HDO pathway and HDCO (hydrogenation/decarbonylation) pathway (Figure 3 [48]). Both pathways start with the hydrogenation of the acid to the aldehyde but after that the pathways diverge. In HDO, the aldehyde is hydrogenated to the alcohol and further converted to olefin and finally paraffin by dehydration/hydrogenation. In de HDCO pathway, the initially formed aldehyde is further converted by decarbonylation/hydrogenation to a paraffin (which is one carbon atom shorter compared to the starting acid). The different end products and intermediates (when possible to isolate) have several applications, which are summarized in Table 2.

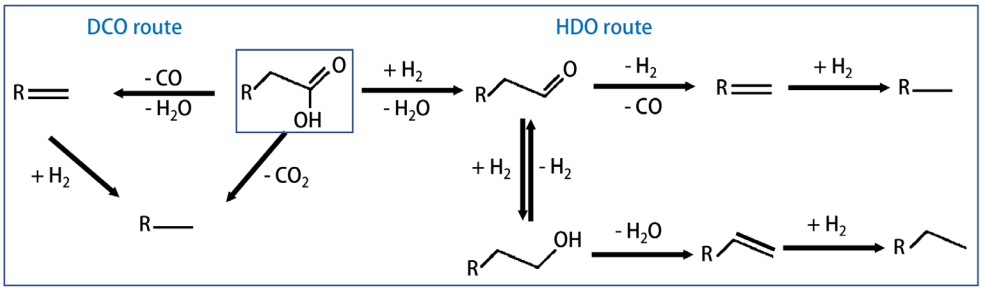

Figure 3. Pathways for deoxygenation of fatty acids.

Table 2. Summary of application for alcohols, aldehydes, olefins and paraffins.

Component	Application	Reference
Alcohol	Fuel or as part of cosmetics, pharmaceutical products, detergents and solvents	[49]
Aldehydes	Disinfectant, food flavor, in perfumes and in pathological, biological, microbiological and dissecting laboratories	[50]
Olefins	Building blocks for plastics and fibers	[51]
Paraffins	Detergent alcohol, solvent and lubrificants markets in addition to the use as diesel-like biofuel when having long carbon chain.	[52]

It has been shown that selectivity depends on the catalyst properties. For example, for Ni-phosphides, catalysts with a lower electron density on the Ni sites (Ni_2P compared to $Ni_{12}P_5$ and Ni_3P) or catalysts with a higher support acidity (Ni_2P/SAPO-11 and Ni_2P-$Ni_{12}P_5$/HY) favor hydrodeoxygenation (HDO) over the decarbonylation (DCO) pathway for the deoxygenation of methyl laurate at 300 – 340 °C and 2 MPa H_2 [53]. In other words, Ni-phosphides with low electron density on the Ni sites or with an acidic support will result in the aldehyde as primary product (alcohols, olefins and paraffins will be formed from them) while Ni-phosphides with a high electron density or low acidic supports will produce only olefins and paraffins.

In addition to the electron density of the Ni sites and acidity of the support, other catalyst properties can also influence selectivity in deoxygenation reactions. In this thesis, the influence of the following properties on the selectivity during stearic acid deoxygenation has been investigated:

a) Nature of active phase (Ni-phosphide vs Mo-carbide)
b) Size of active phase
c) Nature of support

Nature of active phase

It was already discussed above and in Chapter 4 that under the reaction conditions (identical) applied in our research, Mo-carbide favored hydrodeoxygenation (HDO) while Ni-phosphide favored the hydrogenation/decarbonylation (HDCO) pathway. Furthermore, when deoxygenation was carried out over Mo/W-carbides, olefins were observed as intermediates. For example, Figure 4 shows the product distribution for the stearic acid deoxygenation over W_2C/AC catalyst during 6 hours of reaction in a batch reactor. Olefins (green and blue lines) were the main products between 60 and 240 min of reaction, whereas they were completely absent after 300 min of reaction. After that time, mainly paraffins (black and red lines) were obtained. Therefore, when olefins are desired as product, the reaction should be carried out for shorter times while, when paraffins are desired, the reaction time should be prolonged. This holds for a batch process, as described here. When the reaction is performed in a continuous system, the weight hour space velocity (WHSV), *i.e.* contact time, is the relevant parameter to control. Thus, understanding the reaction pathway and therefore the formation of primary, secondary and final products enable us to control production of olefins or paraffins using Mo/W-carbides as catalyst simply controlling the reaction time (batch system) or the contact time (continuous system).

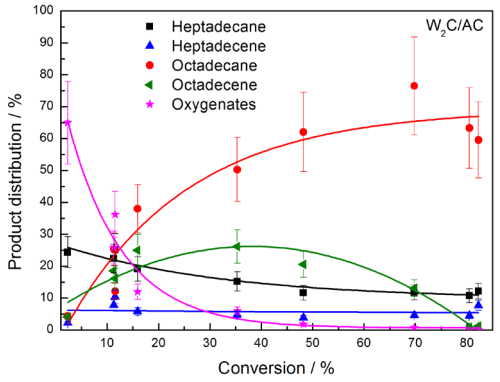

Figure 4. Product distribution of W_2C/AC for stearic acid deoxygenation (250 mg catalyst, 2 g stearic acid, 50 mL solvent, 30 bar H_2, T = 350 °C).

To gain more insight on the prevailing pathways over the carbides and phosphides, the activation energy for the possible reaction pathways was calculated. Over Ni-phosphide, the activation energy for the hydrogenation of stearic acid (54 kJ mol^{-1}) to the aldehyde was significantly lower than for the direct decarboxylation (166 kJ mol^{-1}), indicating that HDO or HDCO is more favorable to occur than DCO over Ni-phosphide catalysts in the stearic acid deoxygenation. Since heptadecane

was the main final product over Ni-phosphide (Figure 5) and it cannot be produced via HDO pathway, we hypothesize that stearic acid deoxygenation occurs mainly via HDCO pathway over Ni-phosphide.

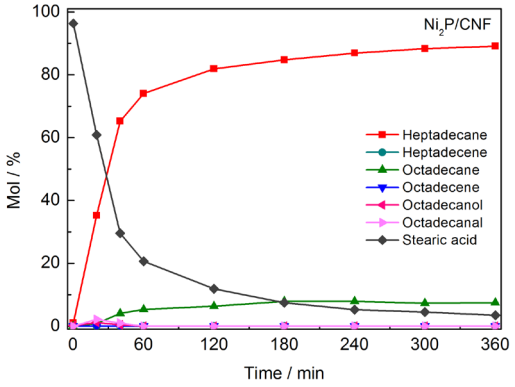

Figure 5. Stearic acid and products concentration (%mol) over time for Ni_2P/CNF for stearic acid deoxygenation (250 mg catalyst, 2 g stearic acid, 50 mL solvent, 30 bar H_2, T = 350 °C).

Regarding Mo-carbide, Shi *et al.* [54] calculated, using density functional theory, the full potential energy surface of the hydrogenation of a fatty acid (butyric acid) to a hydrocarbon (butane) over this catalyst. The steps with the lowest potential energy surface were associated with the predominant pathway. The authors concluded that first, the aldehyde (butanal) is formed from a fatty acid (butyric acid) hydrogenation. Then, the aldehyde is hydrogenated into the alcohol (butanol), which is further hydrogenated into the hydrocarbon (butane). This is in line with our findings which indicate that the HDO pathway is favored over Mo-carbide catalysts.

Size of active phase

In chapter 6, we investigated the influence of the Ni-phosphide particle size on the selectivity of stearic acid deoxygenation. As argued above, the HDCO pathway was the main reaction pathway over nickel phosphide. However, the particle size influenced the predominant reaction pathway. C18 oxygenates (octadecanal and octadecanol, *i.e.* HDCO products) were the major products over 10 wt% Ni_2P/AC, with 8 nm phosphide particles, while C17 hydrocarbons (heptadecane and heptadecene, *i.e.* DCO products) were the major products over 20 wt% (12 nm particles) and 30 wt% (> 30 nm particles) Ni_2P/AC at low conversion (< 10%). This indicates that the hydrogenation of stearic acid (HDCO route) is more facile over smaller particles than over larger particles (12 and > 30 nm). This finding is interesting because when small particles Ni_2P/AC are used in the stearic acid deoxygenation, primary products

such as oxygenates (aldehydes and alcohol) can be obtained, what is not possible when larger particles Ni_2P/AC are employed.

Nature of support

Another catalyst property studied in this thesis that influenced reaction selectivity was the support. Although all analyzed supports in chapter 3 were carbon based, they had differences in their properties such as pore size and acidity. These differences were responsible for distinct product distribution during 6 hours of stearic acid deoxygenation reaction over W-carbides. Oxygenates, *i.e.* hydrogenation products of the carboxylic acid, were initially formed over all catalysts (W_2C/AC, W_2C/CNF and W_2C/CCA), however, the selectivity towards oxygenates was higher over W_2C/AC compared to W_2C/CNF and W_2C/CCA at conversions below 5%. This suggests that the conversion of oxygenates into hydrocarbons was more difficult over W_2C/AC than over W_2C/CNF and W_2C/CCA, which we related to the lower acidity and smaller pore size of W_2C/AC. The support also had an influence on the C18-unsaturated/C18-saturated ratio. At conversions below 30%, W_2C/CNF resulted in the highest C18-unsaturated/C18-saturated ratio in product distribution, which is apparently related to the higher mesopore volume of CNF, which may facilitate the release of unsaturated products during reaction. However, at higher conversions (> 50%), W_2C/CCA resulted in the highest C18-unsaturated/C18-saturated ratio in product distribution, which appeared to be linked to W_2C/CCA having the highest ratio of acid/metallic sites. Whereas metallic sites are associated with hydrogenation of C18-unsaturated into C18-saturated, the acid sites are related to the formation of C18-unsaturated via dehydration of oxygenates.

Those differences in product distribution observed in chapter 3 confirmed that we can also tune the product distribution by changing the supports. However, a deeper study is required to enable us to completely understand the role of catalyst pore size and acidity in the stearic acid deoxygenation. To sum up, Mo/W-carbides and Ni-phosphide are potential catalysts for fatty acid deoxygenation reactions and the selectivity can be tuned by particle size, support and reaction time. This is summarized in Figure 6. Mo/W-carbides favored the olefins formation (octadecene) at short reaction times when supported either on CNF at low conversions or on CCA at high conversions. When supported on AC, instead, W-carbides favored the formation of oxygenates as reaction intermediates. At longer reactions times, on the other hand, those catalysts favored the formation of C18-paraffins (octadecane). Ni-phosphides, in turn, favored the formation of oxygenates as intermediate products when small particle size was used (8 nm), whereas formation of C17-paraffins (heptadecane) was favored when bigger particles were employed (> 12 nm).

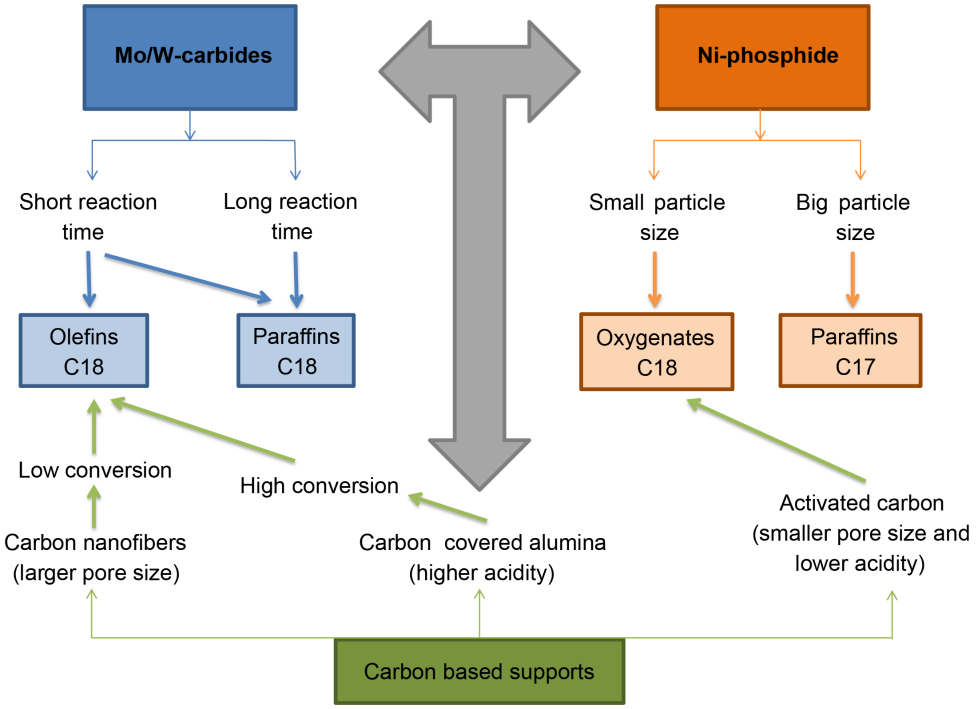

Figure 6. Schematic overview of the influence of catalyst properties in selectivity of stearic acid deoxygenation.

Note that the findings of this thesis summarized in Figure 6 might be restricted to the specific applied reaction conditions (350 °C and 30 bar H_2). Other reaction conditions may influence the results since reaction pressure and temperature are known to influence deoxygenation selectivity [36, 43].

3. α-MoC_{1-x}/CNF and β-Mo_2C/CNF are efficient catalysts for stearic acid deoxygenation: the crystal phase depends on the synthesis route of the carbide

The properties of a catalyst can also depend on the conditions applied during its synthesis. In chapter 5, we focused on the synthesis method of Mo-carbides and we compared the characteristics and performance of Mo-carbides supported on CNF as prepared via temperature programmed carburization and via the carbothermal reduction process. First, it was shown that the ratio between carbon and molybdenum atoms during the catalyst synthesis was a crucial parameter in making carbide based catalysts. Synthesis via the carburization method with 20% CH_4/H_2 resulted in α-MoC_{1-x} while synthesis via carbothermal method with argon resulted in β-Mo_2C. Both catalysts α-MoC_{1-x}/CNF and β-Mo_2C/CNF were applied in the

stearic acid deoxygenation and the alpha phase resulted in a higher weight based activity compared to the beta phase. It is argued in chapter 5 that the higher weight based activity of α-MoC_{1-x}/CNF was due to the catalyst site density. The α-MoC_{1-x} catalyst had a lower site density than the β-Mo_2C. However, although a higher site density is usually linked to better catalytic performance (per unit weight) for several reactions, the lower site density of α-MoC_{1-x}/CNF resulted in more space around the Mo atoms in the α-MoC_{1-x} phase, making the Mo atoms more accessible for the large reactant molecule in our experiments (stearic acid), resulting in its better weight based catalyst activity.

Another issue related to transition metal carbides and phosphides is their high synthesis temperature compared to that of noble metals. While noble metals are activated between 200 and 360 °C [11], especially metal phosphides usually need temperatures over 650 °C to be activated [55]. It would be beneficial if this synthesis temperature could be lowered. A method to decrease the synthesis temperature of Ni-phosphide has been described in chapter 7. It was shown that adding small amounts (1 wt%) of noble metal did decrease the temperatures needed to effectively make supported Ni-phosphides. The regular method to synthesize supported nickel phosphide is the temperature-programmed reduction, which consists on reducing the catalyst under hydrogen flow from room temperature to 650 °C [55]. We showed that this final synthesis temperature decreased to 450 °C when 1 % of noble metal (Rh, Pt or Pd) was added to the catalyst.

4. Transition metal carbides and phosphides are stable/potentially stable in hydrodeoxygenation process

When a catalyst is evaluated to be used in any process, one aspect is paramount for its good performance: stability. Many reports classify transition metal carbides and phosphides as stable catalysts for deoxygenation reactions [27, 56 – 66]. However, in chapter 2 we showed that, depending on catalyst properties, these catalysts can deactivate during triglyceride's deoxygenation under specific reaction conditions. We inferred from the literature that transition metal carbides can deactivate in liquid phase reactions by coke formation, sintering, leaching and oxidation. For example, the nature of support can influence catalyst deactivation by leaching. Since a strong interaction between carbon based supports and carbides active phases is not guaranteed, deactivation by leaching is facilitated when those supports are employed.

The crystallite size of the active phase is another important parameter for stability. It has been reported that smaller carbide particles (< 20 nm) are easier to oxidize. Therefore, especially with small nanoparticles, deactivation by oxidation

needs to be considered.

To conclude, Mo/W-carbides and Ni-phosphide are interesting catalysts for deoxygenation reactions due to their similar or higher catalytic activity compared to noble metals and metal sulfides. However, a few issues about those catalysts remain for discussion, such as their stability and synthesis temperature. In this thesis I brought insights in the connection between deactivation routes and catalyst properties (Chapter 2) and some solutions to decrease their synthesis temperature (Chapter 7). Moreover, I also brought insights in the relation between specific catalyst properties, such as support (Chapter 3), active phase (Chapter 4), synthesis method (Chapter 5) and particle size (Chapter 6), and selectivity, what contributes to a better understanding of Mo/W-carbides and Ni-phosphide performance in deoxygenation reactions. Note that most studies performed in this thesis and in the cited literature were carried out in a batch system although many industrial plants use continuous operation system. Therefore, further studies should be performed in continuous operation system to broaden the understanding and usability of Mo/W-carbides and Ni-phosphide as commercial catalysts for deoxygenation reactions.

The results of this thesis contribute to a deeper understanding about a potential substitute of noble metal catalysts and to the development of the biomass conversion field, more specifically, triglycerides deoxygenation. Hence, those findings contribute to the renewable energy field and can be used to assist countries to strike the global warming issue and to reach the demands of the Paris Agreement.

References

[1] Boden, T.A., G. Marland, and R.J. Andres. 2017. Global, Regional, and National Fossil-Fuel CO2 Emissions. Carbon Dioxide Information Analysis Center, Oak Ridge National Laboratory, U.S. Department of Energy, Oak Ridge, Tenn., U.S.A. doi 10.3334/CDIAC/00001_V2017
[2] N. Abas, A. Kalair, N. Khan, Futures (2015), 69, 31 – 49.
[3] V. K. Arora, J. F. Scinocca, G. J. Boer, J. R. Christian, K. L. Denman, G. M. Flato, V. V. Kharin, W. G. Lee, W. J. Merryfield, Geophysical Research Letters (2011), 38, 1 – 6.
[4] http://www.chinafaqs.org/files/chinainfo/ChinaFAQs_Renewable_Energy_Graphical_Overview_of_2014.pdf
[5] World Resources Institute, "What are other countries doing on climate change?", October 2015. Accessible in: wri.org/countryactions
[6] Government of India, "India's Intended Nationally Determined Contribution: Working towards Climate Justice," submitted to UNFCCC on October 1, 2015. Accessible in: http://www4.unfccc.int/submissions/INDC/Published%20Documents/India/1/INDIA%20INDC%20TO%20UNFCCC.pdf.
[7] Government of Brazil, "Intended Nationally Determined Contribution towards Achieving the Objective of the United Nations Framework Convention on Climate Change," submitted to UNFCCC on September 28, 2015. Accessible in: http://www4.unfccc.int/submissions/INDC/Published%20
Documents/Brazil/1/BRAZIL%20iNDC%20english%20FINAL.pdf.
[8] International Energy Agency (IEA), 2014, World Energy Outlook special report for Southeast Asia, IEA, Paris.
[9] D. Nepstad, D. McGrath, C. Stickler, A. Alencar, A. Azevedo, B. Swette, T. Bezerra, M. DiGiano, J. Shimada, R. S. da Motta, E. Armijo, L. Castello, P. Brando, M. C. Hansen, M. McGraph-Horn, O. Carvalho, L. Hess, Science (2014), 344, 1118 – 1123.
[10] A. J. Ragauskas, C. K. Williams, B. H. Davison, G. Britovsek, J. Cairney, C. A. Eckert, W. J. Frederick Jr., J. P. Hallett, D. J. Leak, C. L. Liotta, J. R. Mielenz, R. Murphy, R. Templer, T. Tschaplinski, Science (2006), 311, 484 – 489.
[11] M. Snare, I. Kubicková, P. Mäki-Arvela, K. Eränen, D. Yu. Murzin, Ind. Eng. Chem. Res. (2006), 45, 5708 – 5715.
[12] I. Kubicková, M. Snare, K. Eränen, P. Mäki-Arvela, D. Y. Murzin, Catal. Today (2005), 197 – 200.
[13] P. Mäki-Arvela, I. Kubicková, M. Snare, K. Eranen, D. Y. Murzin, Energy Fuels (2007), 21, 30 – 41.
[14] N. Asikin-Mijan, H. V. Lee, J. C. Juan, A. R. Noorsaadah, H. C. Ong, S. M. Razali, Y. H. Taufiq-Yap, Appl. Catal. A (2018), 38 – 48.
[15] N. Asikin-Mijan, H. V. Lee, G. Abdulkareem-Alsultan, A. Afandi, Y. H. Taufiq-Yap, J. Clean. Prod. (2017), 167, 1048 – 1059.
[16] B. Peng, Y. Yao, C. Zhao, J. A. Lercher, Angew. Chem. Int. Ed. (2012), 51, 2072 – 2075.
[17] L. Boda, G. Onyestyák, H. Solt, F. Lónyi, J. Valyon, A. Thernesz, Appl. Catal. A (2010), 158 – 169.
[18] J. G. Immer, M. J. Kelly, H. H. Lamb, Appl. Catal. A (2010), 134 – 139.
[19] D. Kubicka, L. Kaluza, Appl. Catal. A (2010), 199 – 208.
[20] P. Simácek, D. Kubicka, G. Sebor, M. Pospísil, Fuel (2010), 611 – 615.
[21] B. Donnis, R. G. Egeberg, P. Blom, K. G. Knudsen, Top. Catal. (2009), 229 – 240.
[22] D. Kubicka, M. Bejblová, J. Vlk, Top. Catal. (2010), 168 – 178.
[23] D. Kubicka, P. Simacek, N. Zilková, Top. Catal. (2009), 161 – 168.

[24] D. Kubicka, J. Horacek, , Appl. Catal. A: Gen. (2011), 394, 9 – 17.
[25] P. M. Mortensen, D. Gardini, C. D. Damsgaard, J-D. Grunwaldt, P. A. Jensen, J. B. Wagner, A. D. Jensen, Appl. Catal. A: Gen. (2016), 523, 159 – 170.
[26] U.S. Geological Survey, 2017, Mineral commodity summaries 2017: U.S. Geological Survey, 202 p., http://doi.org/10.3133/70180197.
[27] B. Dhanadapani, T. St. Clair, S. T. Oyama, Appl. Catal. A: Gen. (1998), 168, 219 – 228.
[28] S. T. Oyama, Catal. Today (1992), 15, 179 – 200.
[29] J. B. Claridge, A. P. E. York, A. J. Brungs, C. M.-Alvarez, J. Sloan, S. C. Tsang, M. L. H. Green, J. Catal. (1998), 180, 85 – 100.
[30] J. Kibsgaard, T. F. Jaramillo, Angew. Chem. Int. Ed. (2014), 53, 14433 – 14437.
[31] R. Prins, M. E. Bussel, Catal. Lett. (2012), 142, 1413 – 1436.
[32] A.-M. Alexander, J. S. J. Hargreaves, Chem. Soc. Rev. (2010), 39, 4388 – 4401.
[33] K. Li, R. Wang, J. Chen, Energy Fuels, (2011), 25, 854 – 863.
[34] S. B.-Eiras, R. Lodeng, H. Bergem, M. Stocker, L. Hannevold, E. A. Blekkan, Catal. Today (2014), 223, 44 – 53.
[35] E. S.-Jimenez, M. Perdu, R. Pace, T. Morgan, M. Crocker, Catalysts (2015), 5, 424 – 441.
[36] P. M. Mortensen, H. W. P. de Carvalho, J.-D. Grunwaldt, P. A. Jensen, A. D. Jensen, J. Catal. (2015), 328, 208 – 215.
[37] S. A. W. Hollak, R. W. Gosselink, D. S. van Es, J. H. Bitter, ACS Catal. (2013), 3, 2837 – 2844.
[38] F. Han, Q. Guan, W. Li, RSC Adv. (2015), 5, 107533 – 107539.
[39] G.-N. Yun, A. Takagaki, R. Kikuchi, S. T. Oyama, Catal. Sci. Technol. (2017), 7, 281 – 292.
[40] Q. Guan, F. Wan, F. Han, Z. Liu, W. Li, Catal. Today (2016), 259, 467 – 473.
[41] M. Lu, F. Lu, J. Zhu, M. Li, J. Zhu, Y. Shan, Reac. Kinet. Mech. Cat. (2015), 115, 251 – 262.
[42] R. Zarchin, M. Rabaev, R. V.-Nehemya, M. V. Landau, M. Herskowitz, Fuel (2015), 139, 684 – 691.
[43] L. A. Sousa, J. L. Zotin, V. Teixeira da Silva, Appl. Catal. A: Gen., (2012), 449, 105 – 111.
[44] Y. Yang, C. O.-Hernández, P. Pizarro, V. A. de la P. O'Shea, J. M. Coronado, D. P Serrano, Fuel (2015), 144, 60 – 70.
[45] A. Infantes-Molina, E. Gralberg, J. A. Cecilia, E. Finocchio, E. Rodríguez-Castellón, Catal. Sci. Technol. (2015), 5, 3403 – 3415.
[46] R. Ma, K. Cui, L. Yang, X. Ma, Y. Li, Chem. Commun. (2015), 10299 – 10301.
[47] R. H. Bowker, M. C. Smith, M. L. Pease, K. M. Slenkamp, L. Kovarik, M. E. Bussel, ACS Catal. (2011), 1, 917 – 922.
[48] R. W. Gosselink, D. R. Stellwagen, J. H. Bitter, Angew. Chem. Int. Ed., (2013), 52, 5089 – 5092.
[49] www.locatellialcool.it/en/products-and-services/industrial-alcohol.html, accessed in 19 January 2017.
[50] www.ktgss.edu.hk/academic/chemistry/201112/S5/5D/homologous/Aldehyde%20_Chem.pdf, accessed in 19 January 2017.
[51] www.cpchem.com/bl/olefins/en-us/Pages/default.aspx, accessed in 19 January 2017.
[52]www.ihs.com/products/normal-paraffins-chemical-economics-handbook.html, accessed in 19 January 2017.
[53] H. Shi, J. Chen, Y. Yang, S. Tian, Fuel Process. Technol. (2014), 118, 161 – 170.

[54] Y. Shi, Y. Yang, Y. -W. Li, H. Jiao, Catal. Sci. Technol. (2016), 6, 4923 – 4936.
[55] S. T. Oyama, J. Catal. (2003), 216, 343 – 352.
[56] V. M. L. Whiffen, K. J. Smith, Top. Catal. (2012), 55, 981 – 990.
[57] S. T. Oyama, X. Wang, Y.-K. Lee, W.-J. Chun, J. Catal. (2004), 263 – 273.
[58] P. A. Clark, S. T. Oyama, J. Catal. (2003), 218, 78 – 87.
[59] A. L. Jongerius, R. W. Gosselink, J. Dijkstra, J. H. Bitter, P. C. A. Bruijnincx, B. M. Weckhuysen, ChemCatChem (2013), 5, 2964 – 2972.
[60] Y. Qin, P. Chen, J. Duan, J. Han, H. Lou, X. Zheng, H. Hong, RSC Adv. (2013), 3, 17485 – 17491.
[61] V. M. L. Whiffen, K. J. Smith, Energy Fuels (2010), 24, 4728 – 4737.
[62] C. Li, M. Zheng, A. Wang, T. Zhang, Energy Environ. Sci. (2012), 5, 6383 – 6390.
[63] E. F. Mai, M. A. Machado, T. E. Davies, J. A. L.-Sanchez, V. Teixeira da Silva, Green Chem. (2014), 16, 4092 – 4097.
[64] J. A. Cecilia, A. I.-Molina, E. R.-Castellón, A. J.-Lopez, S. T. Oyama, Appl. Catal. B: Environm. (2013), 136 – 137, 140 – 149.
[65] Y.-B. Huang, M.-Y. Chen, L. Yan, Q.-X. Guo, Y. Fu, ChemSusChem (2014), 7, 1068 – 1070.
[66] P. Thüne, P. Moodley, F. Scheijen, H. Fredriksson, R. J. Kropf, J. Miller, J. W. Niemantsverdriet, J. Phys. Chem. C (2012), 116, 7367 – 7373.

Appendices

Supplementary information

Appendix A

Supplementary information - Chapter 3

A.1 Nitrogen adsorption/desorption isotherms

Figure A1 displays the nitrogen adsorption/desorption isotherm curves of the pure supports and the three supported W_2C catalysts.

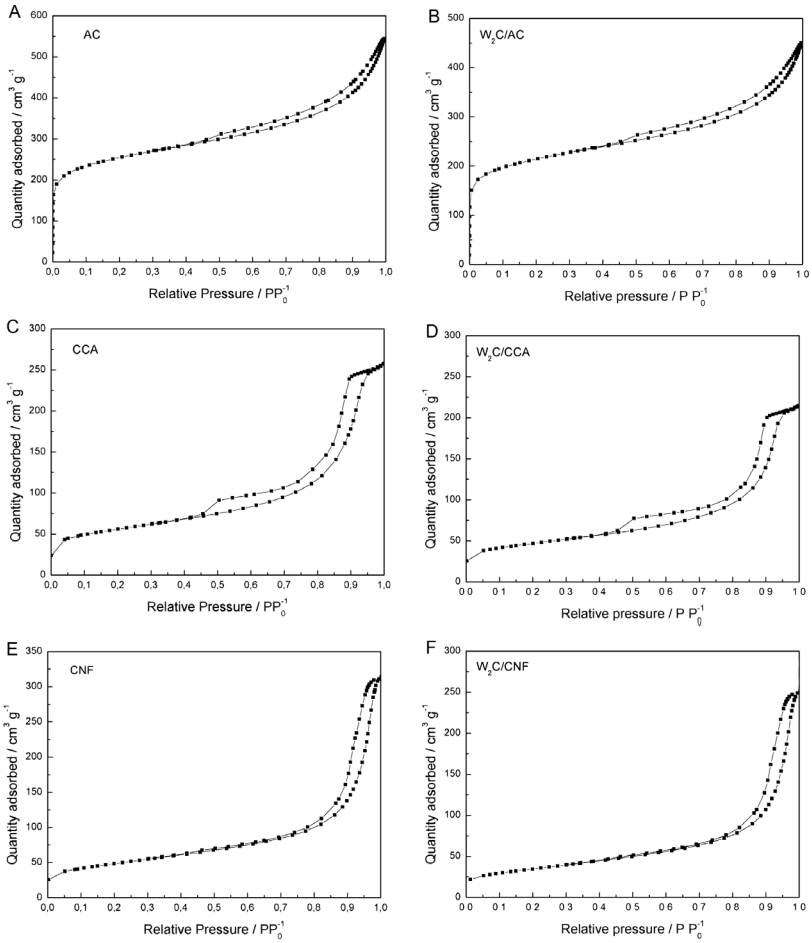

Figure A1. Nitrogen adsorption/desorption isotherms for AC, CCA, CNF and for the three supported W_2C catalysts.

A.2 CO_2 Diffuse Reflectance Infrared Fourier Transform Spectroscopy (CO_2 DRIFTS)

To confirm that alumina was completely covered by carbon monolayers (CCA support), we performed CO_2 DRIFTS analysis. Figure A2 shows the results.

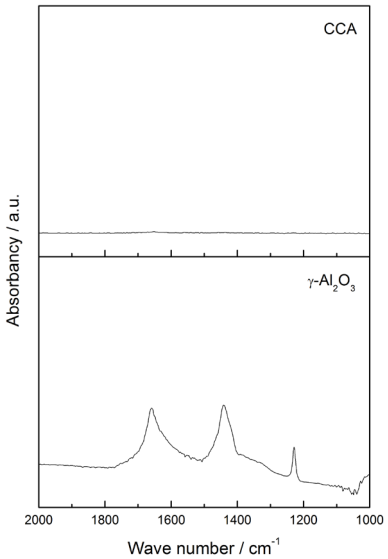

Figure A2. CO_2 DRIFTS spectra for the region 2000 cm^{-1} to 1000 cm^{-1} of γ-Al_2O_3 and CCA after CO_2 adsorption.

The spectrum for alumina shows infrared bands at 1665, 1440 and 1225 cm^{-1}. These bands are related to symmetric and asymmetric stretching of OCO bonds and to the deformation modes of COH from adsorbed bicarbonates species. Bicarbonates species are formed by interaction between CO_2 and alumina's nucleophilic centers [1]. Since there are no bands that refer to bicarbonates on CCA profile, we conclude that alumina is fully covered by carbon over the support.

A.3 Internal and external mass transfer limitation analysis

We carried out two groups of experiments to analyze the presence of internal and external mass transfer limitations during reaction.

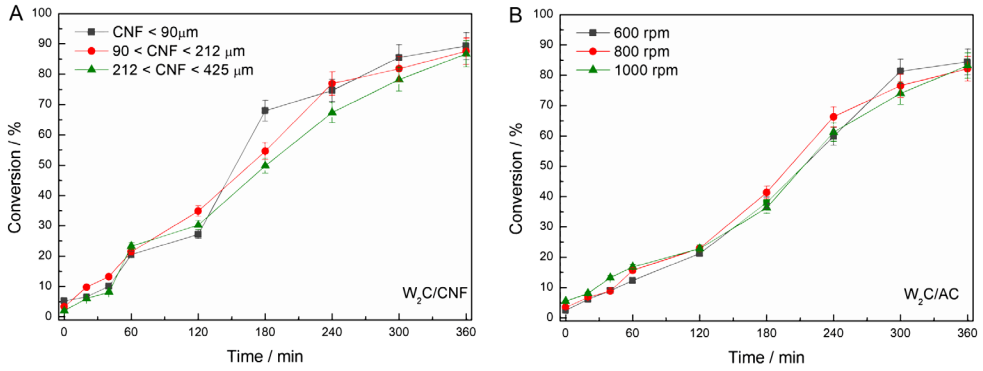

Figure A3. Evaluation of A) internal mass transfer limitations and B) external mass transfer limitations (250 mg catalyst, 2 g stearic acid, 50 mL solvent, 30 bar H_2, 350 °C).

Figure A3(A) depicts the performance of W_2C/CNF catalysts with different granulometries, defined by siefting, evaluated to analyze internal mass transfer limitations (250 mg catalyst, 2 g stearic acid, 50 mL solvent, 30 bar H_2, 350 ºC). As Figure A3(A) makes clear, W_2C/CNF with different granulometries (< 90 μm, 90 to 212 μm, 212 to 425 μm) obtained the same conversion over time. This confirms that the reaction was not limited by internal mass transfer.

Figure A3(B) displays the performance of W_2C/AC at different mixing intensities (600, 800 and 1000 rpm), evaluated to analyze external mass transfer limitations (250 mg catalyst, 2 g stearic acid, 50 mL solvent, 30 bar H_2, 350 °C). W_2C/AC achieved the same conversion over time for different mixing intensities (600, 800 and 1000 rpm). This result confirms that the reaction was not limited by external mass transfer.

References

[1] C. G. Visconti, L. Lietti, E. Tronconi, P. Forzatti, R. Zennaro, E. Finocchio, Appl. Catal. A: Gen., Fischer-Tropsch synthesis on Co/Al_2O_3 catalyst with CO_2 containing syngas (2009), v. 355, 1 – 2, 61 – 68.

Appendix B

Supplementary information - Chapter 5

B.1 Formulas used to evaluate catalyst performance

- Conversion:

$$x_A = \frac{[stearic\ acid]_{final} - [stearic\ acid]_{initial}}{[stearic\ acid]_{initial}} \times 100\%$$

$[stearic\ acid]$ = concentration of stearic acid (g L^{-1})

- Turnover frequency (TOF):

$$TOF = \frac{-r_A}{Active\ sites}$$

$-r_A$ = reaction rate (mmol g^{-1} h^{-1}), as follows:

$$-r_A = \frac{N_{A0} \times {dx_A}/{dt}}{W}$$

N_{A0} = moles of stearic acid
W = mass of catalyst (g)
t = time (h)

- Selectivity

$$S_i = \frac{mol_i}{\sum mol_{products}} \times 100\%$$

B.2 XRD diffractograms

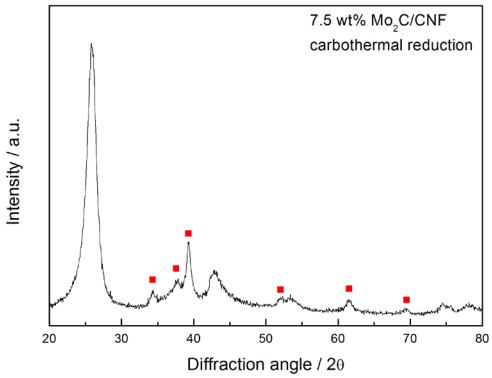

Figure B1. XRD diffractogram for 7.5 wt% Mo_2C/CNF synthesized via carbothermal reduction with argon (■ indicates hexagonal β-Mo_2C; a.u. stands for arbitrary units).

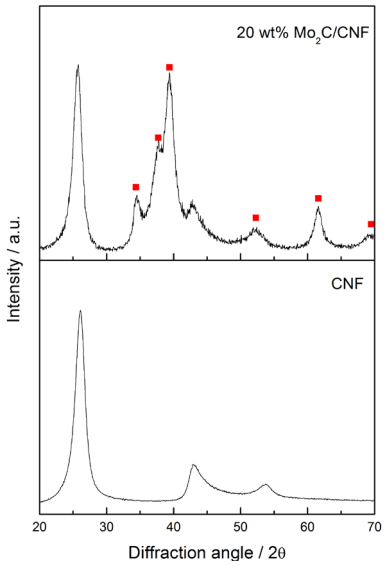

Figure B2. In-situ XRD diffractogram for 20 wt% Mo_2C/CNF synthesized via carburization with 20% CH_4/H_2 gas mixture (■ indicates hexagonal β-Mo_2C).

B.3 Calculation of C/Mo molar ratio for catalysts with 7.5 and 20 wt% Mo loading synthesized via carburization method

During the catalyst synthesis for XRD characterization, 0.2 g of catalyst was carburized in situ using 100 mL min^{-1} 20% CH_4/H_2 from 20 to 650 °C (heating rate = 2.5 °C min^{-1}) and maintained at that temperature for 2 hours. Thus, the amount of carbon from the methane can be calculated as follows:

$$mol_{C1} = mol_{CH_4} = \frac{m_{CH_4}}{MM_{CH_4}} = \rho_{CH_4} \times V_{CH_4} = \rho_{CH_4} \times \dot{V}_{CH_4} \times t$$

where:

Variables	Description	Value
mol_{CH_4}	Mol of CH_4	Calculated = 0.3108 mol
m_{CH_4}	Mass of CH_4	Calculated = 4.9856 g
MM_{CH_4}	CH_4 molecular weight	16.04 g mol^{-1}
ρ_{CH_4}	CH_4 density	0.656 kg m^{-3} = 0.656 g dm^{-3}
V_{CH_4}	Volume of CH_4	7600 mL = 7.6 L = 7.6 dm^3
$\dot{V}_{CH_4}$	Volume flow of CH_4	20 mL min^{-1}
t	Carburization time	380 min

Calculation of carbon and molybdenum amounts for catalyst with 7.5 wt% Mo loading:

$$mol_{C2} = 0.5 \times mol_{Mo} = \frac{m_{Mo}}{MM_{Mo}} = \frac{7.5\% \times m_{total}}{MM_{Mo}}$$

where:

Variables	Description	Value
mol_{Mo}	Mol of molybdenum	Calculated = 0.000156 mol
m_{Mo}	Mass of molybdenum	Calculated = 0.015 g
MM_{Mo}	Molybdenum molecular weight	94.95 g mol^{-1}
m_{total}	Mass of total sample	0.2 g

Total amount of Mo = mol_{Mo}

Total amount of C = $mol_{C1} + mol_{C2}$

Finally,

$$\frac{C}{Mo} ratio = \frac{mol_{Mo}}{mol_{C1} + mol_{C2}} = 1989$$

Calculation of carbon and molybdenum amounts for catalyst with 20 wt% Mo loading:

$$mol_{C2} = 0.5 \times mol_{Mo} = \frac{m_{Mo}}{MM_{Mo}} = \frac{20\% \times m_{total}}{MM_{Mo}}$$

where:

Variables	Description	Value
mol_{Mo}	Mol of molybdenum	Calculated = 0.000147 mol
m_{Mo}	Mass of molybdenum	Calculated = 0.04 g
MM_{Mo}	Molybdenum molecular weight	94.95 g mol^{-1}
m_{total}	Mass of total sample	0.2 g

Total amount of Mo = mol_{Mo}

Total amount of C = $mol_{C1} + mol_{C2}$

Finally,

$$\frac{C}{Mo} ratio = \frac{mol_{Mo}}{mol_{C1} + mol_{C2}} = 746$$

B.4 Calculation of carbide reactivity using TEM and XRD results

The carbide reactivities were calculated on the basis of the particle size obtained via TEM (~250 particles) and XRD of the α-MoC_{1-x}/CNF and β-Mo_2C/CNF catalysts (Table B1). The following equations were employed:

Particle surface area: $A\ (m^2) = \pi \times d^2$;

Particle volume: $V\ (m^3) = \frac{\pi \times d^3}{6}$;

Particle mass: $m\ (g) = \rho \times V$;

In the above, d is particle diameter (m) and ρ is particle density.

Table B1. Number-average, volume-average and surface-average particle size of α-MoC_{1-x}/CNF and β-Mo_2C/CNF catalysts calculated from TEM results.

	α-MoC_{1-x}/CNF	**β-Mo_2C/CNF**
Number-average particle size (nm)	2	6
Volume-average particle size (nm)	3	14
Surface-average particle size (nm)	2	11

Table B1 displays the number-average, volume-average and surface-average particle size of the α-MoC_{1-x}/CNF and β-Mo_2C/CNF catalysts as calculated from the TEM results. For α-MoC_{1-x}/CNF, this calculation resulted in the same particle size for number, volume and surface average. However, the number-average particle size of β-Mo_2C/CNF is smaller (6 nm) than the volume-average and surface-average particle sizes (14 and 11 nm, respectively).

As Figure 5 (Chapter 5) shows, α-MoC_{1-x}/CNF presented a monomodal particle size distribution, while β-Mo_2C/CNF presented a bimodal distribution. This bimodal distribution of β-Mo_2C/CNF influences the number-average, volume-average and surface-average particle size and this is responsible for the observed differences. The bimodal distribution also makes it difficult to measure accurate particle sizes based on XRD (we obtained a volume average particle size of 13 nm for β-Mo_2C/CNF) because the volume-average particle size is calculated mostly on the basis on the larger particles.

On the other hand, the particle size is not relevant for the calculation of catalyst reactivity via CO chemisorption since this technique measures the number of active sites independently of catalyst particle size. This makes CO chemisorption the technique of choice for measuring catalyst activity when a bimodal particle size distribution is present.

Appendix C

Supplementary information - Chapter 6

Figure C1 exhibits water formation profiles for 10, 20 and 30 wt% Ni_2P/AC during the reduction of the catalysts. In that step the adsorbed phosphate is converted to the phosphide with the concomitant release of water. All TPR profiles present two peaks with maxima around 350 and 460 ˚C. According to Feitosa *et al.* [1], the peak at 350 ˚C is related to a surface reduction of nickel phosphate particles forming a layer of partially reduced nickel phosphate. This layer slows down the hydrogen diffusion towards the bulk, resulting in the second reduction peak (460 ˚C) to form nickel phosphide.

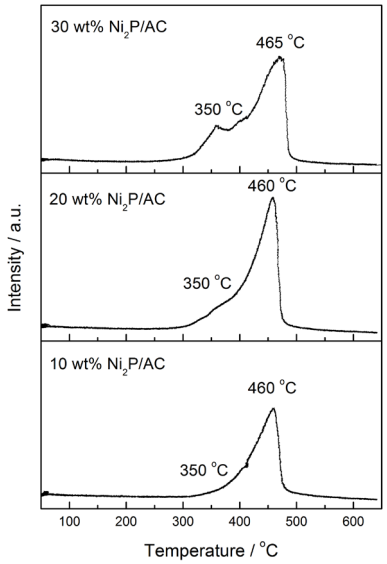

Figure C1. Water TPR profiles for the 10, 20 and 30 wt% Ni_2P/AC catalysts.

References

[1] L.F. Feitosa, G. Berhault, D. Laurenti, T.E. Davies, V. Teixeira da Silva, J. Catal. 340 (2016) 154–165.

Appendix D

Supplementary information - Chapter 7

D.1 Influence of reduction temperature of Ni_2P/SiO_2 in thiophene HDS reaction

Samples of $Ni_xP_yO_z/SiO_2$ were reduced at different temperatures by TPR from room temperature to 723 – 1023 K with heating rate at 1 K min^{-1} and identified as follows:

Sample codes synthesized at different temperatures.

Sample	Description
P723	Ni_2P/SiO_2 with reduction temperature of 723 K
P773	Ni_2P/SiO_2 with reduction temperature of 773 K
P823	Ni_2P/SiO_2 with reduction temperature of 823 K
P873	Ni_2P/SiO_2 with reduction temperature of 873 K
P923	Ni_2P/SiO_2 with reduction temperature of 923 K
P973	Ni_2P/SiO_2 with reduction temperature of 973 K
P1023	Ni_2P/SiO_2 with reduction temperature of 1023 K

Figure D1 displays the XRD diffractograms of the above mentioned samples.

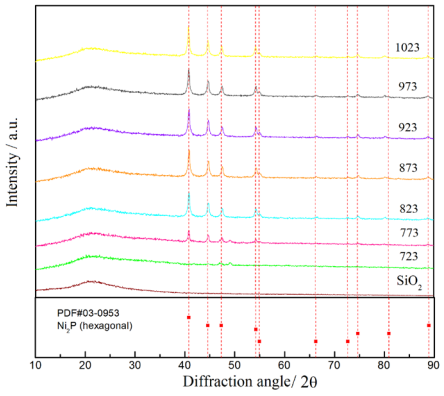

Figure D1. XRD diffractograms of samples SiO_2 (brown), P723 (green), P773 (pink), P823 (blue), P873 (orange), P923 (purple), P973 (black) and P1023 (yellow).

Summary

Renewable resources are indispensable to secure our planet for future generations. While wind, solar and hydropower can provide the energy (electricity) we need, they cannot provide the chemical molecules we need. For that, biomass is the only renewable option. Biomass has the potential to be a source of renewable chemical building blocks and liquid fuels. However conversion of biomass into molecules is needed to make the desired chemical building blocks.

In this thesis, the deoxygenation of stearic acid was used as model reaction for the deoxygenation of biobased oils such as (non-edible) vegetable oils and waste cooking oils. Currently, for these deoxygenation reactions, mainly noble metal based catalyst and non-noble metal sulfides are used as catalysts. Both have their drawbacks. For noble metals, their availability is an issue and for the sulfides, the loss of sulfur, which end up in the products, is a major drawback. Therefore, I studied Ni-phosphide and Mo/W-carbides as potential catalyst since they have similar electronic structures as noble metals, thus a similar reactivity is expected, and are more available.

Although lately Ni-phosphide and Mo/W-carbides have been studied as potential catalysts for deoxygenation reactions, there are still unsolved issues regarding activity, selectivity and stability of these catalysts. In this thesis, I first performed a review study about deactivation routes of carbides in liquid phases reactions. Based on the literature reports, I brought insights in the connection between deactivation routes and carbide properties. For example, the use of carbon based supports might lead to deactivation by leaching.

In the thesis I developed further insights in the catalyst properties that determine the performance of Ni-phosphide and Mo/W-carbides. I showed that the nature of active phase (Mo_2C/CNF vs Ni_2P/CNF), support (W_2C/AC vs W_2C/CNF vs W_2C/CCA), particle size (10, 20 and 30 wt% Ni_2P/AC) and synthesis method (carburization vs carbothermal reduction of Mo_2C/CNF) had an influence on the catalyst performance. I found that synthesis via carburization method lead to the α-MoC_{1-x} phase while synthesis via carbothermal method lead to the β-Mo_2C phase. The former was more active (in a weight basis) due to its lower site density which

allowed an easier access of the reactants to the catalytic active site.

I also found that Mo/W-carbides favored the hydrodeoxygenation (HDO) pathway whereas Ni-phosphide favored the hydrogenation/decarbonylation (HDCO). Moreover, the HDCO pathway was more facile over smaller Ni-phosphide particles (8 nm) than over larger particles (12 and > 30 nm). Over the latter the decarbonylation/decarboxylation (DCO) pathway was predominant.

With this understanding it is now possible to steer the selectivity of deoxygenation of fatty acids to specific products such as aldehyde, alcohols, alkanes and alkenes. These molecules are desired by the chemical industry to be used in products such as cosmetics, disinfectant, plastics, solvents and pharmaceutical products. Thus with this thesis I contributed to the further development of a biobased economy.

Aknowledgments

First, I would like to thank my parents, **Niwton** and **Eliana**, for raising me in the best way I could wish. Thank you for being my life example, for being there every day, every time, every single moment I need (or just want) you. You are my everything. Thank you for encouraging (or at least accepting) me to live 8309 km away from you even knowing that we miss each other every day. You are the best parents I could have and you are just perfect for me. I will be forever grateful to you. Secondly, I would like to thank my sister **Bianca**, now my best friend, for all the support, the encouraging, the everyday talks and for giving me the prettiest and cutest niece forever! Love you, sis!

Thank you, **Julio**, my dearest husband, for being just who you are. Thank you for all the talks, the encouraging, the smiles, the light everyday life, the affection… thank you for everything! I cannot forget about thanking you for all corrections and suggestions about my thesis even not working in the same field. You are just perfect!

Victor, it is a pity that I did not have the opportunity to thank you as much as I wanted while I could. You were the best supervisor I could ever have. You were always available to help me not only in the technical and professional aspects of this PhD but also in the personal ones. Thank you for supporting me during my abroad experience in Wageningen, for all the talks, for being there just to say: everything is going to be ok. Imagining that you will not read this final work or that you will not be in my defense is devastating. Thank you for being part of my life. Rest in peace.

Harry, thank you for being this outstanding professional and very nice supervisor. You are always focused on getting the most out my capacity and at the same time you learned when I needed some encouraging words. In this way, I am very pleased to have you as my supervisor. Thank you for relying on me, for all the teaching, for making my staying in Wageningen so easy and specially for being so friendly, optimistic and attentive in these last months. We made it! ☺

I would like to thank all the **staff members** of both NUCAT and BCT groups for helping me with all the technical issues. A special thanks for **Dora** and **Macarrão** for all the support and good times in NUCAT and for **Gerda** for helping me with all the paperwork and making my time in WUR much easier and nicer.

During this PhD I made many **friends**, both in Brazil and in the Netherlands. I would like to thank them for all the fun, good moments, and for making this part of my life more pleasurable. Thank you **BCT** group. Thank you **NUCAT**. Thank you "**Aterrorizando Waggy**".

About the author

Curriculum Vitae

Luana Macedo received her B.S. in Chemical Engineering from the Federal University of Bahia (Brazil) in 2011 and her M.Sc. in Chemical Engineering from the Federal University of Rio de Janeiro (Brazil) in 2014. Her M.Sc. research focused on understanding the influence of synthesis temperature of silica supported nickel phosphide on the thiophene hydrodesulfurization reaction. As a Ph.D. student of both Federal University of Rio de Janeiro (Brazil) and Wageningen University (The Netherlands), Luana developed a research focused on the evaluation of influence of several properties of carbides and phosphides (active phase, support, particle size, synthesis method) on activity and selectivity of stearic acid hydrodeoxygenation reaction.

Publications

L. Souza Macedo, D. R. Stellwagen, V. Teixeira da Silva, J. H. Bitter, Stability of Transition-metal Carbides in Liquid Phase Reactions Relevant for Biomass-Based Conversion, ***ChemCatChem***, 7, **2015**, 2816 – 2823.

L. Souza Macedo, R. R. Oliveira Jr., T. van Haasterecht, V. Teixeira da Silva, H. Bitter, Influence of synthesis method on molybdenum carbide crystal structure and catalytic performance in stearic acid hydrodeoxygenation, ***Applied Catalysis B: Environmental***, 241, **2019**, 81 – 88.

Overview of completed training activities

Discipline specific courses and activities

Special problems in catalysis	Federal University of Rio de Janeiro (UFRJ)	Brazil	2012
Chemical characterization of catalysts	Federal University of Rio de Janeiro (UFRJ)	Brazil	2012
Special topics in catalysis	Federal University of Rio de Janeiro (UFRJ)	Brazil	2013
Process optimization	Federal University of Rio de Janeiro (UFRJ)	Brazil	2013
Netherlands' catalysis and chemistry conference 2014	VIRAN, KNCV, FWO, NIOK, DCS, NOW-CW	Netherlands	2014
Catalysis: An integrated approach	Nederlands Instituut voor Onderzoek in de Katalyse (NIOK)	Netherlands	2014
Netherlands' catalysis and chemistry conference 2016	VIRAN, KNCV, FWO, NIOK, DCS, NOW-CW	Netherlands	2016
Advanced chemistry	VLAG	Netherlands	2016

General courses

VLAG PhD week	VLAG	Netherlands	2014
PhD workshop carousel 2014	WGS	Netherlands	2014
Reviewing a scientific paper	WGS	Netherlands	2014
Entrepreneurship in and outside science	WGS	Netherlands	2014
Scientific writing	WGS	Netherlands	2016
Career assessment		Netherlands	2016/ 2017
PhD workshop carousel 2017	WGS	Netherlands	2017

Others

Preparation of research proposal	Research group – Biobased chemistry and technology (BCT)	Netherlands	2014
Biorefinery products: Renewable Resources for the Bulk Chemical Industry (BCH-50306)	BCT	Netherlands	2016
Weekly group meetings	Research group – Biobased chemistry and technology (BCT)	Netherlands	n.a.

The research described in this thesis was financially supported by the 'Conselho Nacional de Desenvolvimento Científico e Tecnológico' (CNPq, Brazil) and by Wageningen University.

Cover design by Lucio Maia de Oliveira
Cover description: Vegetable/waste oil passes through the heterogeneous (solid) catalyst and is converted into several chemical molecules.
Thesis layout by Luana Souza Macedo
Printed by Proefschriftmaken.nl